U.S. Department
of Transportation
Federal Railroad
Administration

Office of Research,
Development and Technology
Washington, DC 20590

Defect Growth Characterization in Modern Rail Steel

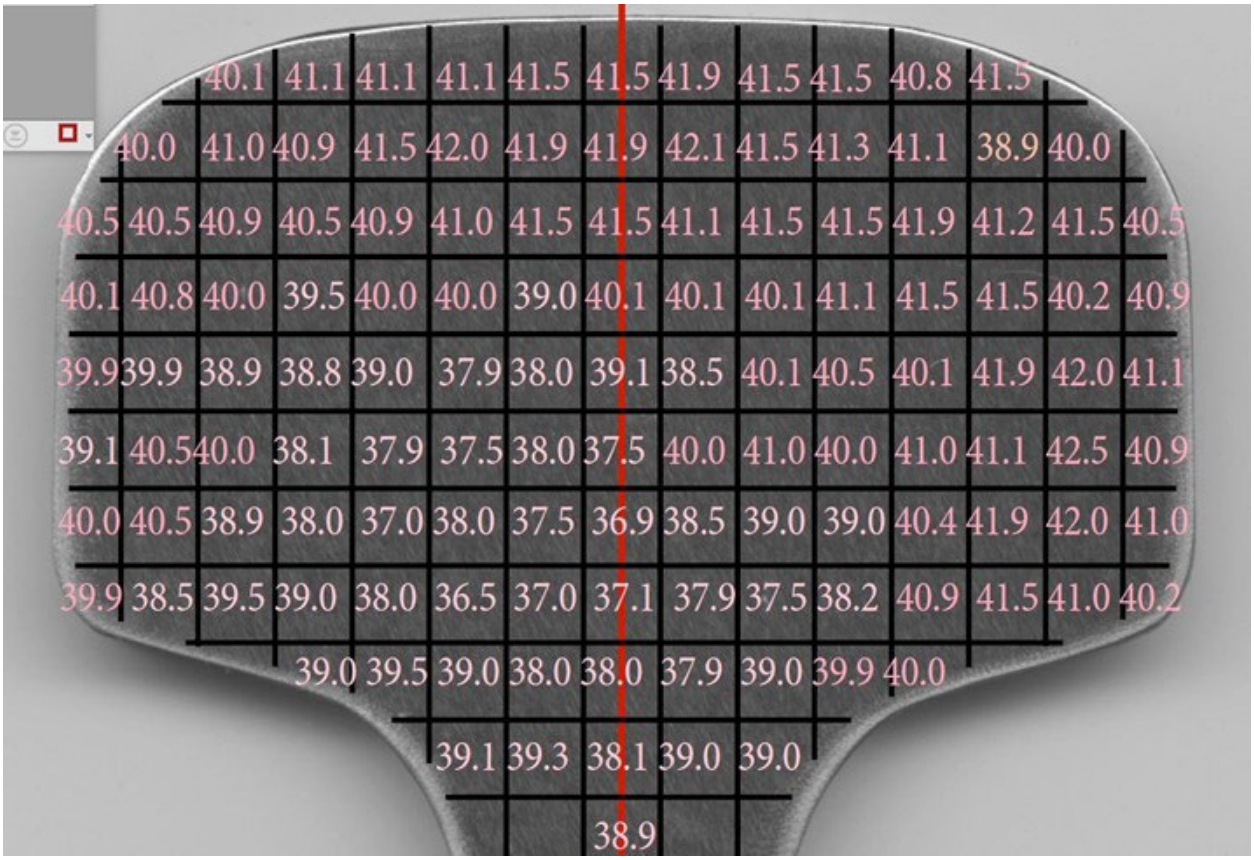

REPORT DOCUMENTATION PAGE

Form Approved
OMB No. 0704-0188

1. REPORT DATE *(DD-MM-YYYY)*	**2. REPORT TYPE**	**3. DATES COVERED** *(From - To)*
25-07-2024	Technical Report	01/05/2016 to 03/20/2018

4. TITLE AND SUBTITLE

Defect Growth Characterization in Modern Rail Steel

5a. CONTRACT NUMBER
DTFR5316C00001

5b. GRANT NUMBER

5c. PROGRAM ELEMENT NUMBER

6. AUTHOR(S)

Pawel B. Woelke: ORCID #0000-0003-0114-9635
Herman F. Nied: ORCID #0000-0002-7668-0431
John N. DuPont: ORCID #0009-0008-2392-750X
Sena Kizildemir: ORCID #0000-0001-6636-7057
Fred B. Fletcher: ORCID #0000-0002-1203-1264
John W. Hutchinson: ORCID #0000-0001-6435-3612

5d. PROJECT NUMBER

5e. TASK NUMBER

5f. WORK UNIT NUMBER

7. PERFORMING ORGANIZATION NAME(S) AND ADDRESS(ES)
Thornton Tomasetti—Weidlinger Applied Science
40 Wall St., 19th floor
New York, NY 10005-1304

8. PERFORMING ORGANIZATION REPORT NUMBER

TT-WAS/FRA/2018-1

9. SPONSORING/MONITORING AGENCY NAME(S) AND ADDRESS(ES)
U.S. Department of Transportation
Federal Railroad Administration
Office of Railroad Policy and Development
Office of Research, Development, and Technology
Washington, DC 20590

10. SPONSOR/MONITOR'S ACRONYM(S)

11. SPONSOR/MONITOR'S REPORT NUMBER(S)
DOT/FRA/ORD-24/23

12. DISTRIBUTION/AVAILABILITY STATEMENT
This document is available to the public through the FRA website.

13. SUPPLEMENTARY NOTES
COR: Robert Wilson

14. ABSTRACT
This report discusses a comprehensive fatigue and fracture characterization of modern head-hardened rails in reference to legacy rails. The focus is in on detail (i.e., transverse) fracture, the effects of the microstructural gradient in the railhead, and residual stresses caused by head-hardening and roller straightening. A key objective of this study is to develop the information necessary to determine if an existing rail inspection interval, established for legacy rails is valid for modern, head-hardened rails.
Five rails (two head-hardened and one modern control rail and two legacy rails) were investigated. As expected, the head-hardened rails show significantly improved hardness and strength in the railhead, comparing to the legacy rails, which contributes to improved wear resistance. While in many cases, increasing material hardness and strength results in reduction of toughness and fatigue life, results of the current study indicate that this is not the case. Both toughness and fatigue crack growth rates are similar across all investigated rails, which indicates that the rail inspection interval, previously established for legacy rails may not require revisions for modern rails.

15. SUBJECT TERMS
Modern rail steel characterization, railhead hardening, detail fracture, fatigue, microstructural gradient in railhead, residual stresses, rail inspection interval

16. SECURITY CLASSIFICATION OF:			**17. LIMITATION OF ABSTRACT**	**18. NUMBER OF PAGES**	**19a. NAME OF RESPONSIBLE PERSON**
a. REPORT Unclassified	**b. ABSTRACT** Unclassified	**c. THIS PAGE** Unclassified		112	**19b. TELEPHONE NUMBER** *(Include area code)*

Standard Form 298 (Rev. 8/98)
Prescribed by ANSI Std. Z39.18

METRIC/ENGLISH CONVERSION FACTORS

ENGLISH TO METRIC	METRIC TO ENGLISH
LENGTH (APPROXIMATE)	**LENGTH (APPROXIMATE)**
1 inch (in) = 2.5 centimeters (cm)	1 millimeter (mm) = 0.04 inch (in)
1 foot (ft) = 30 centimeters (cm)	1 centimeter (cm) = 0.4 inch (in)
1 yard (yd) = 0.9 meter (m)	1 meter (m) = 3.3 feet (ft)
1 mile (mi) = 1.6 kilometers (km)	1 meter (m) = 1.1 yards (yd)
	1 kilometer (km) = 0.6 mile (mi)
AREA (APPROXIMATE)	**AREA (APPROXIMATE)**
1 square inch (sq in, in^2) = 6.5 square centimeters (cm^2)	1 square centimeter (cm^2) = 0.16 square inch (sq in, in^2)
1 square foot (sq ft, ft^2) = 0.09 square meter (m^2)	1 square meter (m^2) = 1.2 square yards (sq yd, yd^2)
1 square yard (sq yd, yd^2) = 0.8 square meter (m^2)	1 square kilometer (km^2) = 0.4 square mile (sq mi, mi^2)
1 square mile (sq mi, mi^2) = 2.6 square kilometers (km^2)	10,000 square meters (m^2) = 1 hectare (ha) = 2.5 acres
1 acre = 0.4 hectare (he) = 4,000 square meters (m^2)	
MASS - WEIGHT (APPROXIMATE)	**MASS - WEIGHT (APPROXIMATE)**
1 ounce (oz) = 28 grams (gm)	1 gram (gm) = 0.036 ounce (oz)
1 pound (lb) = 0.45 kilogram (kg)	1 kilogram (kg) = 2.2 pounds (lb)
1 short ton = 2,000 pounds (lb) = 0.9 tonne (t)	1 tonne (t) = 1,000 kilograms (kg) = 1.1 short tons
VOLUME (APPROXIMATE)	**VOLUME (APPROXIMATE)**
1 teaspoon (tsp) = 5 milliliters (ml)	1 milliliter (ml) = 0.03 fluid ounce (fl oz)
1 tablespoon (tbsp) = 15 milliliters (ml)	1 liter (l) = 2.1 pints (pt)
1 fluid ounce (fl oz) = 30 milliliters (ml)	1 liter (l) = 1.06 quarts (qt)
1 cup (c) = 0.24 liter (l)	1 liter (l) = 0.26 gallon (gal)
1 pint (pt) = 0.47 liter (l)	
1 quart (qt) = 0.96 liter (l)	
1 gallon (gal) = 3.8 liters (l)	
1 cubic foot (cu ft, ft^3) = 0.03 cubic meter (m^3)	1 cubic meter (m^3) = 36 cubic feet (cu ft, ft^3)
1 cubic yard (cu yd, yd^3) = 0.76 cubic meter (m^3)	1 cubic meter (m^3) = 1.3 cubic yards (cu yd, yd^3)
TEMPERATURE (EXACT)	**TEMPERATURE (EXACT)**
[(x-32)(5/9)] °F = y °C	[(9/5) y + 32] °C = x °F

QUICK INCH - CENTIMETER LENGTH CONVERSION

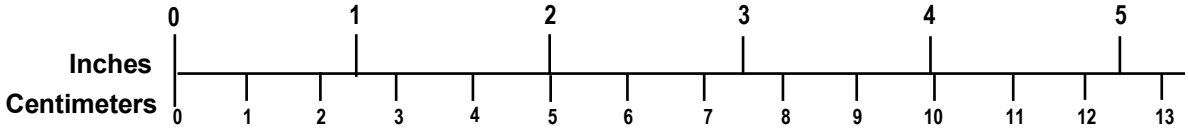

QUICK FAHRENHEIT - CELSIUS TEMPERATURE CONVERSIO

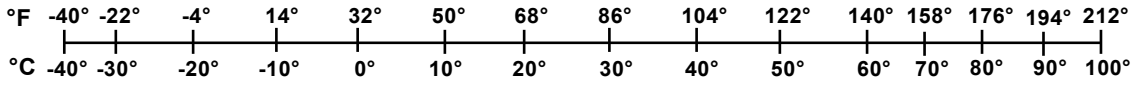

For more exact and or other conversion factors, see NIST Miscellaneous Publication 286, Units of Weights and Measures. Price $2.50 SD Catalog No. C13 10286

Updated 6/17/98

Acknowledgments

We gratefully acknowledge the Federal Railroad Administration, specifically Dr. Robert Wilson for his management and technical contributions.

We also acknowledge invaluable technical contributions by Dr. David Jeong, as well as those of Michael Carolan and Dr. Benjamin Perlman of the Volpe National Transportation Systems Center.

We gratefully acknowledge the contributions of Dr. Fred Fletcher of ArcelorMittal, who donated three new rails and offered great technical insights into all aspects of the project.

At Lehigh University, Dick Towne, Eli Towne, Bill Maroun, and Mike Rex expertly handled the extensive machining required to fabricate the test fixtures and specimens needed for this study. We also acknowledge the contributions of three Lehigh undergraduate students: Erwin Fuentes, Lezheng Fang, and Jiaye Chen, who provided critical assistance in machining and polishing specimens and performing experimental measurements.

We also thank Dr. Matthew A. Adler of Laboratory Testing, Inc., who provided valuable assistance conducting fracture tests on Center Cracked Tension specimens. His comments and recommendations on fatigue testing procedures are appreciated.

Finally, Dr. Thomas Gnaupel-Herold of the National Institute of Standards and Technology (NIST) and Dr. Majid Farajian of Fraunhofer Institut für Werkstoffmechanik performed the neutron diffraction measurements for the measurement of residual stresses in the investigated rails, which was an essential element of the project. We gratefully acknowledge their contributions.

Contents

Illustrations

Tables

Executive Summary

In this project, the research team designed and executed a comprehensive experimental and numerical program for fatigue characterization of modern head-hardened rails, with a specific focus on detail (i.e., transverse) fracture. This program provides necessary information to determine a safe and economically viable rail inspection interval, which will be pursued in follow-up projects.

A safe inspection interval has previously been established for legacy (i.e., non-head-hardened) rails. The head hardening process, which evolved over the past several decades, has been designed to improve rail wear resistance by increasing hardness. However, increasing hardness, which is related to strength, typically results in reduction of toughness and fatigue life. This means that while improved wear resistance can extend the wear life of the rail, its fatigue life can simultaneously be reduced. Consequently, the safe inspection interval for legacy rails is not necessarily valid for modern rails. Thorough material characterization of modern rails in reference to legacy rails is necessary to establish the applicability of the legacy rail inspection interval to head-hardened rails.

Three modern rails (ArcelorMittal's advanced head-hardened [AHH], head-hardened [HH], and standard, control-cooled [SS] rail) and two unused legacy rails, produced in 1977 and 1984, were investigated here. The SS rail, the legacy rails, and existing data were used as references. As expected, the two modern head-hardened rails (AHH and HH) are significantly harder and stronger than the control rail (SS) and the two legacy rails. Uniform pearlitic microstructure was observed in all rails, with hardness and strength variation caused primarily by pearlite spacing, which is controlled by the cooling rate and the alloy content. Despite the strength variation, toughness test results are mostly uniform across all rails, with some spatial variation inside the railheads. Similarly, no significant differences in fatigue crack growth rates between modern and legacy rails have been observed (especially between AHH and legacy rails). These results indicate that the head-hardening process designed to improve wear resistance does not have a significant negative impact on the fatigue life of rails. It is important to note that improving wear resistance of modern rails without sacrificing fatigue properties in reference to legacy rails is a significant enhancement in rail manufacturing technology. However, it can result in fatigue becoming the limiting factor for the overall life of the rail, which places higher emphasis on rail inspection and characterization of fatigue and fracture properties.

Residual stresses due to heat treatment and roller straightening were also investigated in the AHH and HH rails by means of neutron diffraction measurements supplemented by advanced numerical analysis. The results show that the largest stress component (~350MPa) is the longitudinal stress, which is also the most consequential for fatigue growth of transverse defects. Given the long beam time required to penetrate the rail material, full 3D distribution of residual stresses is difficult to obtain. Additionally, interpretation of the residual stress state measured with smaller specimens, such as plane stress slices and half-rail samples cut along the longitudinal, vertical symmetry plane, is very challenging due to significant level of interaction between different stress components. This means that extracting a rail specimen by cutting not only relives the stress component normal to the cut plane, but it also affects the remaining stress components. Some of these challenges can be, to a certain degree, alleviated by numerical analysis, which will be pursued in the next phase of the project. Considering the importance of

the longitudinal residual stresses for transverse crack growth rates, their magnitude and distribution, as well as the effect of rail-wheel contact, require further investigation.

Since only a representative subset of existing rails was investigated here, a testing protocol that can be applied to other rails was also developed. This testing protocol includes only the most relevant experimental tests, which were determined based on the results of a comprehensive program discussed in this report. Establishing the reduced testing protocol requires that the most important effects are understood first, which is one of the main accomplishments of this project.

1. Introduction

1.1 Background

One of the most important threats to the safe operation of rail transport is related to the propagation of internal transverse rail defects known as detail fractures (Figure 1b). A detail fracture typically originates from the longitudinal fracture crack known as the shell (Figure 1a). Detail fractures can grow to critical size without any visible material damage on the rail surface [14]. This topic has been extensively investigated during the past several decades by the Volpe National Transportation Systems Center (Volpe) in conjunction with the rail industry, which resulted in a comprehensive life evaluation methodology for legacy rails (i.e., non-head-hardened rails [5, 6, 8, 9, 10, 12]) and establishing the maximum inspection interval of 40 MGT [10].

The railhead hardening process, which has been evolving over the past 30 years, is a major improvement in the rail manufacturing technology. The main objective of head hardening is to improve wear resistance of rails achieved by increasing hardness (and therefore strength) of the head. In most steels, strength increase is usually associated with ductility reduction, which negatively affects fracture toughness. In addition, the process of head hardening involves quenching of the top of the railhead by spraying water, mist, or oil, which introduces a microstructural gradient inside the head (Figure 1c). This can lead to variable crack growth rate inside the head. Another important effect to consider is the influence of residual stresses introduced by the heat treatment process. Residual stresses provide a significant contribution to the overall stress state in the railhead. In addition, their distribution follows, to some degree, the microstructural gradient, i.e., residual compression on the top of the railhead changes to tension inside the head, where the material is softer. Interaction of these two effects, (property variation and residual stress distribution) in the railhead can have a significant effect on the fatigue life of the rail. Thus, the inspection intervals previously determined for legacy rails, might not be applicable to modern head-hardened rails.

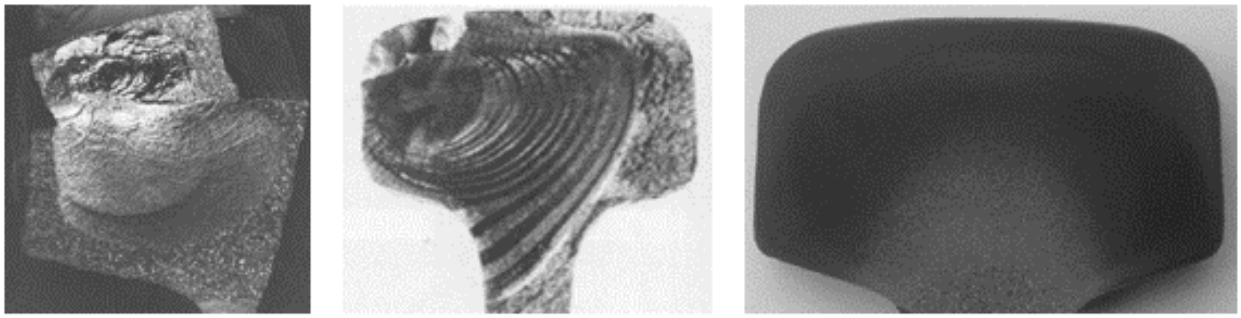

(a) (b) (c)

Figure 1. (a) Longitudinal shell fracture and transition into the detail fracture; (b) Detail fracture [13]; (c) Microstructural gradient produced by the heat treatment in modern rails [16]

Establishing the new inspection interval for modern rails would require a multiyear effort, like the one conducted previously for legacy rails, which spanned several decades. This is beyond the scope of the project discussed in this report. The focus of the effort discussed here is on detailed experimental investigation of the effects of head hardening on fatigue and fracture properties in modern rails, in reference to legacy rails.

1.2 Objectives

The main objective of this research effort is to investigate the effects of head hardening on fatigue behavior of modern rails. The data and observations made during the project and presented in this report provide necessary information to determine a safe and economically viable inspection interval for modern rails.

A secondary objective of the project is development of a systematic and repeatable testing protocol to characterize the microstructural gradient and residual stresses in rails, as well as a clear and consistent procedure to collect and interpret the data. This protocol is necessary considering significant variability in the rail properties resulting from different railhead hardening process used over the past 30 years (e.g., induction cooling, compressed air, water or mist cooling, oil quenching [1, 16]).

1.3 Overall Approach

Reaching the project objectives requires detailed experimental characterization of modern rail steel. Multiple experimental techniques and methods were employed to investigate specific aspects of fatigue behavior in rails, including:

- **Hardness**: Rockwell hardness mapping is used to identify strategic locations for collection of material samples for light optical microscopy (LOM) and scanning electron microscopy (SEM). Hardness maps provide a general overview of spatial property distribution in the railhead, which is a function of microstructural gradient.
- **Metallography**: LOM and SEM microstructural observations using Hitachi 4300 High Resolution Field Emission SEM equipped with a state-of-the-art integrated EDAX-TSL energy dispersive X-ray system. These observations allow a detailed mapping of the microstructure in the railheads.
- **Tensile Testing**: Tensile testing of the rail steel using samples extracted from different location inside the rail. Tensile tests provide a simple and effective way of investigating the elastic properties and the yield strength of the investigated rails as well as their ductility under uniaxial loading conditions.
- **Toughness and Fatigue Testing**: Fracture toughness and fatigue crack growth measurements using machined compact tension (CT) and center cracked tension (CCT) specimens cut from various locations and orientations within the rails. These measurements are an essential component of investigating fatigue properties of rail steels. All previously conducted tests (hardness, metallography, tensile tests) provide necessary information for strategic planning of fracture and fatigue tests.
- **Residual Stress Measurements**: Neutron diffraction measurements performed to characterize the residual stress field in the rail. Detailed finite element simulations are used to optimize the specimens and analyze the data. These measurements allow approximation of the residual stress field in the railheads, which is a significant component of the overall stress state in the rails.

These and other measurement methods are used to characterize a representation of three modern rails, i.e., advanced head hardened (AHH), head hardened (HH) and standard control-cooled rail (SS), all of which were donated by ArcelorMittal. The SS rail serves as a baseline providing the

reference data for comparison with the head-hardened rail data. In addition, two unused legacy rails are characterized: a Colorado Fuel & Iron (CF&I) control-cooled rail manufactured in 1977 (CF&I77) and a vacuum heat-treated Hayange Steel rail produced in 1984 (HAY84). While this representation of different rails and their properties can be considered comprehensive, it does not cover all possible rail types. Thus, the data generated here for both modern and legacy rails are used for direct comparison with the corresponding data generated during the legacy Rail Integrity Research Program [5, 8, 10, 12]. This allows quantification of the microstructural gradient and residual stress effects on fatigue crack growth rate in modern rails in reference to legacy rails, expressed by the parameters of the crack growth relationship. Since a Paris-Walker relationship was used during the legacy Rail Integrity Program and its parameters for legacy rails were determined [7], the same relationship is used here for modern rails.

All critical observations and conclusions reached during execution of the experimental program were collected and documented. This serves the second objective of the project, development of a testing protocol for characterizing fatigue properties of modern rails.

1.4 Scope

Experimental material characterization effort is the primary component of the scope of work discussed in this report. The test plan is designed to meet the project objectives: investigation of the microstructural gradient and residual stress effects on fatigue and fracture properties of modern, head-hardened rail steel, in reference to legacy rail steel.

Five distinct rail types are used in the experimental program and are given the following designations throughout this report:

1. AHH: advanced head-hardened; new rail manufactured by ArcelorMittal
2. HH: head-hardened; new rail manufactured by ArcelorMittal
3. SS: standard, control-cooled rail; new non-head-hardened rail manufactured by ArcelorMittal
4. CF&I77: Colorado Fuel & Iron control-cooled rail manufactured in 1977; never used
5. HAY84 – Hayange Steel vacuum heat treated rail manufactured in 1984; never used

The project includes the following tasks:

- **Task 1 — Microstructural gradient**: The objective of this task is to characterize the microstructural gradient in modern rails in reference to legacy rails through a combination of mechanical tests and metallurgical observations performed using LOM and SEM.
- **Task 2 — Residual stress**: The objective of this task is to characterize the residual stress state in the rails through a combination of neutron diffraction measurements and detailed finite element analyses.
- **Task 3 — Bending stress gradient**: The objective of this task is to characterize the effect of different stress states in the rails caused by a combination of bending and residual stresses through toughness and fatigue crack growth rate measurements.
- **Task 4 — Data analysis and testing protocol**: This task is intended to collect and summarize the key observations made during the experimental testing program to

establish best testing practices and a systematic test program that could be used broadly to characterize rail steel.

A detailed breakdown of project tasks, subtasks, milestones, and deliverables is given in Table 1.

Table 1. Project task breakdown and an experimental test plan

Tasks, Subtasks/Tests	Type of Test	Test Plan (Modern and Legacy Rails)
1. MICROSTRUCTURAL GRADIENT		
Chemical analysis of legacy rail steel	Chemical analysis	2 AM steels and '77 and '80s rails[1]
Tensile test data	Uniaxial tension	5 samples: 3 AM steels[2] plus '77 and '80s rails
Hardness data from AM – initial screening	Existing data	3 AM steels[2]
Rockwell Hardness mapping (all rails)		3 AM steels plus '77 and '80s rails
LOM – interpretation of the hardness map		3 AM steels plus '77 and '80s rails
Hitachi 4300 High Resolution Field Emission SEM – samples removed based on LOM results		2 AM steels (AHH, HH) plus '77 and '80s rails
CT specimens – K_{Ic} plane strain toughness;	K_{Ic} ASTM E1820	5 CT locations[3]: 2 AM steels (AHH, HH) plus '77 and '80s rails
Compact tension specimens – fatigue tests (da/dN tests); additional verification tests with center cracked tension specimen (CCT)	ASTM E647	5 CT locations, constant ΔK: 2 AM steels (AHH, HH) plus '77 and '80s rails. 2 CCT verification tests, 2AM steels
Rail samples – fatigue tests with constant ΔK tests → correlate with the CT results	Constant ΔK	2 AM steels (AHH, HH) plus '77 and '80s rails
2. RESIDUAL STRESSES		
Residual stress measurements – transverse and vertical stresses using thin slices	Neutron diffraction	3AM steels plus '77 and '80s rails, 4 samples per rail
Residual stress measurements longitudinal direction (x "axial" stress component)	Neutron diffraction /contour	Single rail – AHH (highest strength)
3. STRESS GRADIENT		
Fatigue tests with under different stress states reflecting variable stress ratio	Variable stress ratio	3 CT – 2 steels (6 tests)

1. Chemical analysis was performed by ArcelorMittal.
2. ArcelorMittal steels are three rails donated by ArcelorMittal and designated as AHH, HH, SS.
3. CT specimen locations are discussed in a latter section of the report.

The project team was led by Thornton Tomasetti of Weidlinger Applied Science and Dr. Pawel Woelke, who served as a Principal Investigator. Most of the experimental tests were conducted by a team from Lehigh University: Dr. Herman Nied (Mechanical Engineering), Sena Kizildemir (Civil Engineering graduate student), and Dr. John N. DuPont (Materials Science). Neutron diffraction measurements of residual stresses were conducted by Dr. Thomas Gnaupel-Herold at the National Institute of Standards and Technology (NIST) and Dr. Majid Farajian of Fraunhofer Institut für Werkstoffmechanik (IWM). Dr. John Hutchinson of Harvard University served as a consultant and an advisor to the project. Dr. Fred Fletcher of ArcelorMittal supported the project by donating rails to the program and by providing critical input related to the rail microstructure, material properties, and other related information.

1.5 Organization of the Report

The next section of the report (Section 2) discusses the experimental test program, including all pertinent tests performed in support of the project and a summary of the results. Also included in Section 2 are the measurement of the residual stresses in the rails and the supporting finite element simulations performed to optimize the test specimens and interpret the results. Section 3 presents the data analysis and the testing protocol to characterize the microstructural gradient and residual stresses in rails. Section 4 consists of the conclusions and discussion. The raw data spreadsheets are included in the Appendices:

- Appendix A. Hardness Values as a Function of Position
- Appendix B. Tensile Stress Strain Curves
- Appendix C. Load vs COD for Fracture Toughness

2. Mechanical Testing of Rails

To characterize and quantify the mechanical behavior of head-hardened rails of different types, grades, and their properties, the research team established a repeatable testing protocol. The purpose of this testing was to contrast different types of modern head-hardened rails (AHH, HH) with standard modern rail (SS) and legacy rails that exhibit significantly lower head hardness (CF&I77, HAY84). The testing protocol required a sequence of chemical, mechanical, and metallurgical tests. These tests may be listed under six main categories:

1. Characterization of alloy chemistry
2. Characterization of metallurgical microstructure
3. Characterization of uniaxial tensile properties
4. Characterization of fracture toughness
5. Characterization of fatigue crack growth behavior
6. Characterization of residual stress distribution

The mechanical testing and metallurgical observations were conducted primarily using facilities at Lehigh University. ArcelorMittal Global R & D performed the chemical analyses, and NIST performed the residual stress measurements at their neutron diffraction facilities.

2.1 Test Articles

The main objective of this project is the characterization of the effects associated with railhead hardening, including the resulting residual stresses on fatigue and fracture behavior of rails. This is achieved by establishing a reference set of properties obtained for non-head-hardened, i.e., SS and legacy rails, and comparing the properties of head-hardened rails to the reference rails. Most of the reference properties were established during the legacy rail integrity research program conducted during the 1980's and 1990's [5, 6, 8, 9, 10, 12]. In addition, two legacy rails (CF&I77 and HAY84) and one new control-cooled rail (SS) are included in the current research program to provide further reference data for comparison with modern head-hardened rail data. Thus, five distinct rails, shown in Table 2, were used as test articles in this study.

Table 2. Rails used as test articles with their designations

Rail Type	Designation	Manufacturer	Weight	Heat Treatment	Wear	Notes
Modern	**AHH**	ArcelorMittal	136 RE	Head hardened; fast cooled	New	Donated by AM
Modern	**HH**	ArcelorMittal	136 RE	Head hardened	New	Donated by AM
Modern	**SS**	ArcelorMittal	136 RE	Control-cooled	New	Donated by AM
Legacy	**CF&I77**	Colorado Fuel & Iron, 1977	136 RE	Control-cooled	Never used	Donated by TTCI
Legacy	**HAY84**	Hayange Steel (now Tata Steel)	136 RE	Vacuum heat treated and degassed	Never used	Donated by TTCI

The AHH, HH, and SS rails were originally shipped in 30 ft lengths to Lehigh University and then cut into smaller, 3 ft sections for subsequent sawing into plate stock and machining into test specimens. In the cutting and testing procedures, specimens were usually cut from horizontal slices in the railhead, or from vertical plates as shown in Figure 2. For example, Figure 2a depicts the orientation of 0.025 in thick horizontal plates cut for uniaxial tensile test specimens and Figure 2b shows the plate thickness dimensions for two plates cut for fracture toughness (CT) specimens in the vertical direction. In both drawings, the long dimension of the plates, usually 1–3 ft, coincides with the long axis of the rail.

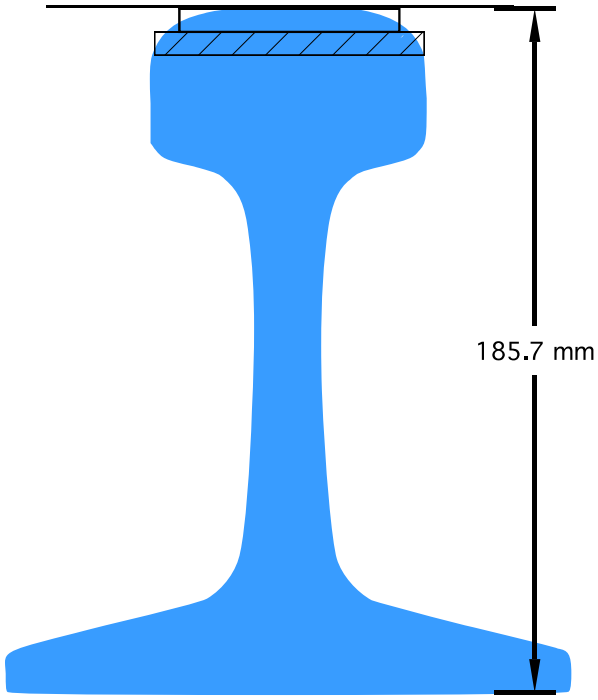

(a) (b)

Figure 2. (a) Locations of horizontal plates cut for uniaxial test specimens, (b) Location of vertical plate cuts for CT specimens with vertical crack orientations

2.2 Chemical Composition

The chemical compositions of the modern rails employed in this study are shown in Table 3. The SS and HH rails comply with the requirements listed in AREMA for Carbon Rail Steel. Note that the HH rail is like the SS rail, with a small addition of titanium in the HH rail. The AHH rail has less manganese than the other two new rails, plus a small addition of vanadium. While AHH is not currently listed within the AREMA rail specification, AREMA permits the chemical composition limits of alloy high-strength rail steel grades to be subject to agreement between the purchaser and the manufacturer. Such agreements have enabled AHH rails to be placed in revenue service.

Table 3. Chemical composition of ArcelorMittal rails AHH, HH, and SS

Type	C	Mn	P	S	Si	Cu	Ni	Cr	Mo	V	Nb	Ti	Al	B	N
AHH	0.84	0.69	0.012	0.012	0.54	0.26	0.09	0.24	0.023	0.086	0.002	0.022	0.004	0.0001	0.0087
HH	0.85	0.98	0.011	0.012	0.4	0.22	0.1	0.25	0.033	0.004	0.003	0.018	0.004	0.0003	0.0102
SS	0.83	1.11	0.011	0.012	0.54	0.25	0.11	0.21	0.023	0.004	0.003	0.003	0.004	0.0003	0.0087

Table 4 shows the compositions of the legacy rails. While the carbon content of the legacy rails is significantly less than the modern rails, the HAY84 rail meets the current AREMA chemical analysis for carbon rail steel. The CR&I77 rail contains only 0.72 percent C, which is less than the 0.74 percent C minimum currently required by AREMA for carbon rail steel. The HAY84 rail contains much less copper than the other four rails and the CF&I77 rail has a significantly higher silicon content.

Table 4. Chemical composition of legacy rails designated HAY and CF&I

Type	C	Mn	P	S	Si	Cu	Ni	Cr	Mo	V
HAY84	0.79	1.13	0.016	0.019	0.407	0.02	0.05	0.16	0.006	0.003
CF&I77	0.72	0.92	0.012	0.017	0.762	0.23	0.08	0.07	0.013	0.002

Table 5. Chemical composition of legacy rails continued

Type	Nb	Ti	Al	B	N	Sn	Sb	Co	Ca	Pb
HAY84	0.001	0.001	0.009	0.0002	0.0073	0.002	0.0009	0.015	0.0004	0.0029
CF&I77	0.002	0.003	0.009	0.0002	0.0073	0.013	0.003	0.0118	0.0007	0.0045

The five rails included in this study represent many miles of rail in revenue service in the U.S.

2.3 Hardness Testing

The purpose of the hardness testing was to determine the difference in hardness among the five rails examined in this study. Since the team expected that the rails would not only exhibit different maximum hardness, but different spatial variations in hardness, they generated a hardness map for each railhead using 5 mm x 5 mm grid cells. The hardness measurements were performed using a standard Rockwell hardness tester on 8 mm thick plate cross sections from each of the rails. For the hardness tests, a C Brale penetrator was used with a 150 kg load.

2.3.1 Sample Preparation

The preparation of test samples for hardness measurements involved saw-cutting 8 mm thick representative cross-sections from each of the 136RE rails. After cutting, the rail cross-sections were surface ground and marked with a 5 mm x 5 mm grid overlay using a low-power laser. Hardness measurements were made at the center point of each of the 5 mm x 5 mm cells over the entire head region of the rail, including along a vertical line at the center of the web, and along a line close to the bottom of the rail.

2.3.2 Hardness Measurements

The hardness measurements were performed on the head portions of the rail cross-sections, along a vertical line in the web, and along a horizontal row on the lower portion of each rail as. Detailed measurements superimposed on the rail cross section are reported in Appendix A, Figures 108–112. Contour plots of the measured hardness values permit a better visualization of the variation in hardness on the face of the railheads. Figure 3 contains contour plots of the HRC hardnesses shown with the same hardness scale. As shown in Figure 3, there are significant differences in the average and maximum head hardness values among the rails. As expected, the progression in rail steel hardness coincides with chronological manufacturing history: the modern rails exhibit the highest head hardness values. In addition, there are significant spatial variations in hardness within any given railhead. Because of the average hardness differences between the rails, the detailed spatial distribution of hardness within a given railhead is best visualized using different hardness scales for each railhead, as shown in Figure 4. As expected, the railhead with the highest hardness in the crown is the AHH rail (Figure 3a and Figure 4a). The AHH rail had a minimum hardness of 36 HRC and a maximum of 43 HRC.

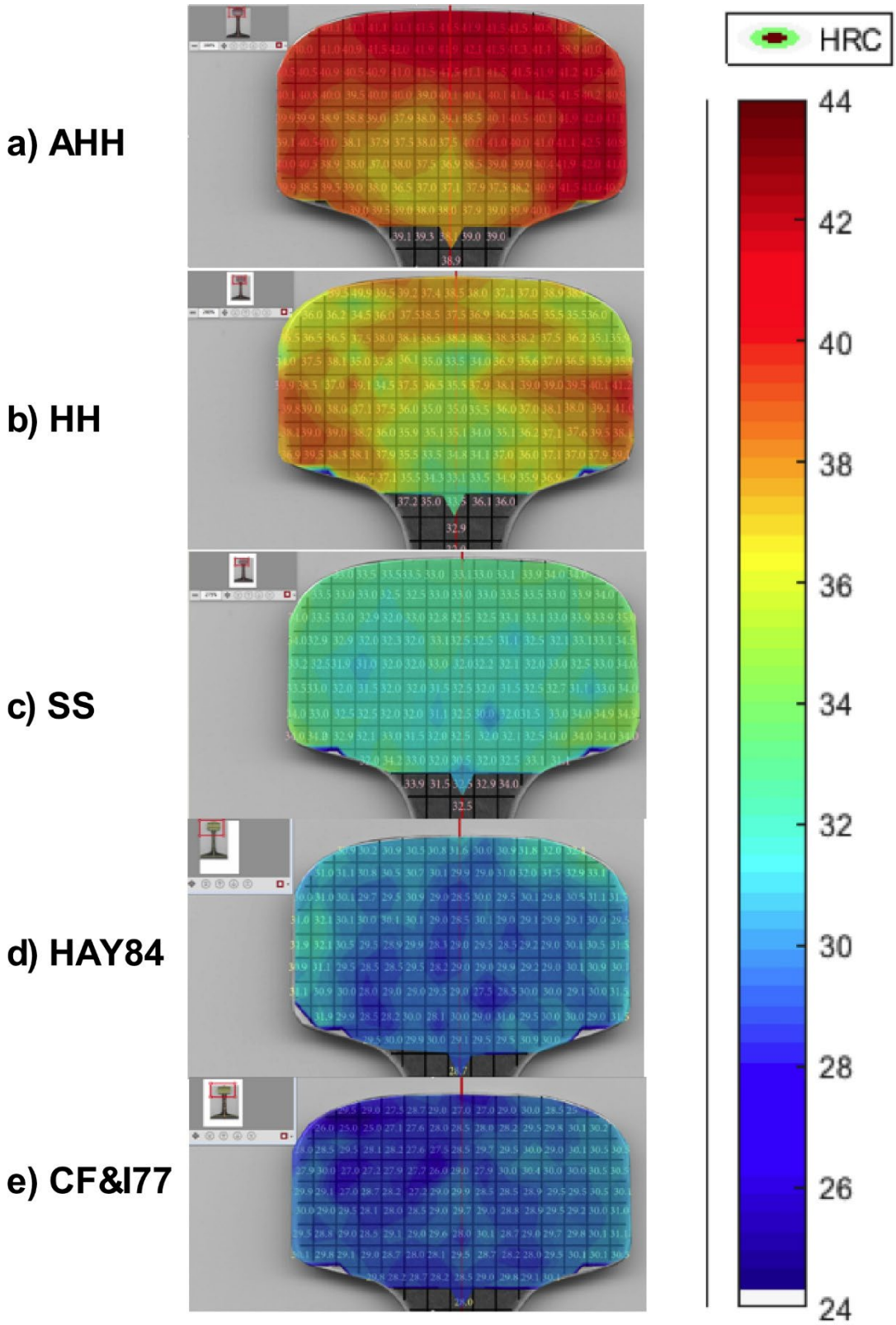

Figure 3. Contour plots showing hardness variation in the railheads using the same HRC scale

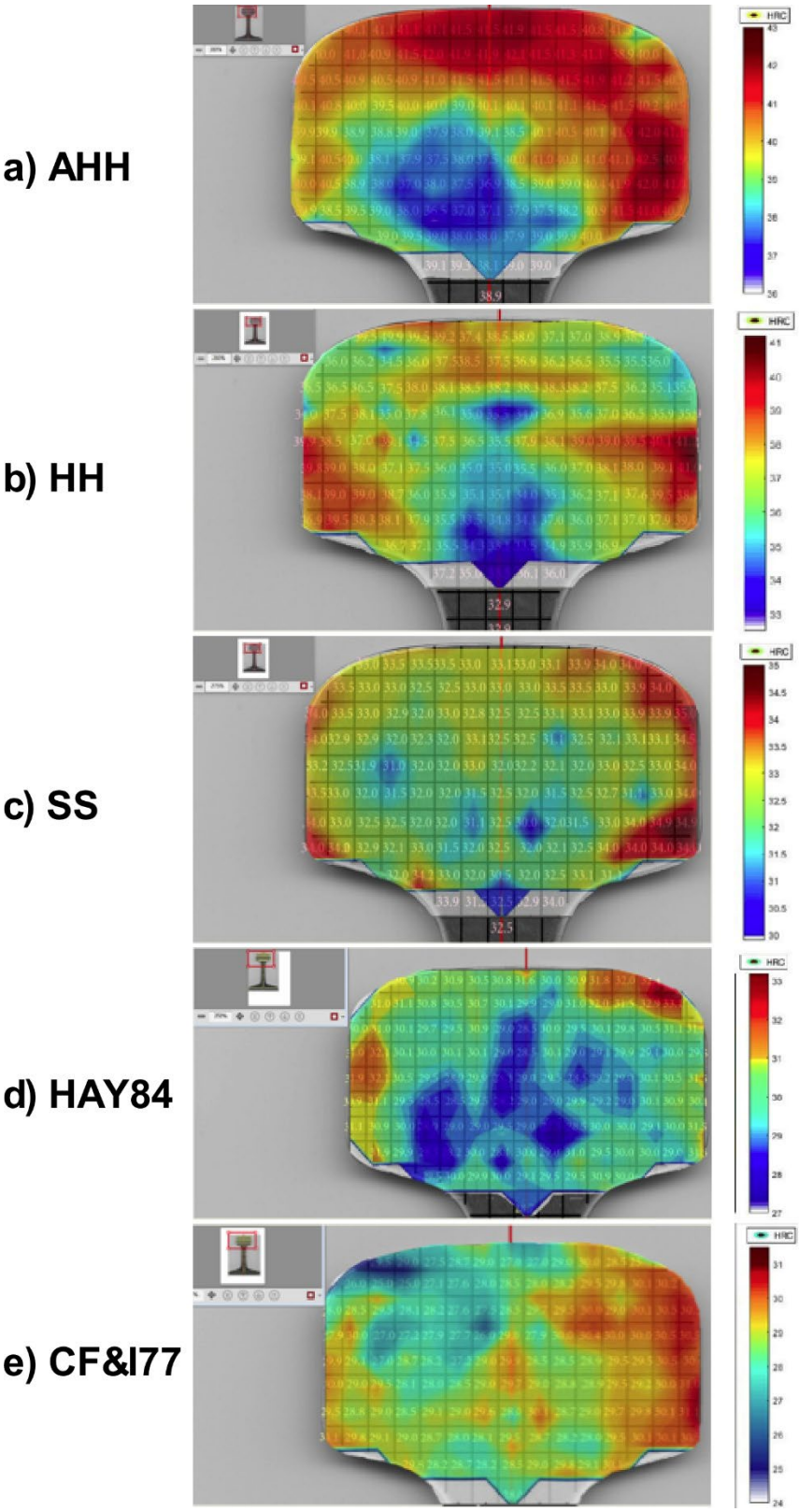

Figure 4. Contour plots showing head hardness variations with different HRC scales. AHH (36–43), HH (33–41), SS (30–35), HAY84 (27–33), CF&I77 (24–31)

It is also useful to plot the hardness variation along the central vertical line measured from the railhead running surface to the base of the head (Figure 5) and horizontally across the midsection of the head (Figure 6). As shown in Figure 5, modern head-hardened rails exhibit considerably higher hardness in the crown of the rail, with hardness values that mostly remains constant within a zone extending at least 12 mm below the railhead running surface.

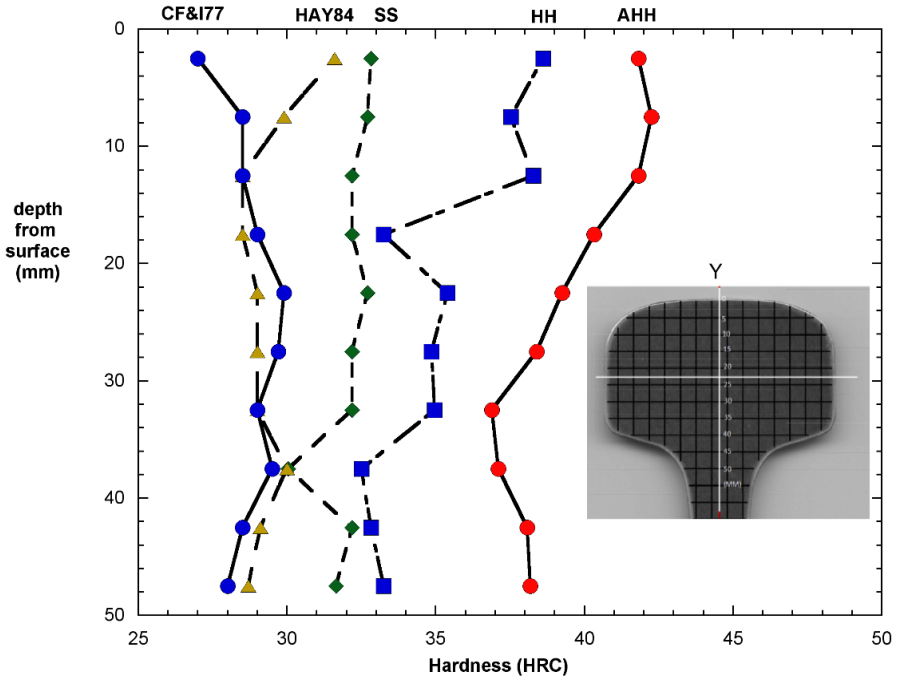

Figure 5. HRC hardness as a function of vertical depth on the plane of symmetry

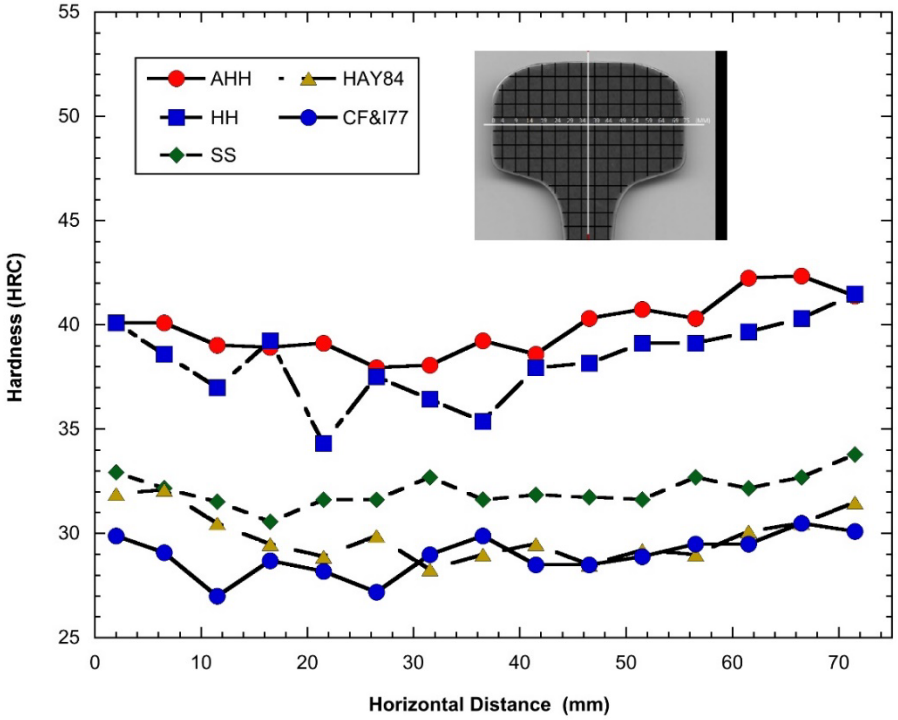

Figure 6. HRC hardness as a function of horizontal position across the head mid-section

2.3.3 Data Interpretation

Figure 3 shows the differences in hardness values for the five rails in this study. Table 6 summarizes the hardness measurements. The average hardness for the outer 20 mm is a good representation of the head material that is subject to abrasive wear in service. The legacy rails are noticeably softer than the modern rails in this important region of the heads. In particular, the AHH rail is significantly harder than even the HH rail. This finding suggests that the wear rates of the modern rails will be much lower than the legacy rails, implying that the fatigue behavior of the modern rails is more important than in the past because the modern rails will sustain longer lives, increasing the probability of fatigue crack development late in service life.

Table 6. Representative Hardness Values of the Rails

	AHH	HH	SS	HAY84	CF&I77
20 mm average	40.7	37.2	33.0	30.4	28.9
Maximum in head	41.9	39.9	34.0	32.4	31.1
Overall head average	40.8	37.1	32.6	30.0	28.8
Web average	35.4	32.2	33.2	29.8	29.3
Base average	36.7	34.2	33.9	31.8	30.2

The other hardness values in Table 6 provide comparisons with the relative hardness of the outer 20 mm of the heads. For example, for all the rails, the average head hardness is only slightly less than the outer 20 mm. Although the two head-hardened rails exhibit some degree of hardness gradient from the surface into the head, the gradient is small, just as it is for the SS and legacy rails that were cooled in air after rolling. The hardness values in the webs of the head-hardened rails, AHH and HH, are approximately 5 HRC softer than the corresponding heads, while the webs of the other rails are essentially the same as their heads. This characteristic is expected. There were no high hardness readings in the webs of any of the rails, demonstrating that the steels were not badly segregated. As expected, the bases of the two head-hardened rails are 3–4 HRC softer than their heads, while the bases of the air-cooled rails are about 1 HRC harder than their heads.

The contour plots shown in Figure 3 suggest that there is reasonable symmetry in the hardness of all five railheads. However, the higher resolution plots given in Figure 4 indicate that there is a degree of asymmetry, especially for the AHH rail. This condition is a consequence of the manufacturing method of rails. A typical hardness variability in the heads is observed for the five rails in this study, which leads to the conclusion that the more advanced properties such as residual stress, fracture toughness, and fatigue crack growth rate reported below can be considered as representative of the rails that are in service.

In addition to the results discussed above, ArcelorMittal performed separate hardness measurements for comparison purposes with the AREMA standards. The running surface of the SS rail was 337 HB, which meets the 310 HB minimum hardness requirements of standard carbon rail. The running surface of the HH rail was 384 HB, which meets the 370 HB minimum hardness requirements for high strength carbon rail. The running surface of the AHH rail was 413 HB (AHH is not included in the current AREMA standards). All three modern rails comply with the hardness requirements of the AREMA rail specification.

2.4 Microstructural Observations with LOM and SEM

2.4.1 Experimental Procedure

Figure 7 shows the locations where five metallographic samples were removed from each rail, and the arrows show the viewing direction associated with each sample. Each sample was mounted in epoxy and polished. The samples were examined in either the as-polished or etched (2 percent nital) condition. Select samples were used for micro-hardness measurements with a Vickers indenter and a 10 g load.

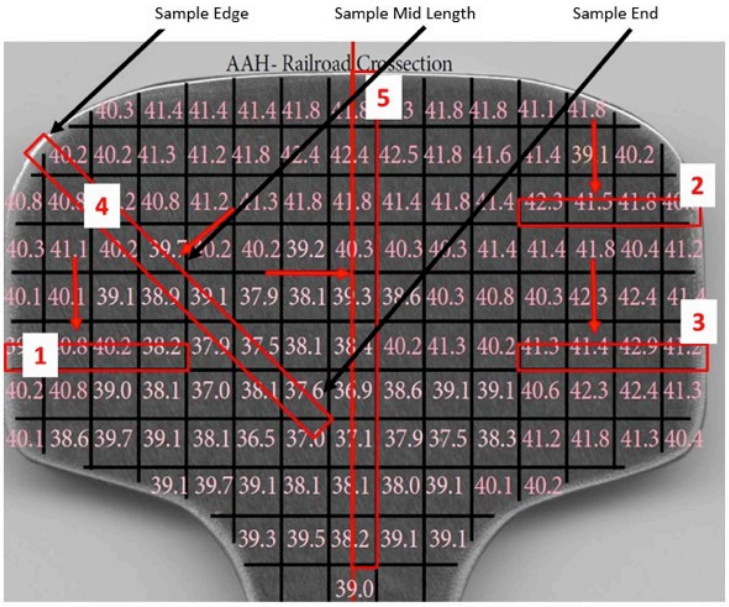

Figure 7. The location and viewing direction of five metallography samples that were removed from each rail

2.4.2 Results and Discussions

All five metallographic samples from each rail were initially examined along their entire viewing length. However, all samples showed similar microstructural features, so only results from Sample 4 of each rail are shown. Figure 8 through Figure 12 show the outer edge of Sample 4 for each rail. The rails exhibit a mixed ferrite/pearlite microstructure at the surface that eventually changed to a fully pearlitic microstructure with increasing distance from the rail running surface. The white phase is the ferrite, while the darker constituent is pearlite. The mixed ferrite/pearlite region is caused by decarburization that occurs during high temperature processing of the rails.

Figure 13 through Figure 17 show LOM photomicrographs of the microstructure at the mid-length of Sample 4 for each rail, and similar LOM photomicrographs are shown for the end of the sample in Figure 18 through Figure 22 (Figure 7 shows these locations.)

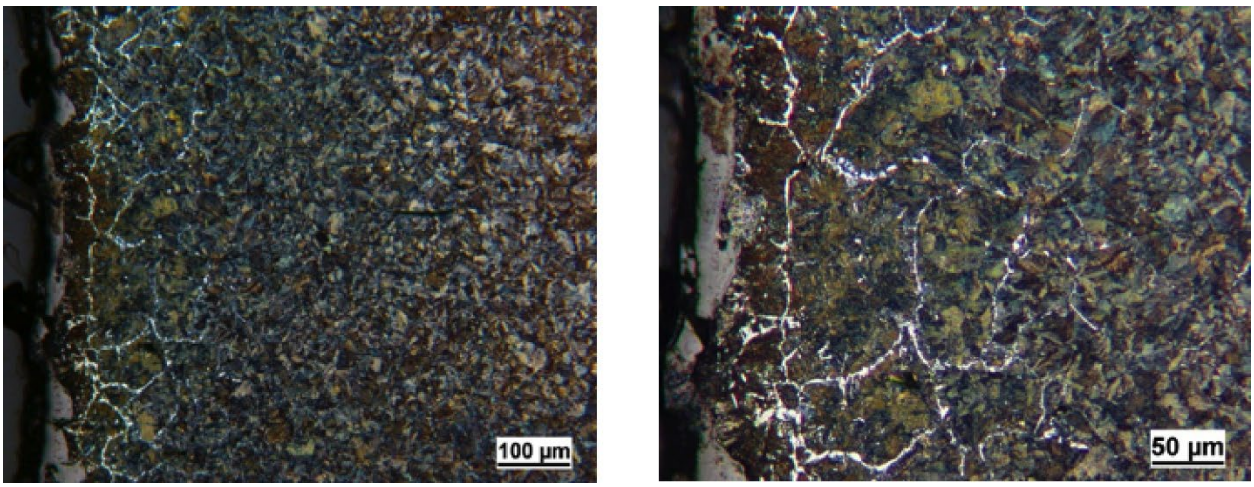

Figure 8. LOM photomicrographs of Sample 4 from HH rail as viewed at the outer edge of the sample

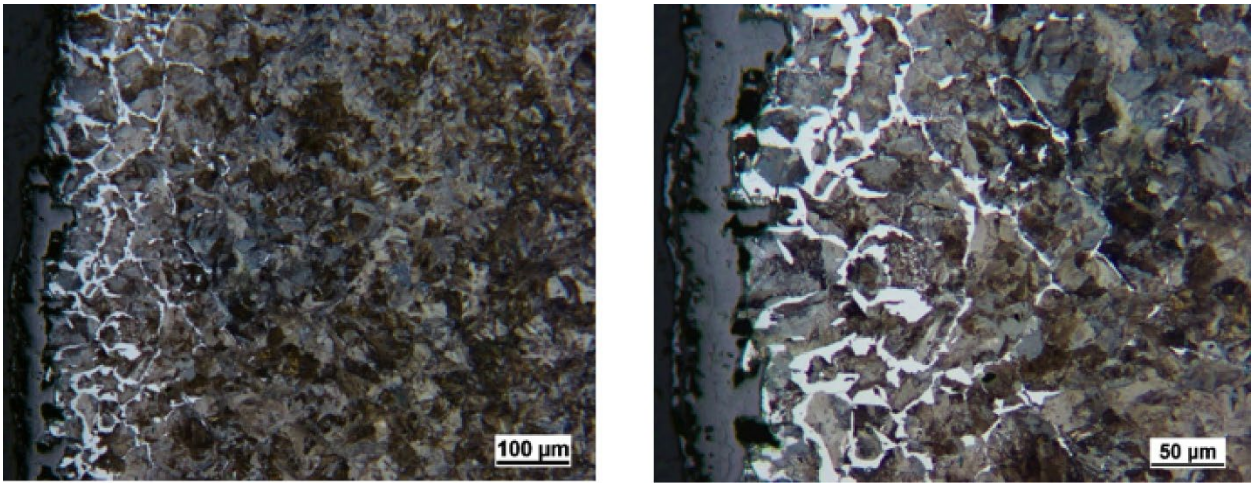

Figure 9. LOM photomicrographs of Sample 4 from SS rail as viewed at the outer edge of the sample

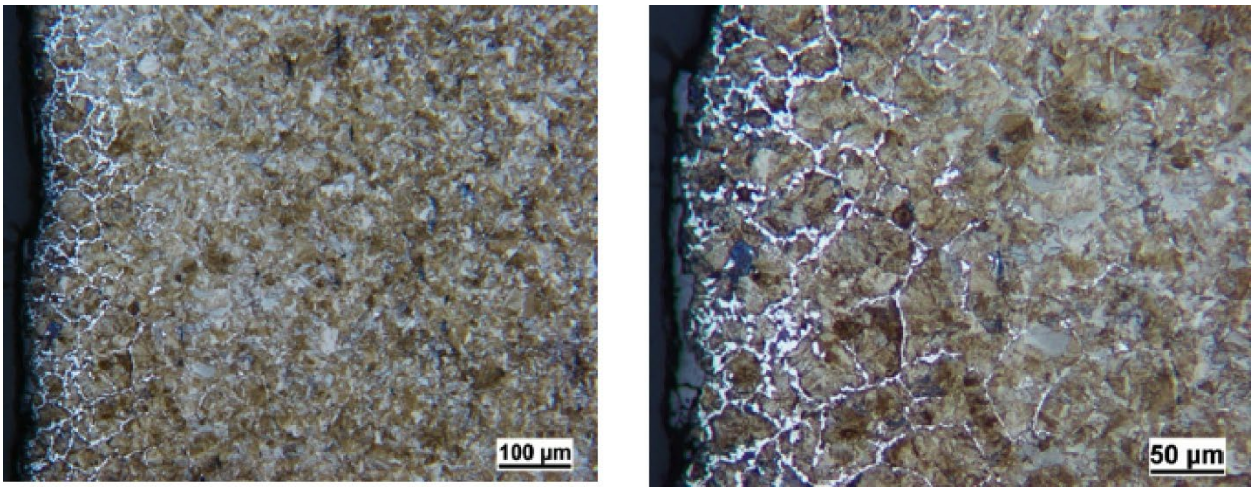

Figure 10. LOM photomicrographs of Sample 4 from AHH rail as viewed at the outer edge of the sample

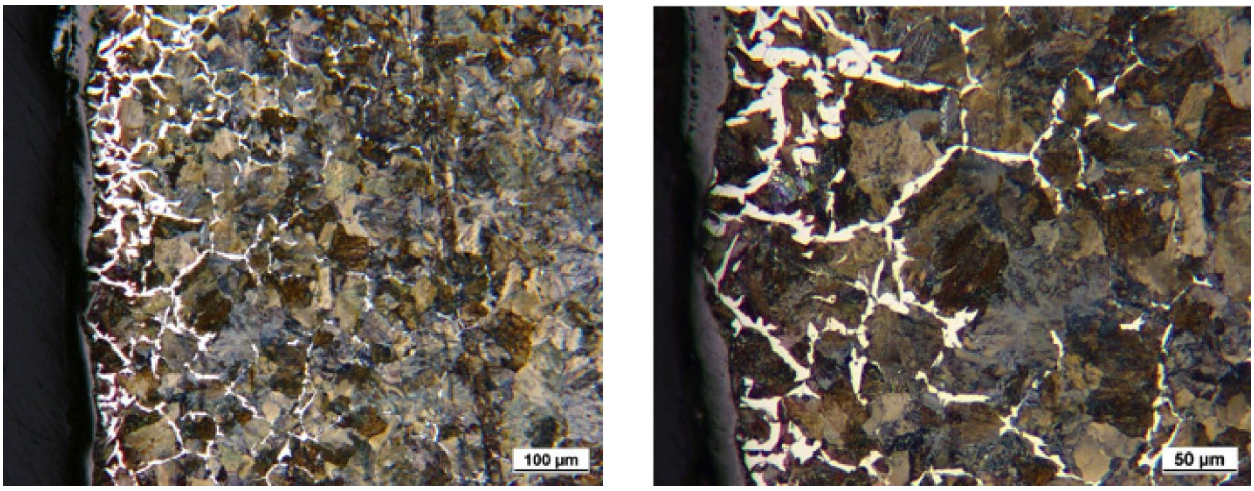

Figure 11. LOM photomicrographs of Sample 4 from CF&I77 rail as viewed at the outer edge of the sample

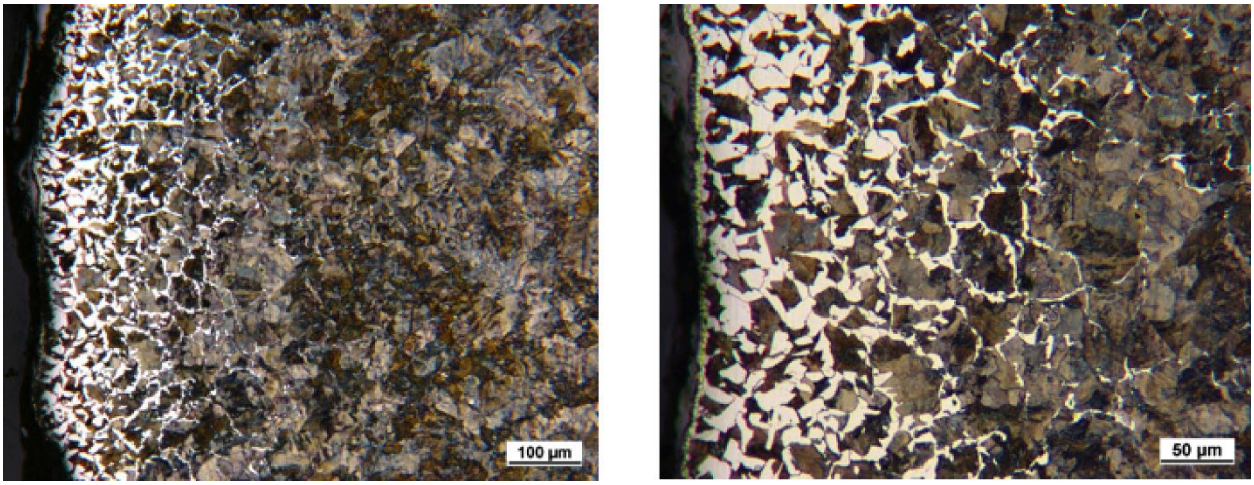

Figure 12. LOM photomicrographs of Sample 4 from HAY84 rail as viewed at the outer edge of the sample

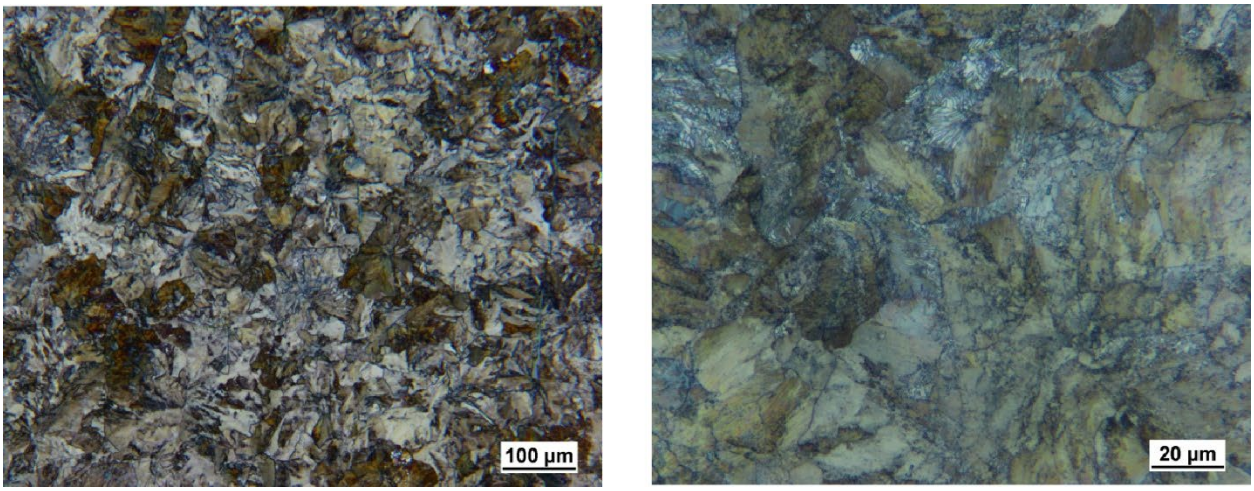

Figure 13. LOM photomicrographs of Sample 4 from SS rail as viewed at the mid length of the sample

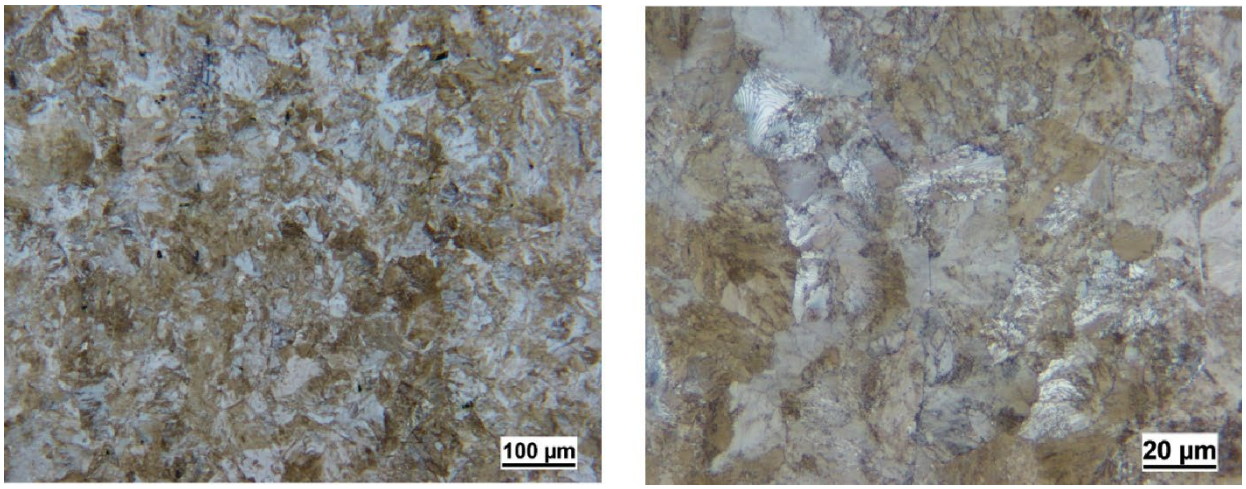

Figure 14. LOM photomicrographs of Sample 4 from HH rail as viewed at the mid length of the sample

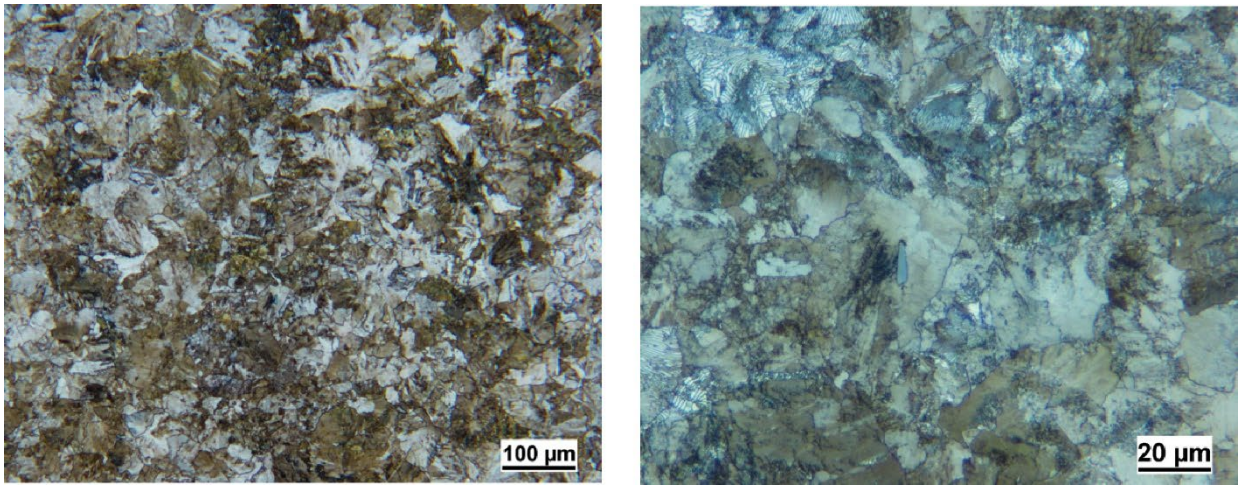

Figure 15. LOM photomicrographs of Sample 4 from AHH rail as viewed at the mid length of the sample

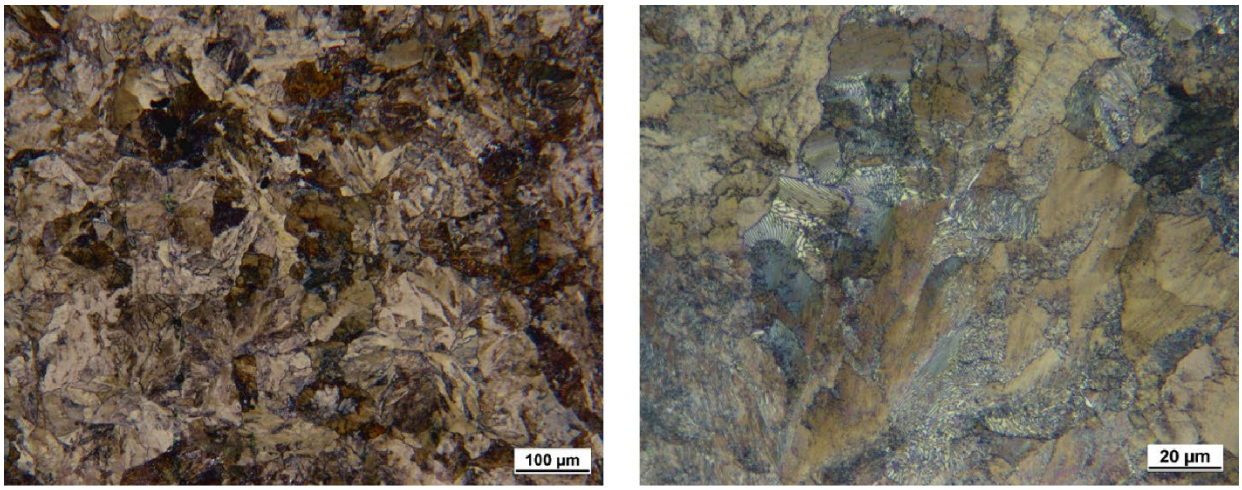

Figure 16. LOM photomicrographs of Sample 4 from CF&I77 rail as viewed at the mid length of the sample

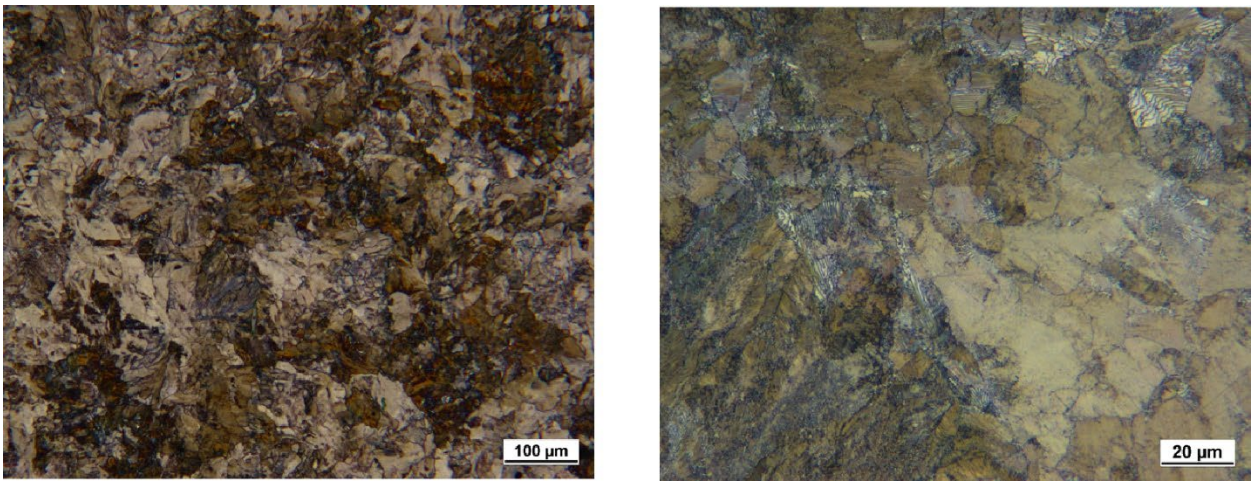

Figure 17. LOM photomicrographs of Sample 4 from HAY84 rail as viewed at the mid length of the sample

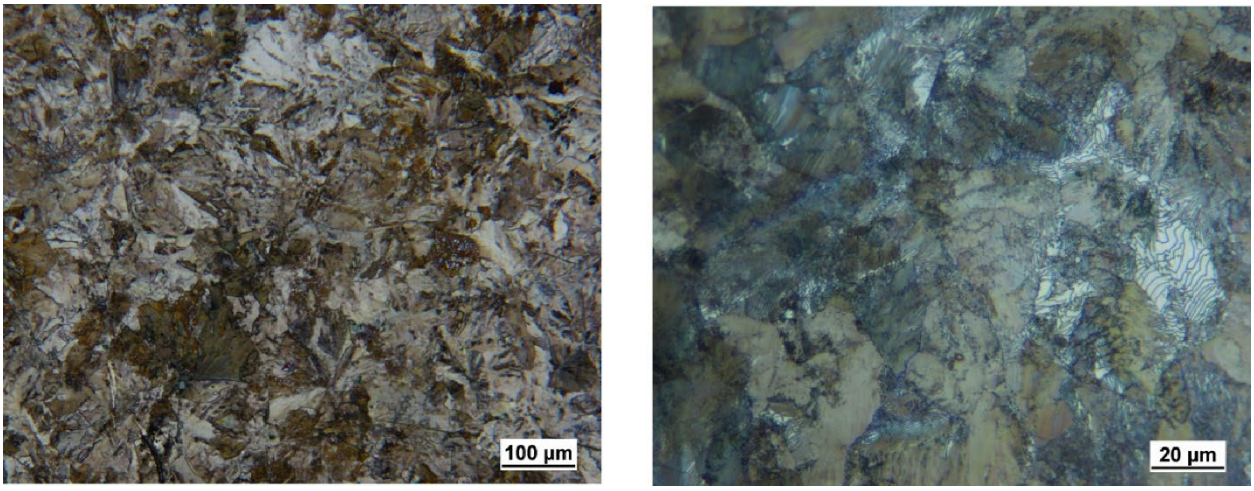

Figure 18. LOM photomicrographs of Sample 4 from SS rail as viewed at the end of the sample

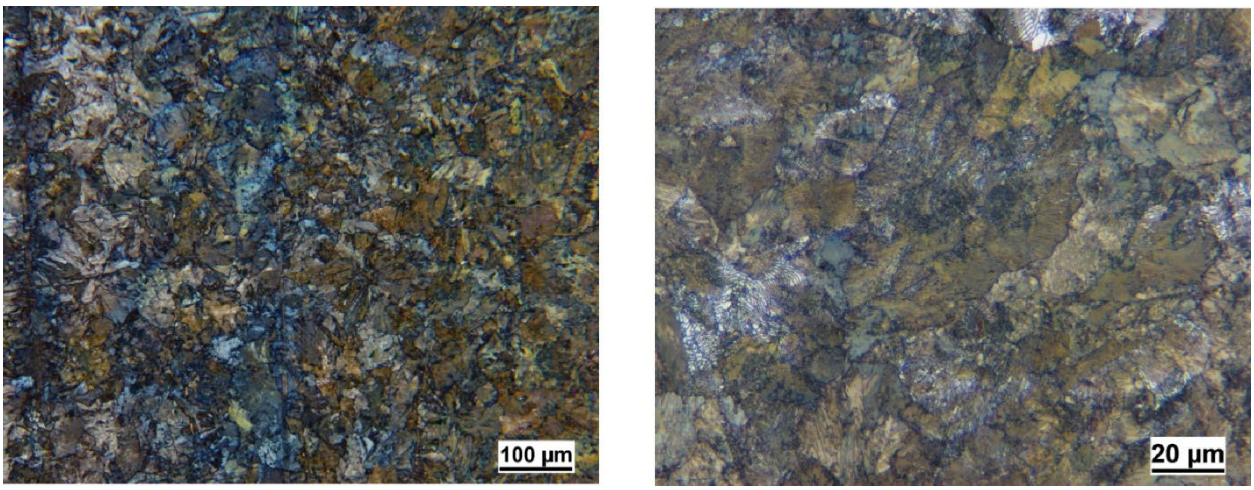

Figure 19. LOM photomicrographs of Sample 4 from HH rail as viewed at the end of the sample

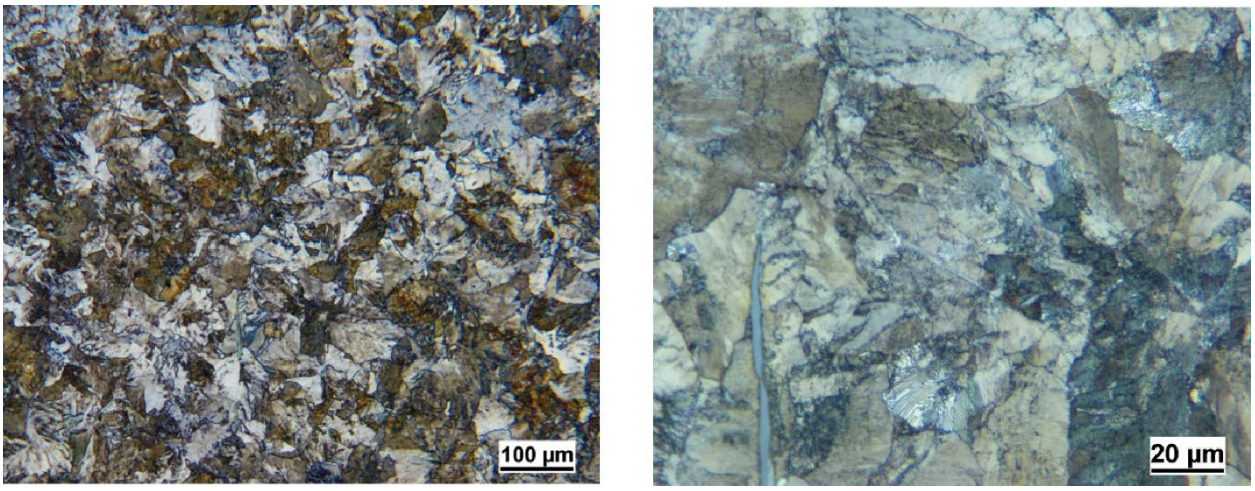

Figure 20. LOM photomicrographs of Sample 4 from AHH rail as viewed at the end of the sample

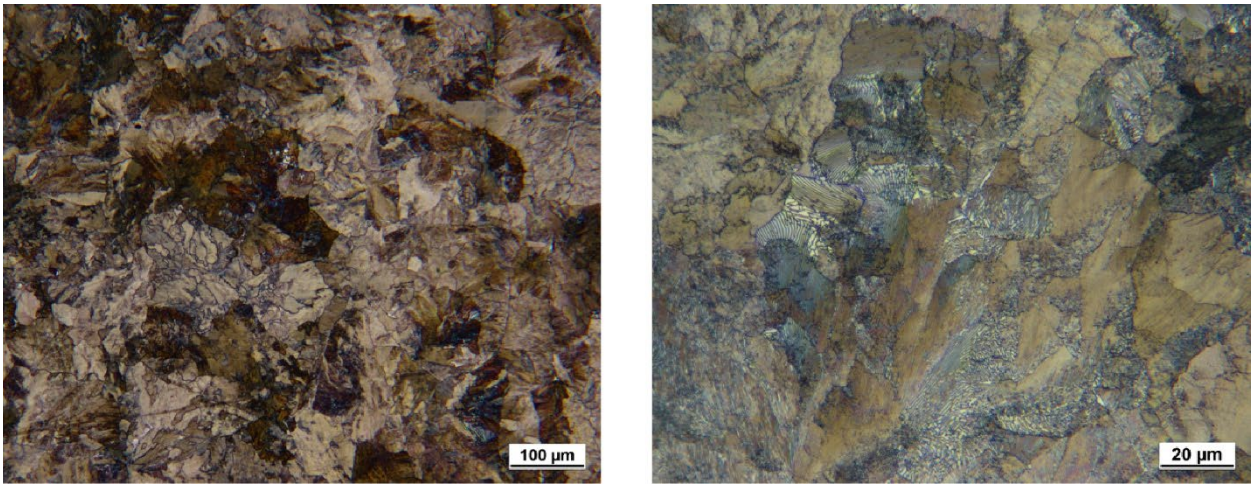

Figure 21. LOM photomicrographs of Sample 4 from CF&I77 rail as viewed at the end of the sample

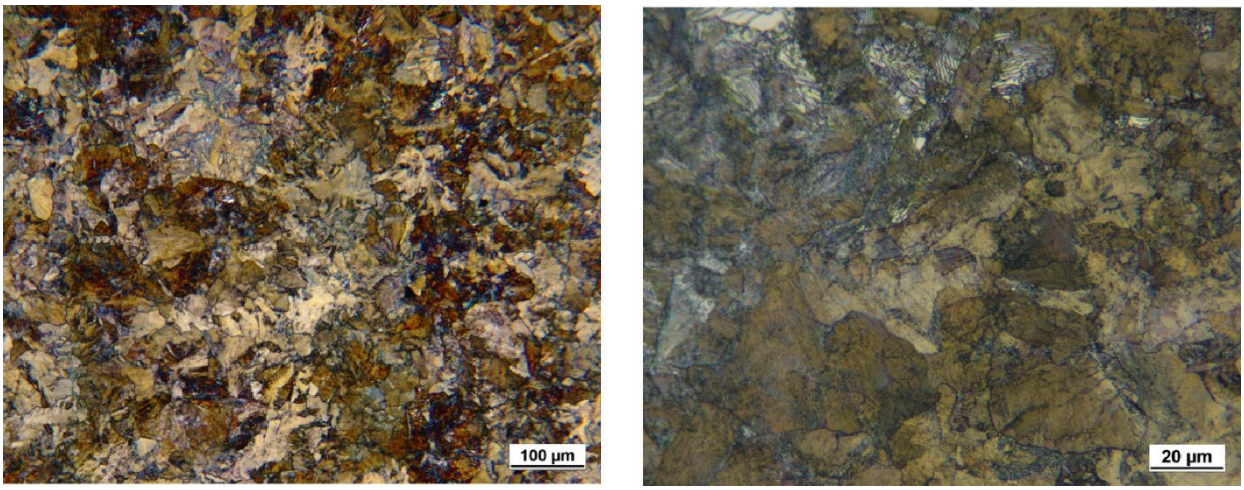

Figure 22. LOM photomicrographs of Sample 4 from HAY84 rail as viewed at the end of the sample

The SS, HH, and AHH rails were also examined by SEM at the same locations (surface, mid-length, end) on Sample 4 for each rail (Figure 23 through Figure 31). In the low magnification SEM photographs on the left-hand side of Figure 23 through Figure 25, the pro-eutectoid ferrite appears as dark bands. Examples of the ferrite and pearlite are labeled for the SS rail in the higher magnification image on the right-hand side of Figure 23, where the two-phase cementite and ferrite mixture of the pearlite is readily resolved.

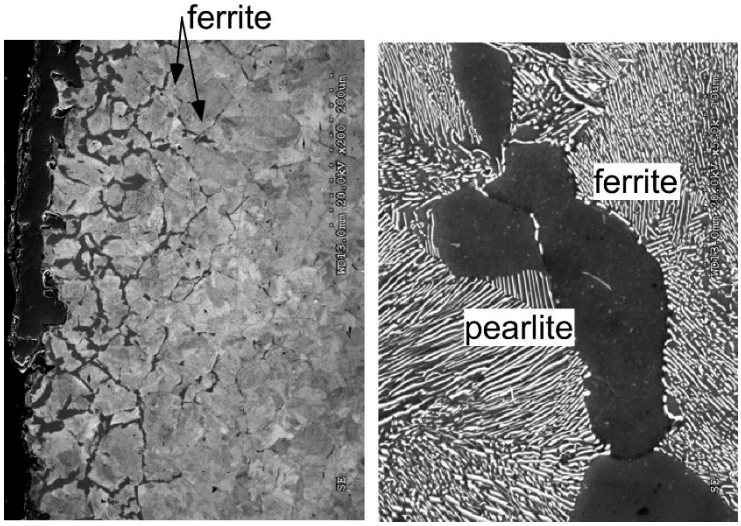

Figure 23. SEM photomicrographs of Sample 4 from SS rail as viewed at outer edge of sample

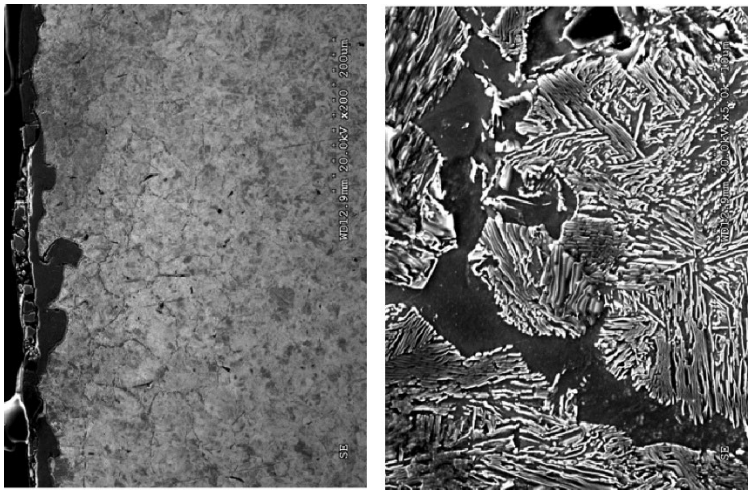

Figure 24. SEM photomicrographs of Sample 4 from HH rail as viewed at outer edge of sample

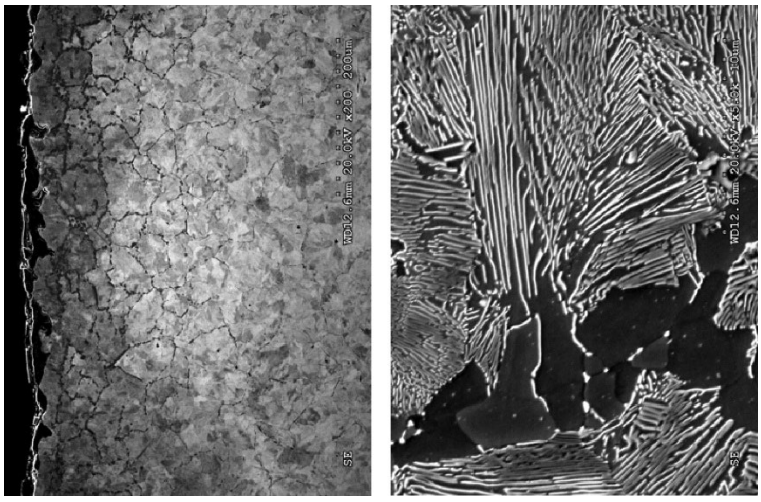

Figure 25. SEM photomicrographs of Sample 4 from AHH rail as viewed at outer edge of sample

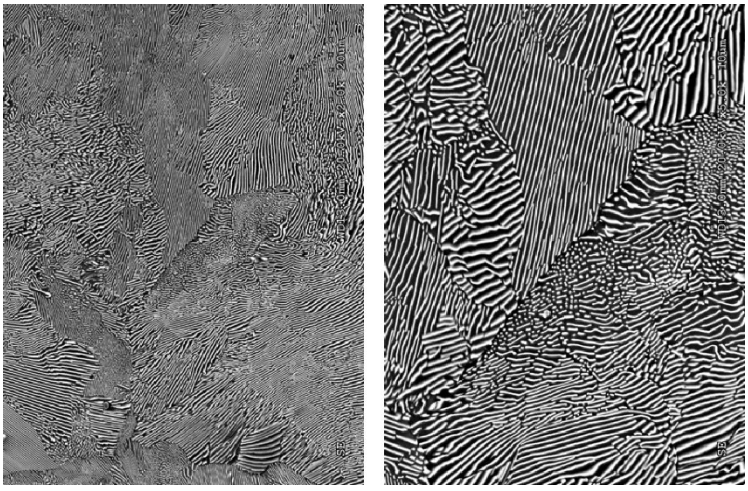

Figure 26. SEM photomicrographs of Sample 4 from SS rail as viewed at mid length of sample

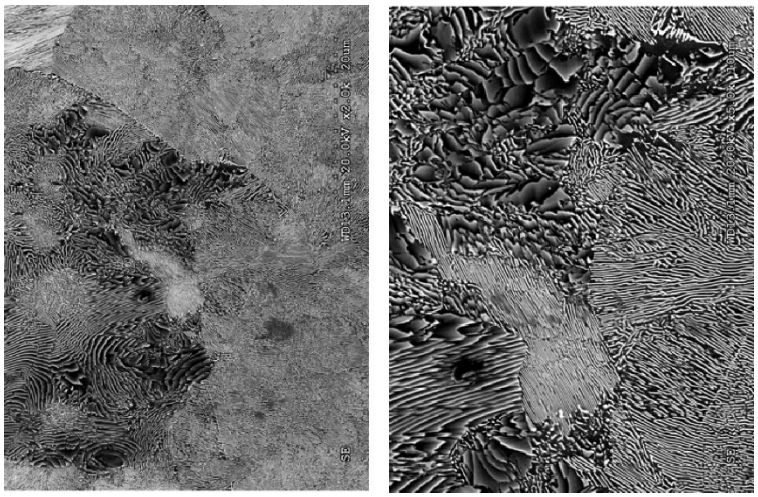

Figure 27. SEM photomicrographs of Sample 4 from HH rail as viewed at mid length of sample

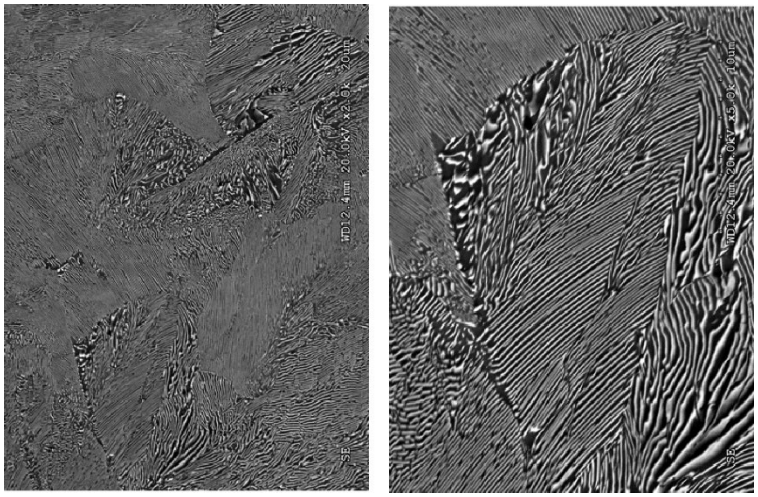

Figure 28. SEM photomicrographs of Sample 4 from AHH rail as viewed at the mid length of the sample

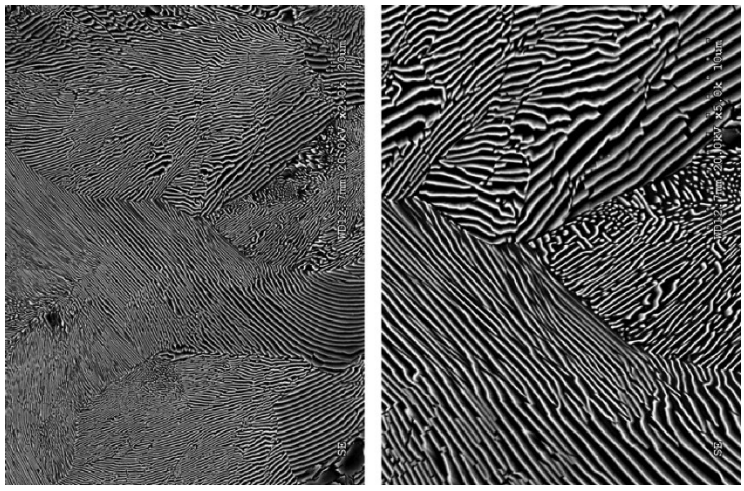

Figure 29. SEM photomicrographs of Sample 4 from SS rail as viewed at the end of sample

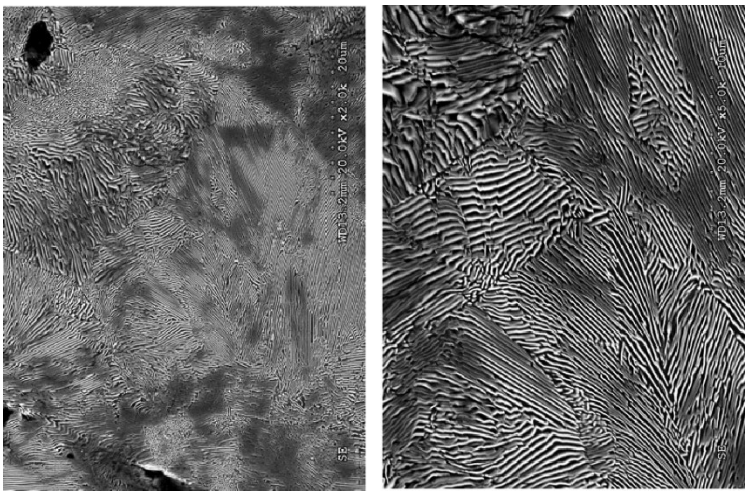

Figure 30. SEM photomicrographs of Sample 4 from HH rail as viewed at the end of sample

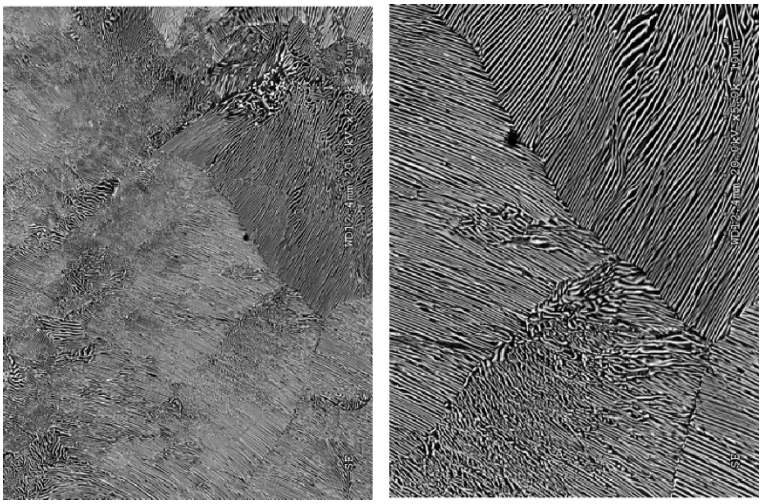

Figure 31. SEM photomicrographs of Sample 4 from AHH rail as viewed at the end of sample

Figure 32 through Figure 34 show the results of microhardness traces conducted from the surface to the interior of Sample 4 for the SS, HH, and AHH rails. As expected, the decarburization layer at the surface results in a local decrease in hardness that is about 1 mm in length.

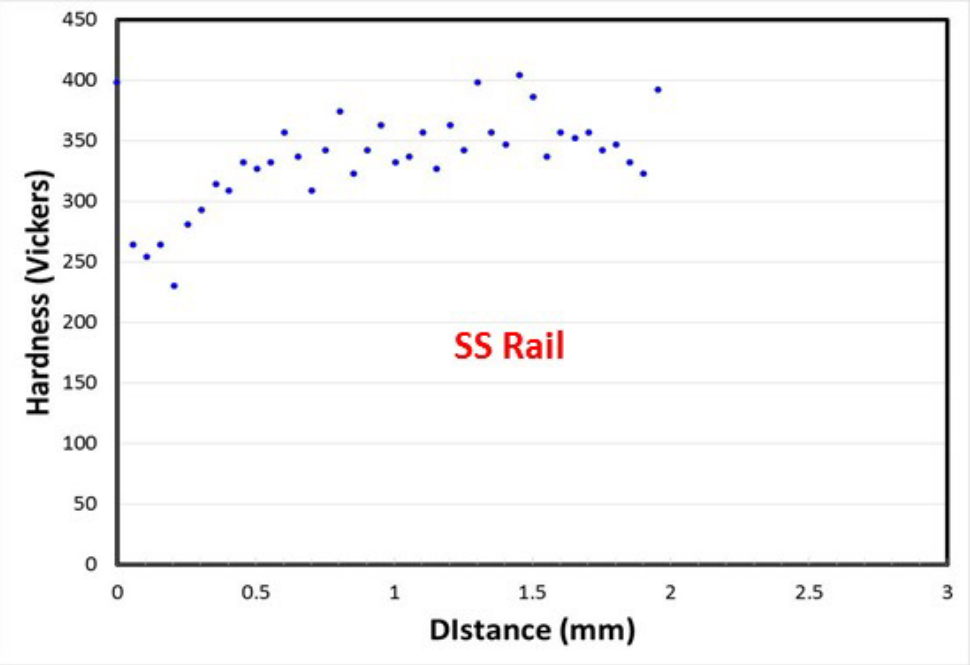

Figure 32. Variation in microhardness near the outer edge of the SS rail for Sample 4

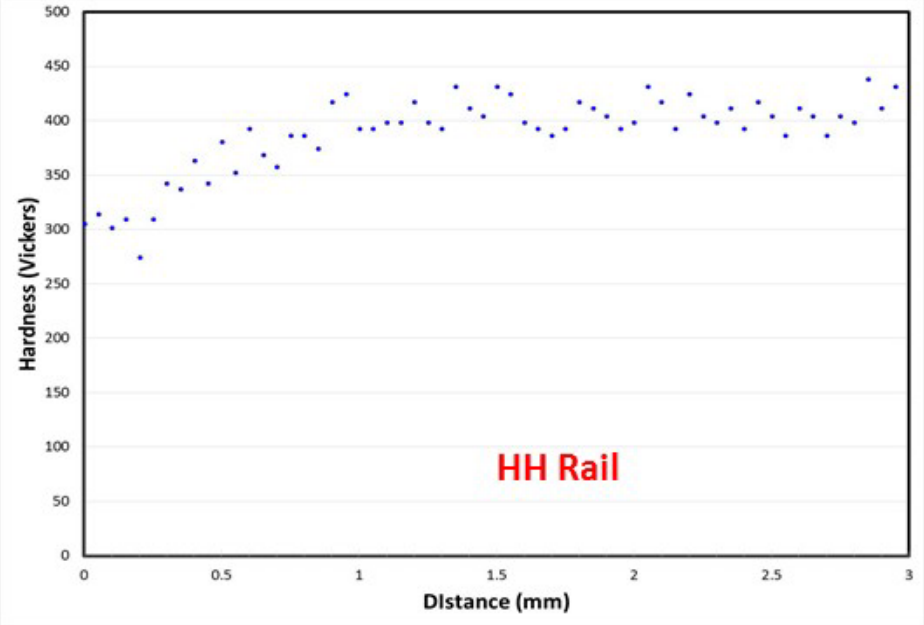

Figure 33. Variation in microhardness near the outer edge of the HH rail for Sample 4

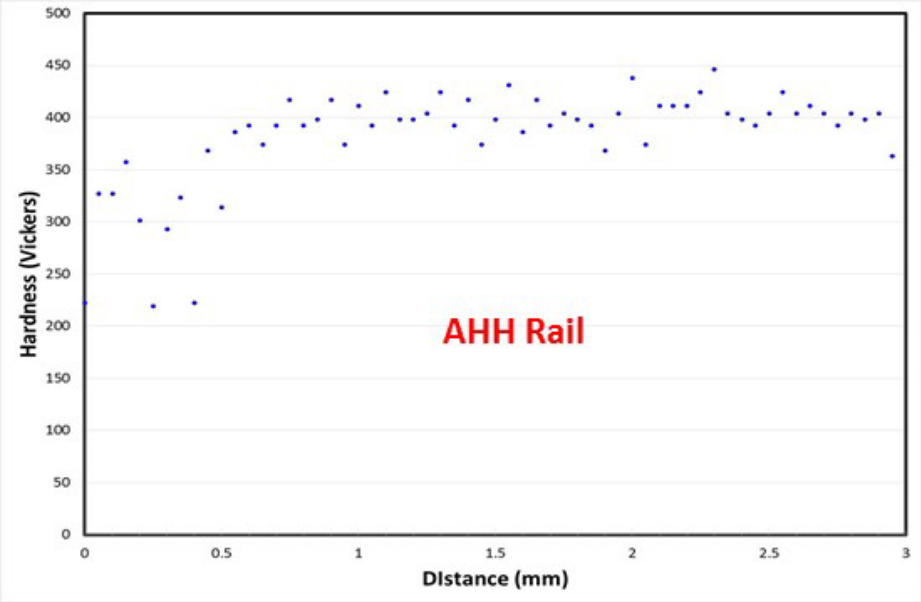

Figure 34. Variation in microhardness near the outer edge of the AHH rail for Sample 4

Inclusions were also observed in the rails (Figure 35) that were acquired in the as-polished condition for Sample 4 on the SS rail. Two types of inclusions were observed. One inclusion type had a grey color and was elongated in the longitudinal direction of the rail. The second type of inclusion exhibited an orange appearance and was more equiaxed in shape.

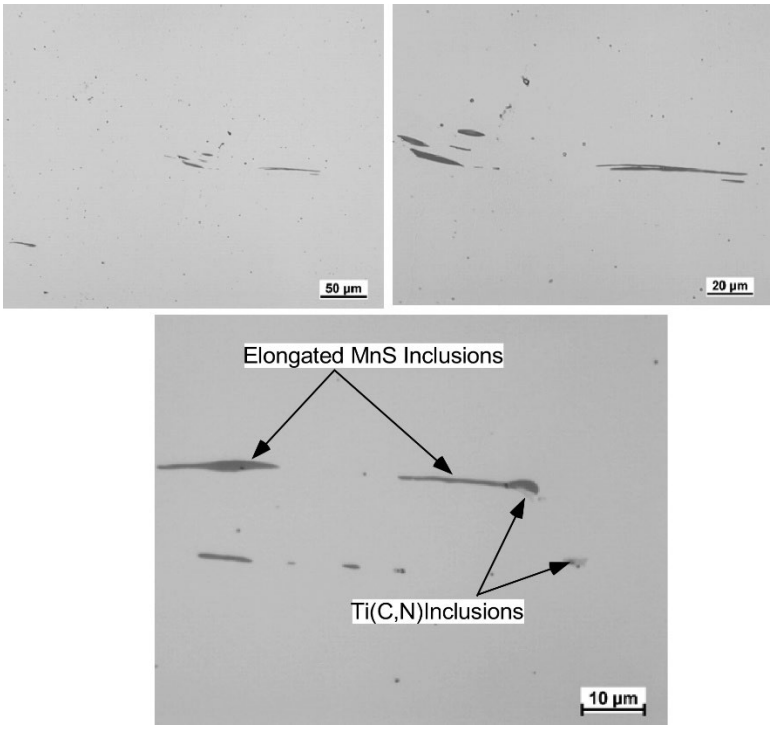

Figure 35. LOM images acquired in as-polished condition showing typical inclusions observed in rails (Sample 4, SS Rail)

Higher magnification SEM images and Energy Dispersive Spectrometry (EDS) spectra of these phases are shown in Figures 36 and 37 (the red + sign in the SEM images denote the locations where the EDS spectra were acquired). The elongated particles are enriched in manganese (Mn) and sulfur (S), while the equiaxed particles are enriched in titanium (Ti). The elongated inclusions are MnS inclusions that are typically observed in steel. The Ti rich inclusions are likely titanium carbo-nitrides that form from the melt at the start of solidification of the ingot. The MnS inclusions are elongated along the length of the rail (i.e., perpendicular to the fatigue crack growth plane) and are therefore unlikely to have any significant effect on fatigue resistance. Similarly, the Ti rich inclusions are equiaxed and present in very small quantities, and therefore also unlikely to have any detrimental effect on fatigue properties.

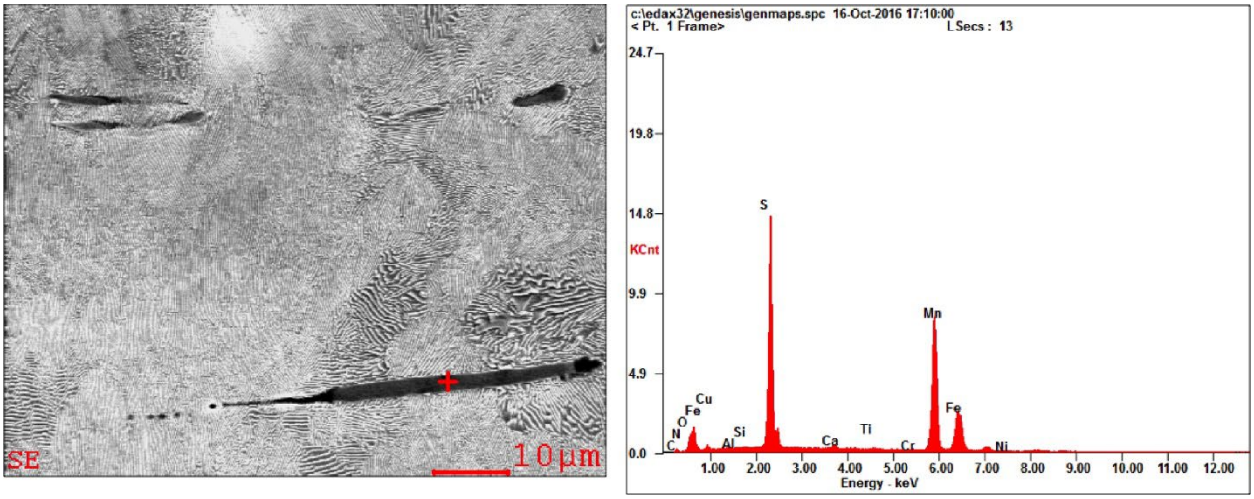

Figure 36. SEM photomicrograph (left) and corresponding EDS spectrum (right) of typical MnS inclusions observed in rails (SS Rail, Sample 4)

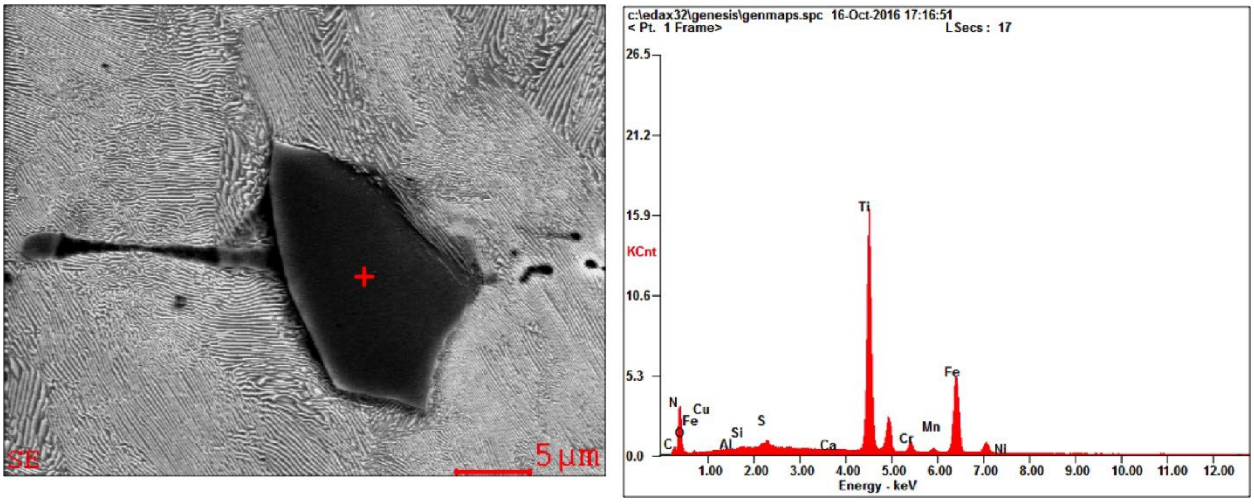

Figure 37. SEM photomicrograph (top) and corresponding EDS spectrum (bottom) of typical Ti rich inclusions observed in rails (SS Rail, Sample 4)

The chemical composition of the rails is designed to produce a fully pearlitic microstructure. The mixed ferrite/pearlite microstructure associated with the surface of the rail is associated with decarburization that occurs during high temperature processing. This decarburization results in a local depletion of carbon near the surface. As a result of this local reduction in carbon

concentration, pro-eutectoid ferrite precipitates from austenite during cooling. This accounts for the mixed ferrite/pearlite microstructure observed at the rail surfaces. The ferrite is softer than the pearlite due to reduced carbon and the associated absence of the hard cementite phase, and this accounts for the reduced hardness observed within the decarburized layer at the surface. Beyond the decarburized region, the carbon content of the rail is at the eutectoid composition, and the austenite transforms fully to pearlite during cooling from the processing temperature.

The hardness and strength of pearlite increases with decreasing pearlite spacing. The pearlite spacing, in turn, is controlled primarily by the cooling rate during the austenite-to-pearlite transformation and the alloy content of the steel. Higher cooling rates and additions of substitutional alloying elements such as vanadium (V) and titanium (Ti) decrease the pearlite spacing. It should be noted that accurate pearlite spacing measurements require extensive sampling and measurements that were beyond the scope of this project. During cooling of the rail from the processing temperature, the cooling rate will be highest at the surface and decrease with increasing distance from the surface. This variation in cooling rate accounts for the relatively high hardnesses observed near the rail surfaces and decrease in hardness with increasing distance from the surface. Of the modern rails, the SS rail exhibited the lowest hardness and strength, followed by increasing hardness/strength for the HH and then AHH rails. These differences can be attributed to the higher alloying elements (V and Ti) associated with these rails. During the austenite to pearlite transformation, the alloying elements must partition between the ferrite and cementite phases, and this process is diffusion controlled. The diffusion rate of the relatively larger V and Ti substitutional alloying elements is significantly slower than that of carbon, which diffuses interstitially. As a result, the diffusion distance during the austenite-to-pearlite transformation is reduced with the addition alloying elements, which reduces the pearlite spacing. This likely accounts for the higher hardness and strength observed for the HH and AHH rails.

2.5 Tensile Testing

Uniaxial tensile tests were conducted on the modern rails and legacy rails to compare uniaxial tensile properties among the different rail types and check for possible correlations with microstructural observations and residual stress measurements.

2.5.1 Sample Preparation

Uniaxial tensile specimens were machined from nine different 1/4 in thick plates, cut from each of the rail cross sections, as shown in Figure 38. The flat tensile test specimens were prepared in accordance with ASTM E8 standards using 1 in gauge lengths. The other dimensions for the tensile specimen are given in Table 7. The tensile specimens were cut from long plates that were oriented with respect to the rails' primary axis, plates that may have contained significant internal residual stresses in the axial direction. However, the team believed that the residual stresses in the gauge length of the tensile specimens were minimal due to the relatively small thickness and width dimensions (6 mm x 6 mm) in the gauge length.

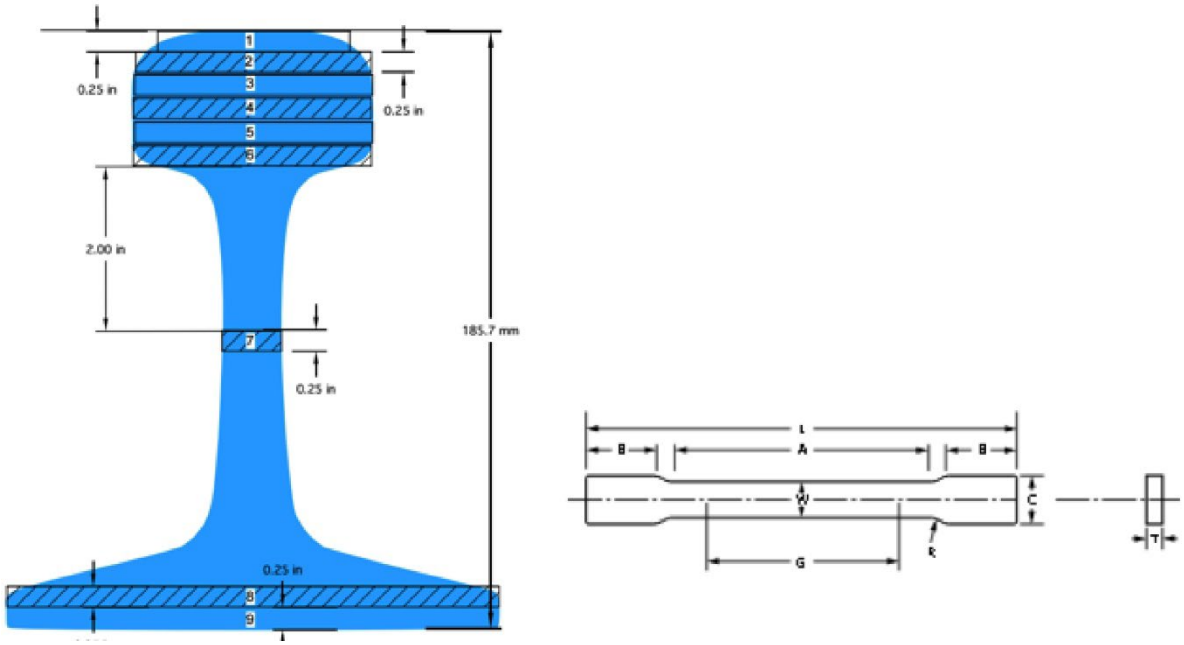

Figure 38. ASTM E8 tensile specimens cut from specific vertical locations in 136RE rails

Table 7. Tensile Specimen Dimensions

	G Gauge Length	W Width	T Thickness	R Radius of fillet	L Overall Length	B Length of Grip	C Width of grip
Specimen Dimensions mm [in]	25 [1]	6 [0.25]	6 [0.25]	6 [0.25]	100 [4]	30 [1.25]	10 [0.375]

2.5.2 Uniaxial Stress-Strain Curves

A total of 45 tensile tests were conducted (5 rails, 9 tensile specimens per rail). In these tests, the engineering stress (force per unit original undeformed area) and engineering strain ($\Delta L / L$) within the gauge length were measured using a clip-on extensometer and recorded. As described in Appendix B, Figure 113, the standard offset method was used to determine the tensile yield strength in accordance with the ASTM E8 standards. The individual stress/strain curves, taken from layer 2 for each of the railheads (see Figure 38), are given in Figures 114–118. Figure 39 compares the uniaxial tensile behavior from all tests on a single plot. The figure shows that the modern head hardened rails exhibit significantly higher yield and ultimate tensile strength. Figure 40 gives the Young's modulus at different depths in each of the rails, in addition to the rails' average Young's modulus (figure legend). Figure 41 shows the variation in the uniaxial yield strength as a function of depth from the surface of the railhead for the five rails. The AHH rail exhibited the highest yield strength at all depths. The yield strength close to the AHH's running surface is approximately 345 MPa (50 ksi) greater than the yield strength observed in the CF&I77 rail at the same location. The variation in the yield strength between the head region and the base for all of the rails is noteworthy. For example, in the AHH rail, the yield strength decreased from a maximum of 862 MPa (125 ksi) slightly below the running surface to a yield strength of 689 MPa (100 ksi) in the rail base.

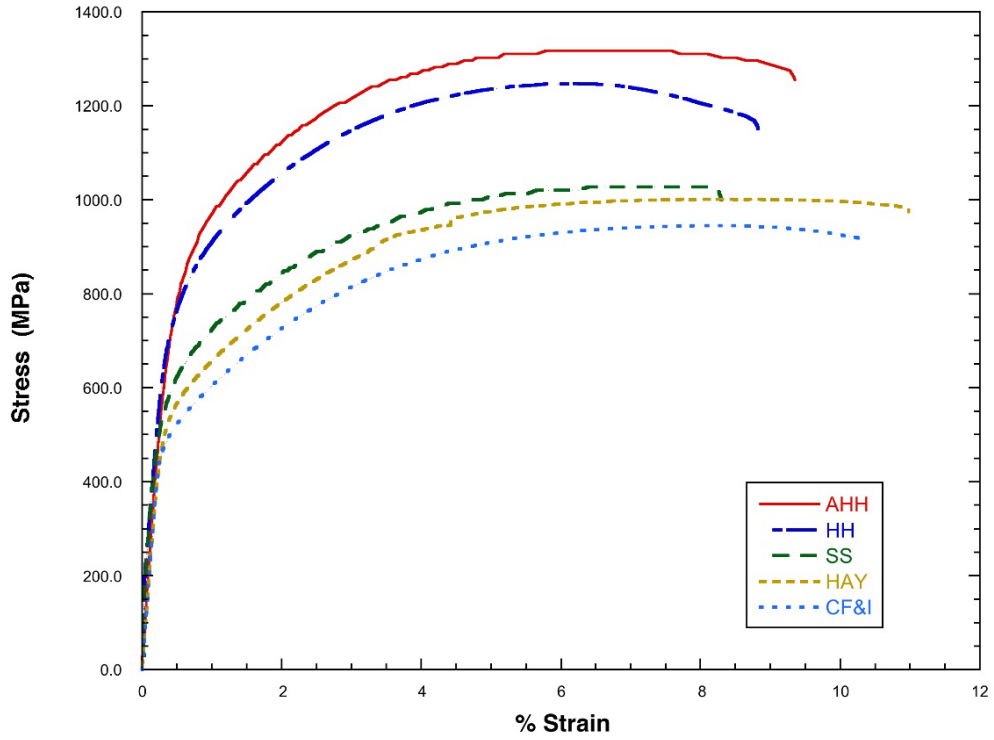

Figure 39. Comparison of uniaxial tensile behavior at a specific location (layer 2) for all rails

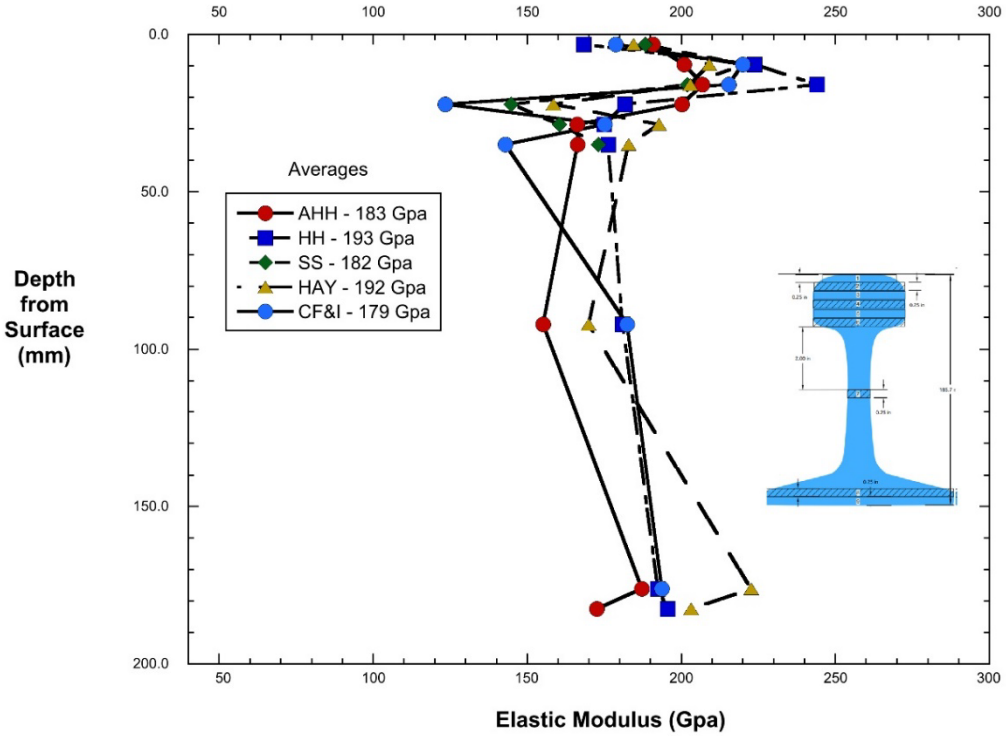

Figure 40. Young's Modulus as a function of depth measured from the railhead running surface

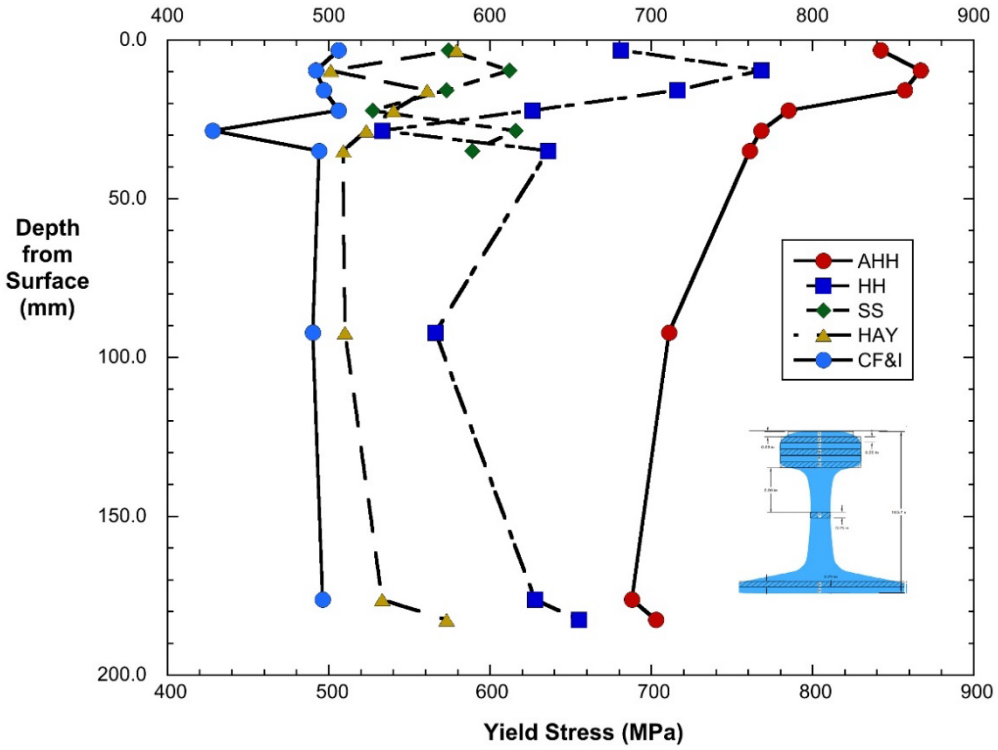

Figure 41. Uniaxial yield stress as a function of depth measured from the railhead running surface

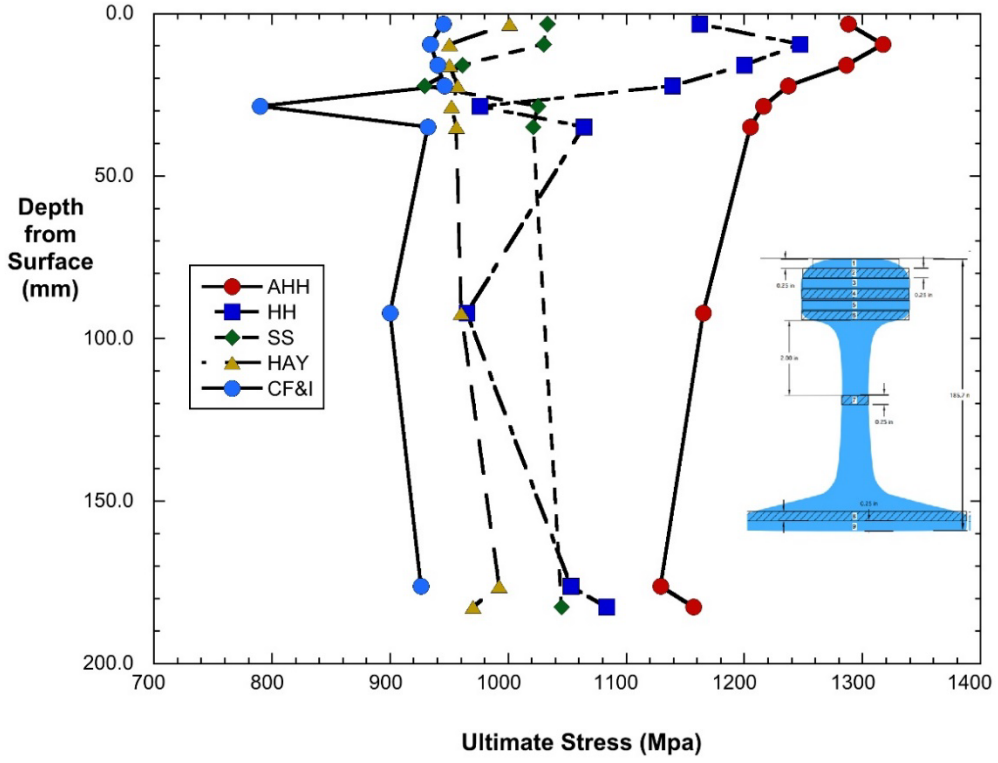

Figure 42. Ultimate tensile strength as a function of depth measured from the railhead running surface

As observed in Figure 42, the ultimate tensile strength has a spatial variation with respect to depth that is very similar to that seen in the yield strength plot (Figure 41). As expected, the greatest ultimate tensile strength was measured close to the surface of the AHH rail, with a maximum ultimate strength > 1,310 MPa (190 ksi). For comparison, the legacy rails (HAY84, CF&I77) exhibited ultimate tensile strengths generally below 965 MPa (140 ksi) in the railhead.

Both yield and tensile strength data collected here were compared to previously collected data documented by Orringer, et al. [11]. The results obtained here are consistent with the past results, except in the case of the AHH rail, which exceeds strength of previously investigated rails [11]. In addition, tensile tests of modern rails were conducted by AM following the AREMA specification for rails (including specimen locations). The SS rail had a yield strength of 690 MPa (100 ksi), a tensile strength of 1100 MPa (160 ksi), and an elongation of 9 percent, which meets the AREMA standard for standard strength carbon rail steel. The HH rail exhibited a yield strength of 880 MPa (128 ksi), a tensile strength of 1310 MPa (190 ksi), and an elongation of 10 percent. These measurements confirmed that the HH rail meets the AREMA high-strength carbon rail requirements (830 MPa [120 ksi] minimum yield strength, 171 ksi [1180 MPa] minimum tensile strength, and 10 percent minimum elongation). Finally, the AHH rail used in this study had a yield strength of 960 MPa (139 ksi), a tensile strength of 1380 MPa (200 ksi), and an elongation of 10 percent, all of which are typical for this high-strength rail.

2.6 Fracture Toughness Testing

A prime objective in this study was to measure the fracture toughness of different rail types and determine the variation in the fracture toughness with respect to position and orientation in the railhead.

2.6.1 Specimen Preparation

Most of the fracture and fatigue tests conducted in this study used CT test specimens (Figure 43). The test specimens were prepared following ASTM E399 and E647 standards. For valid fracture toughness (K_{IC}) measurements, conditions of small-scale yielding must be maintained. This is ensured by using a test specimen with sufficient thickness to maintain plane strain conditions along the bulk of the crack front. The size of the yield zone at the crack tip depends on the magnitude of K_{IC}, as well as the uniaxial yield strength σ_Y. Thus, it is not possible to know in advance whether a fracture toughness test is valid until after a provisional K_{IC} has been measured and a check made to ensure that conditions of small-scale yielding have been satisfied. The ASTM requirements for valid plane strain fracture toughness measurements are:

$$a \geq 2.5\left(\frac{K_{IC}}{\sigma_Y}\right)^2 \tag{0.0.1}$$

$$B \geq 2.5\left(\frac{K_{IC}}{\sigma_Y}\right)^2 \tag{0.0.2}$$

$$W \geq 5.0\left(\frac{K_{IC}}{\sigma_Y}\right)^2, \qquad (0.0.3)$$

where a is the distance from the center of the pin holes to the crack tip, B the specimen thickness, and W the width distance from the pin holes to the back edge of the specimen. Based on previously reported values for rail fracture toughness, the research team assumed that the largest K_{IC} values would probably be less than 40 $\mathrm{MPa}\sqrt{\mathrm{m}}$. The uniaxial yield strength, as reported in Section 2.5, was estimated to be no less than 552 MPa and in most cases was considerably higher, e.g., the yield strength for the AHH rails is always greater than 690 MPa. Thus, a conservative thickness dimension suitable for the fracture toughness tests in this study was estimated to be 13 mm. The resulting overall dimensions for the main CT specimen used in the testing program is shown in Figure 43.

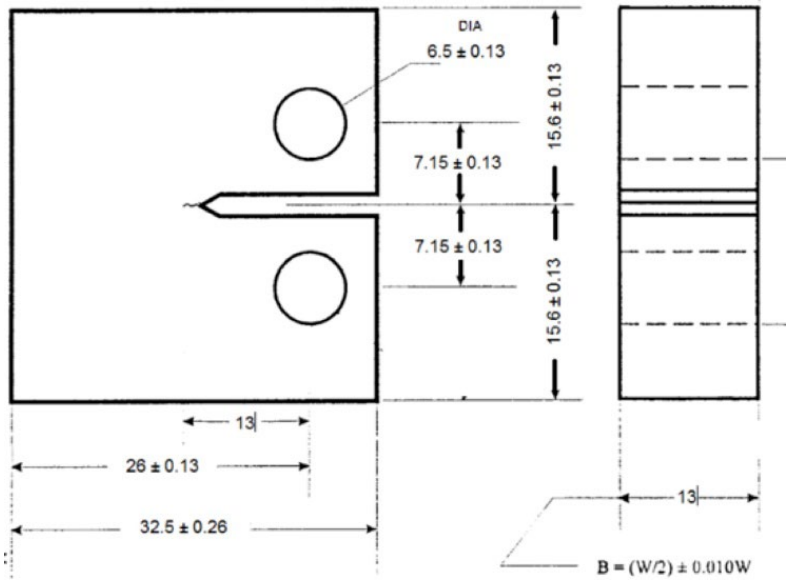

Figure 43. Compact tension (CT) specimen (dimensions in mm)

The team cut specimens in both horizontal and vertical orientations in an effort to determine the fracture toughness and fatigue behavior as a function of position and orientation in the five different rails examined For example, Figure 44 shows the orientation of CT specimens machined from horizontal plates cut at different depths within the railhead. Specimens were extracted along the center of the rail and to the left and right of center by waterjet cutting the specimens from plates of specified thickness as shown in Figure 45. The specimen layout shown in Figure 44 permitted fracture measurements both as a function of depth and lateral (off-center) position within the railhead. The relatively small size of the CT specimens minimized the magnitude of the residual stresses normal to the crack surface and thus the fracture measurements obtained with these specimens are primarily a function of local metallurgical properties and orientation.

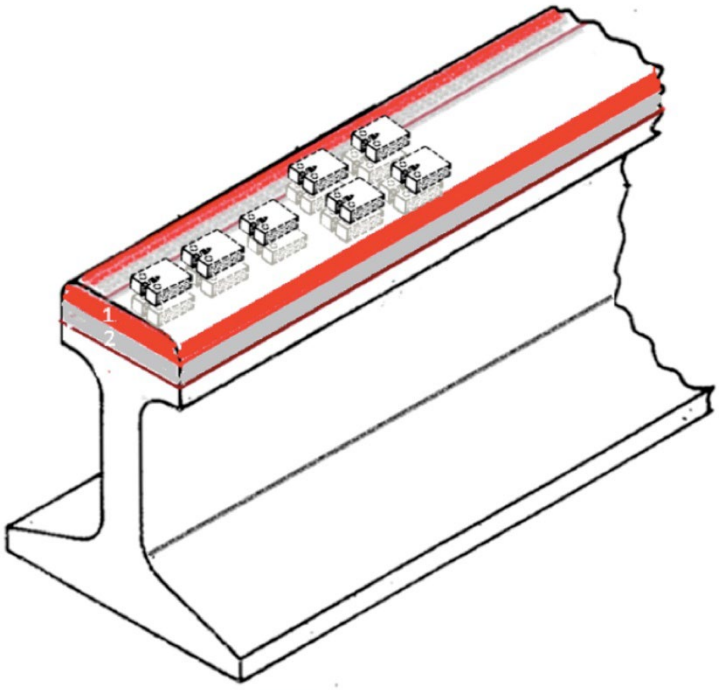

Figure 44. Orientation of CT specimens cut from horizontal slices in the railhead

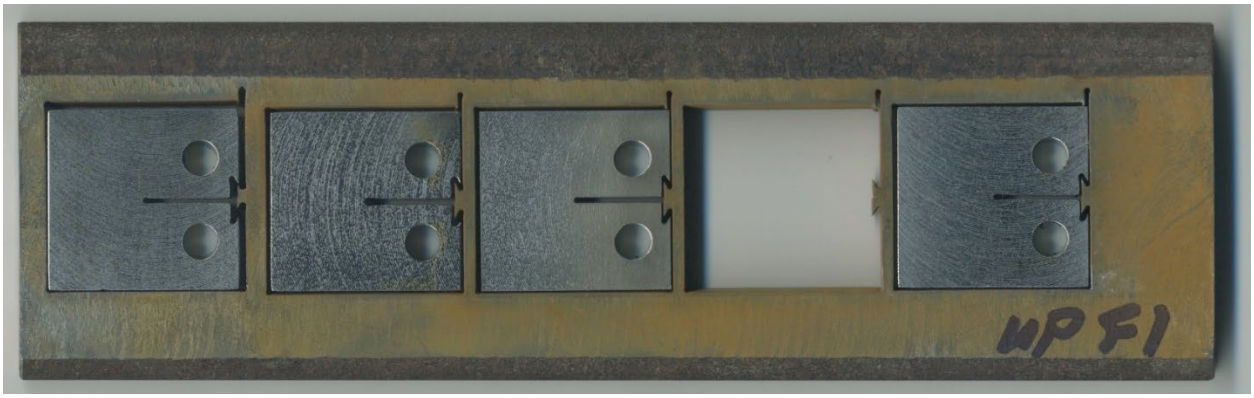

Figure 45. Single column of CT specimens waterjet cut from region close to the railhead running surface

Additional machining steps included milling the CT specimens to obtain flat surfaces, boring the pin loading holes, and cutting the notch. In the initial phases of the test program, notches were cut with a very fine (0.006 in.) diameter wire (EDM). However, the research team determined that waterjet cut notches (notch widths 0.020–0.030 in) were acceptable for the precracking process, especially if a fine jewelers saw (blade width 0.012 in) was used to make a fine saw cut at the base of the waterjet cut notch as shown in Figure 46. All CT fracture specimens were precracked in fatigue at $\Delta K = 16\ \text{MPa}\sqrt{\text{m}}$ to obtain a precrack length of $a = 12.5$ mm using sinusoidal loading at a frequency of 15–20 Hz. Figure 47 shows a polished CT specimen with a close-up image showing the fatigue crack growth from the tip of the notch. The photomicrograph in Figure 48 also clearly shows the precrack from the notch tip in a CT specimen.

Figure 46. Cutting sharp notch at the base of waterjet cut notch using jeweler's saw

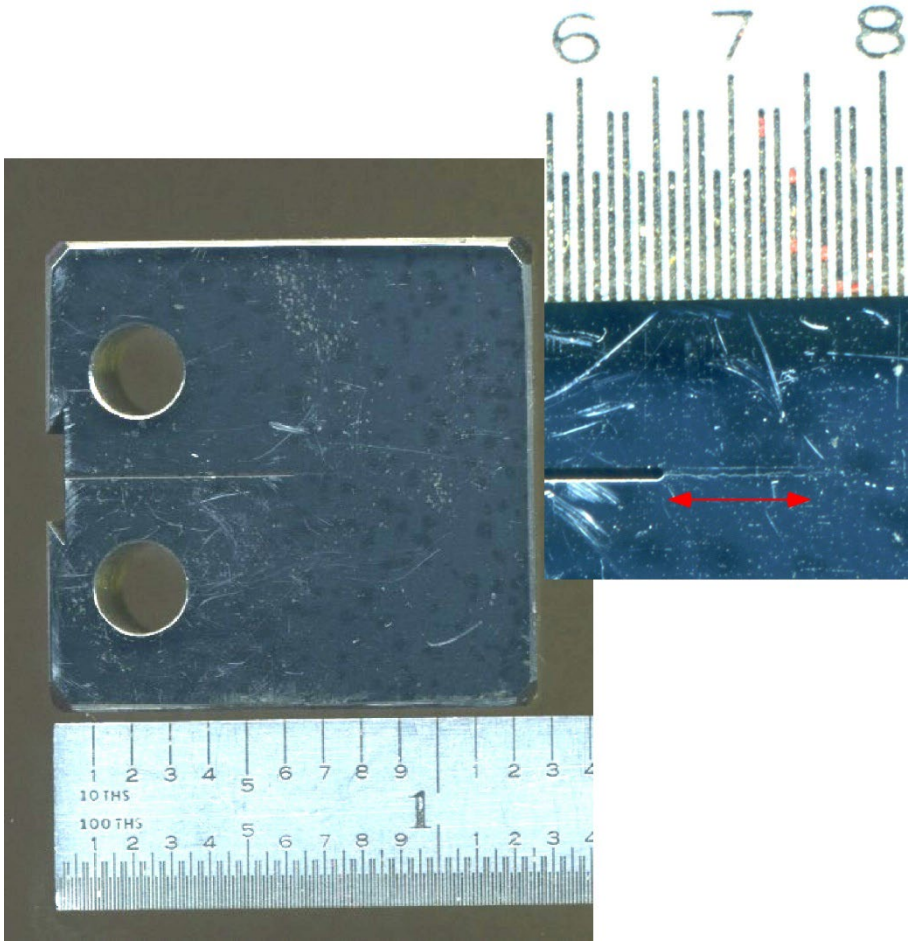

Figure 47. CT specimen with wire EDM notch and polished surface. Inset shows ~0.1 in. fatigue precrack at base of notch

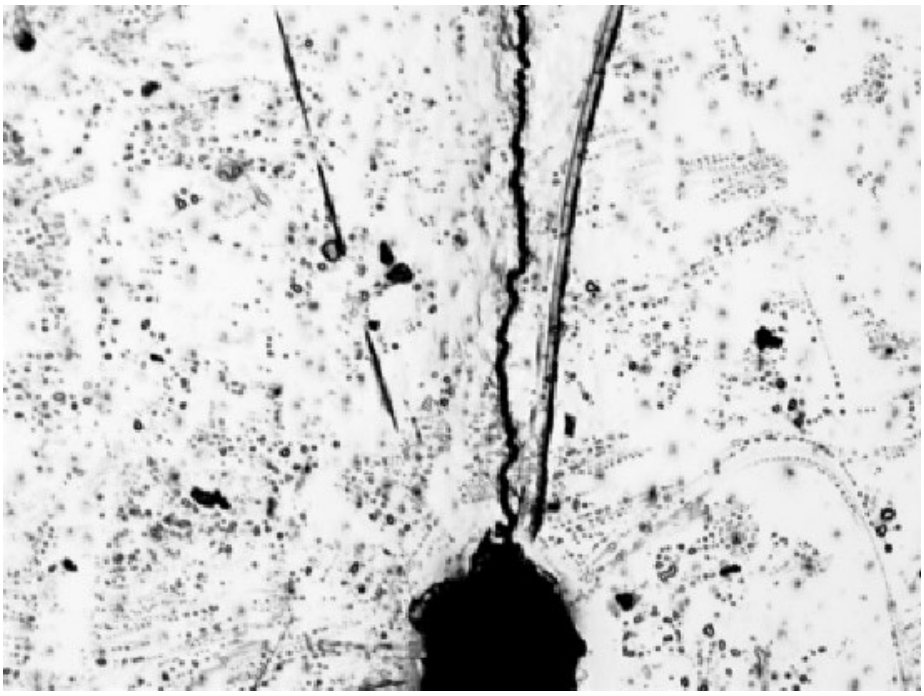

Figure 48. Photomicrograph showing precrack from notch tip in CT specimen

Following the ASTM E399 fracture toughness testing protocol, the load and crack opening displacement (COD) were monitored during the test to detect the proper type of crack "pop in" and advance that will ensure a valid K_{Ic} measurement. Figure 49 shows a typical CT specimen with the attached COD clip gauge during fracture toughness testing. Appendix C contains sample load vs COD measurements taken from valid K_{Ic} tests for the different rail types. This appendix also contains the CT formulas for K_1 and crack opening displacement δ_1. The formulas for K_1 and δ_1 are given as a polynomial function of the crack length a and applied load P. Thus, the crack length a and the stress intensity factor K_1 can be determined indirectly from the measured values of P and δ_1 during a test.

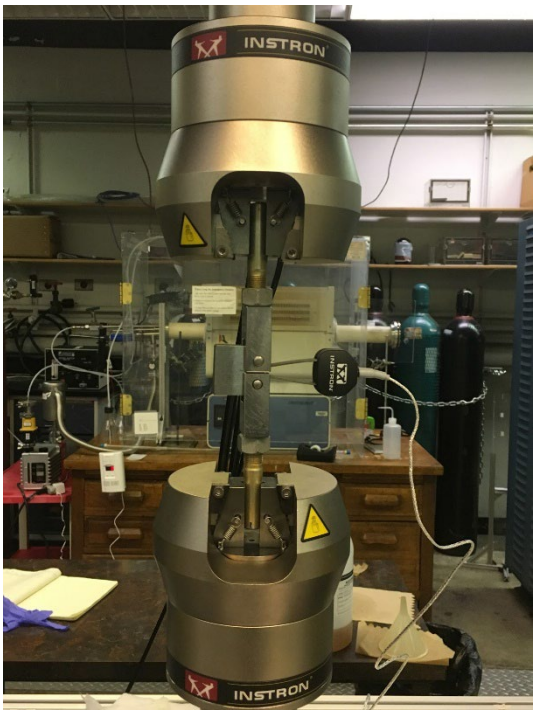

Figure 49. Compact tension fracture toughness test showing COD clip gauge

2.6.2 Fracture Toughness Results

Figure 50 shows typical fracture surfaces from sample CT specimens taken from the five rail types. In each of the samples, the lower surface represents the region of the pre-cut notch; in this photo a wire EDM notch was cut for the AHH, HH, and SS specimens, and waterjet notch cut for the CF&I77 and HAY84 specimens. The portion of the "smooth" fracture surface immediately ahead of the notch region represents the extent of the fatigue precrack as seen from the side view in Figure 47. As part of the ASTM K_{Ic} measurement standards, it is required that the fatigue crack front obtained during precracking be straight within specified limits. In Figure 50, the final, rough portion of the fracture surface beyond the precrack represents the zone of rapid crack advance, which occurs during the K_{Ic} test.

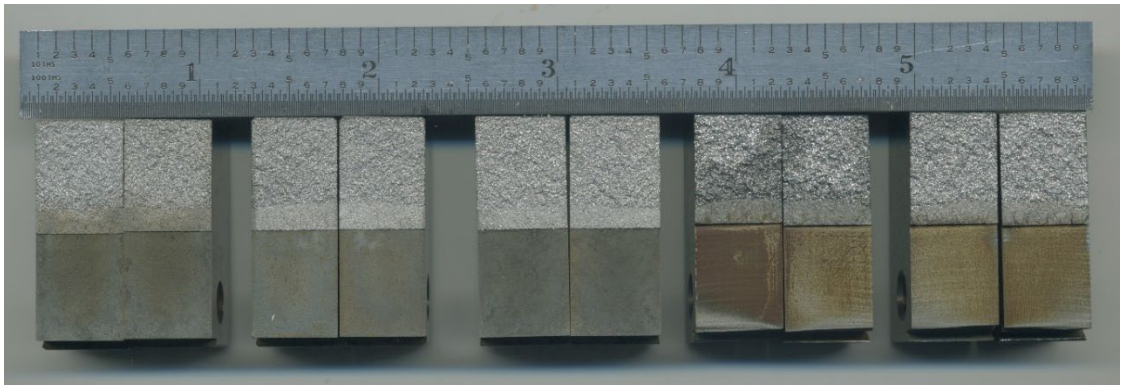

Figure 50. Fracture surfaces after fracture toughness testing, from left to right: AHH, HH, SS, CF&I77, and HAY84

Results from the fracture toughness measurements are given in Figures 51–54. In these figures, the fracture toughness values, K_{Ic}, are given in $\mathrm{MPa}\sqrt{\mathrm{m}}$ at designated locations in the railhead. The small squares indicate the location where specimens were cut from the rail. Red shading indicates K_{Ic} tests and blue indicates fatigue specimens. The gray squares represent specimens that were cut as backup for future testing, or specimens that that were tested but did not fully comply with ASTM requirements for a valid K_{Ic} measurement (see further explanation in Appendix C). The CT specimens were taken from the plate centers (measured from the railhead running surface). These measurements are: 6.5 mm for Slice 1, 19.5 mm for Slice 2, and 32 mm for Slice 3. The fracture toughness for Slice 1 (from the AHH rail) was $K_{Ic} = 40\,\mathrm{MPa}\sqrt{\mathrm{m}}$. For Slice 2, K_{IC} was determined to be slightly less, between $K_{Ic} = 34\,\mathrm{MPa}\sqrt{\mathrm{m}}$ and $K_{Ic} = 36\,\mathrm{MPa}\sqrt{\mathrm{m}}$. For Slice 3, the measured K_{IC} in the rail was $K_{Ic} = 38.8\,\mathrm{MPa}\sqrt{\mathrm{m}}$. As can be seen in Figure 51, the maximum value of K_{IC} is close to the railhead running surface. However, the vertical variation in fracture toughness seems to be relatively small. Likewise, there does not appear to be any significant variation in the fracture toughness across the width of the railhead, as shown in the second slice in Figure 51.

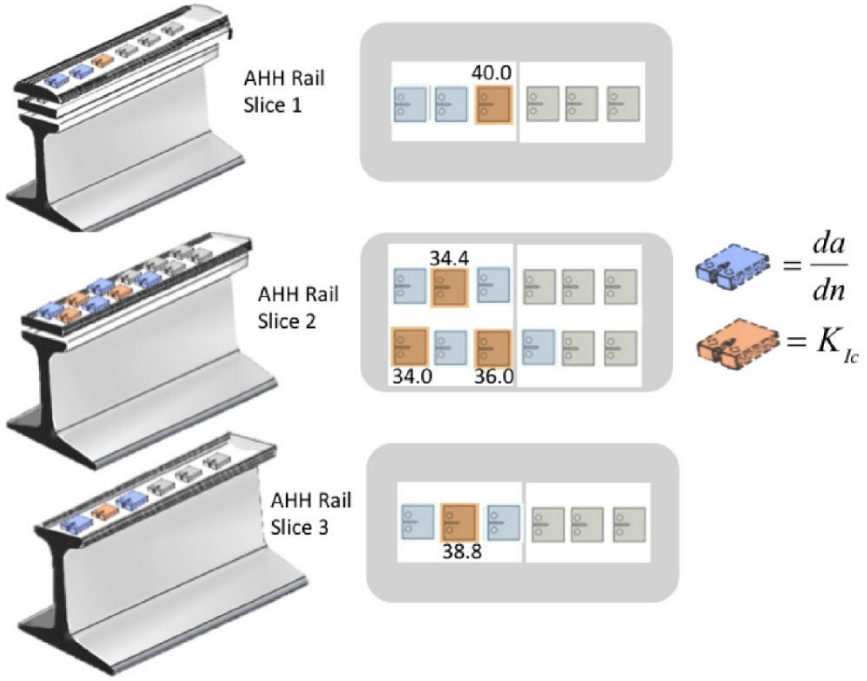

Figure 51. This schematic shows the locations of CT specimens cut from three different levels in AHH railhead. Fracture toughness values are given in terms of $\mathrm{MPa}\sqrt{\mathrm{m}}$. Red designates K_{Ic} test specimens and blue designates fatigue crack growth specimens.

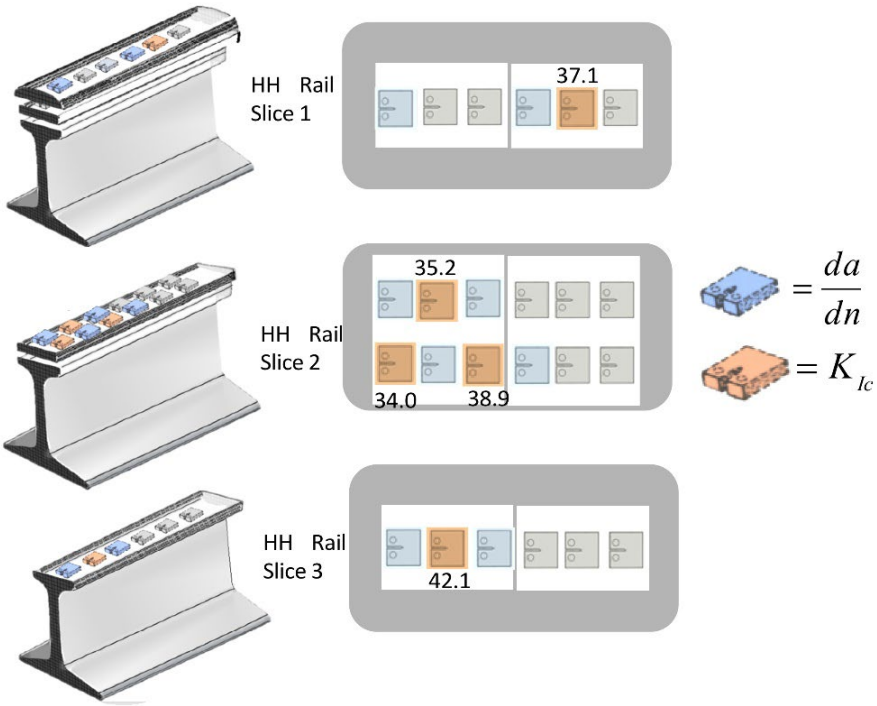

Figure 52. This schematic shows the locations of CT specimens from three different levels in HH railhead. Fracture toughness values are given in terms of $\mathrm{MPa}\sqrt{\mathrm{m}}$. Red designates K_{Ic} test specimens and blue designates fatigue crack growth specimens.

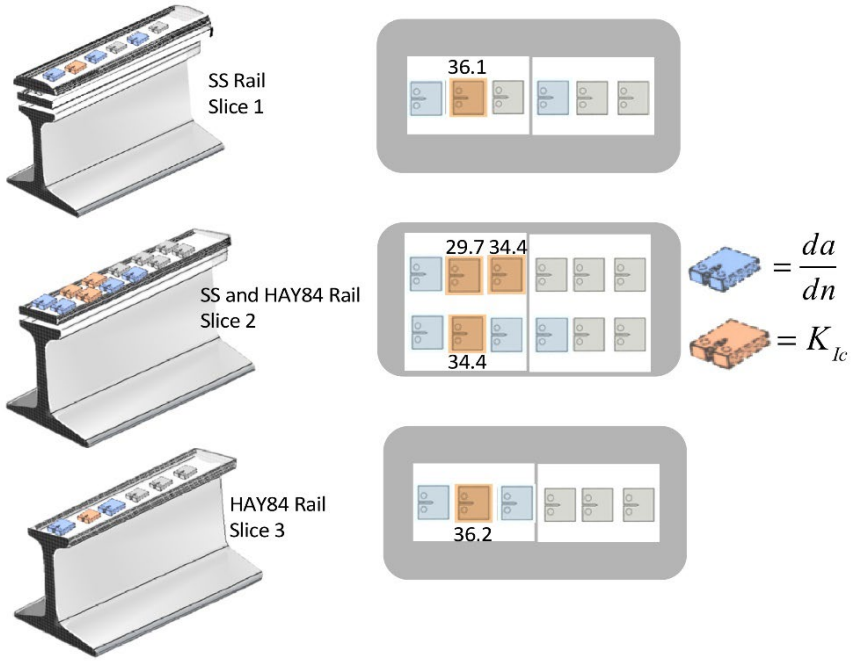

Figure 53. This schematic shows the locations of CT specimens cut from three different levels in SS and HAY84 railheads. Fracture toughness values are given in terms of

$\mathrm{MPa}\sqrt{\mathrm{m}}$. Red designates K_{Ic} test specimens and blue designates fatigue crack growth specimens.

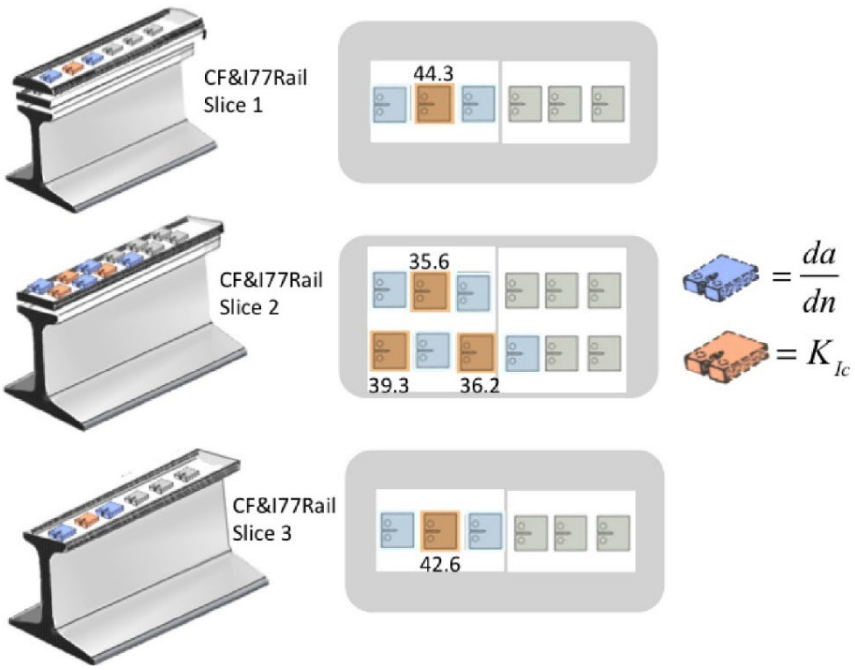

Figure 54. This schematic shows the locations of CT specimens cut from three different levels in CF&I77 railhead. Fracture toughness values given in terms of $\mathrm{MPa}\sqrt{\mathrm{m}}$. Red designates K_{Ic} test specimens and blue designates fatigue crack growth specimens.

If thinner layers within the railheads were analyzed, greater vertical variation in the fracture toughness may be revealed. However, to achieve a finer fracture toughness spatial resolution would require much thinner specimens, specimens that would violate the ASTM small scale yielding requirement. If such measurements were desired, it would be more appropriate to use J_{Ic} testing procedures.

Small variations in fracture toughness values were noted among the railheads, as shown in Figures 51–54. In the early phase of the testing program, the researchers recognized that the SS and HAY84 rails would have very similar fracture toughness values. Thus, the fracture toughness results from these two rails are combined in Figure 53.

Considering the fracture toughness measurements obtained from the horizontally-cut plates in the railheads, average fracture toughnesses for the different rails are: AHH = 36.6 $\mathrm{MPa}\sqrt{\mathrm{m}}$, HH = 37.5 $\mathrm{MPa}\sqrt{\mathrm{m}}$, SS & HAY84 = 34.2 $\mathrm{MPa}\sqrt{\mathrm{m}}$, and CF&I77 = 39.6 $\mathrm{MPa}\sqrt{\mathrm{m}}$. These values constitute a negligible difference in the average fracture toughness for the different rails. Table 8 summarizes the variation in the average fracture toughness in each rail type as a function of depth (measured from the railhead running surface) to the center of the test specimen.

Table 8. Fracture Toughness K_{Ic} ($\mathrm{MPa}\sqrt{\mathrm{m}}$) as a function of depth measured from the railhead running surface

Depth in mm	AHH	HH	SS & HAY84	CF&I77
6.5	40.0	37.1	36.1	44.3
19.5	34.7	36.0	32.8	37.0
32.0	38.8	42.1	36.2	42.6

2.7 Fatigue Testing

Most of the fatigue measurements used the same type of CT specimens as the fracture toughness testing (Figure 43). The specimens were precracked (as shown in Figure 47) at constant $\Delta K = 16\ \text{MPa}\sqrt{\text{m}}$. Continuous fatigue crack growth measurements were taken on CT specimens subjected to varying amplitude sinusoidal loading at a frequency of 20 Hz. The fatigue crack growth rate (da/dn) for each specimen was monitored as a function of the change in the stress intensity factor (ΔK), where $\Delta K = K_{max} - K_{min}$. In most tests, the magnitude of the R-ratio $\left(R = K_{\text{min}}/K_{\text{max}}\right)$ was maintained at $R = 0.1$. As noted in Section 2.6, the research team anticipated that the relatively small dimensions of the CT specimen would minimize any residual stress effect on the fatigue crack growth rate measurements. Thus, they expected that the da/dn measurements from the CT specimens are primarily a function of the local metallurgical properties and orientation. During measurement of the crack growth rates, the measured value of the load amplitude P and the clip gauge measurement of the crack opening displacement (COD), or δ_1, provides sufficient information for computing the crack length a and the instantaneous value of K_1, based on the compliance formula for the CT specimen (see Appendix C). Using feedback control, crack growth rate tests were conducted under controlled ΔK conditions, i.e., under decreasing or increasing ΔK.

2.7.1 Fatigue Crack Growth Rate Results

Fatigue crack growth rate measurements were performed on CT specimens cut from two different orientations in the railheads. The first orientation relied on CT specimens cut from horizontal plates taken at three different levels within the railhead as depicted in Figures 55–58; this was the orientation used for most of the fatigue testing. These locations were the same as the locations of the fracture toughness measurements described in Section 2.6. The crack propagation direction for these specimens was therefore along the major axis of the rail, a direction with very uniform material properties. The second orientation used CT specimens cut from vertical plates taken from either side of the plane of symmetry in the railhead as shown in Figure 59. The CT specimens from vertical plates allowed the team to measure fatigue crack growth behavior in two different crack propagation directions. As shown in Figure 59, cracks from the vertically oriented CT specimens were designed to measure crack propagation behavior either vertically downwards (away from the rail running surface) or vertically upwards (towards the rail running surface).

During the fatigue crack growth rate measurements, load and COD were continuously measured to determine the change in the crack length (Δa) over a specified number of cycles (Δn), as a function of ΔK. In most of the fatigue crack growth rate tests, the fatigue measurements were started at a moderate ΔK value, e.g., 16 $\text{MPa}\sqrt{\text{m}}$. As the crack grew under fatigue conditions,

ΔK was decreased, resulting in decreasing crack growth rates. Though no attempt was made to precisely ascertain values for ΔK threshold (ΔK_T), it is apparent from the da/dn data plots that as the crack growth rate approaches ~ 2×10^{-6}mm/cyc, ΔK_T must be close to ~8 $\mathrm{MPa}\sqrt{\mathrm{m}}$ for the tests conducted with an R-ratio, R=0.1. Once crack growth rates were established at low values of ΔK, the value of ΔK was slowly increased during fatigue testing until the specimen failed. As expected, at high ΔK values the crack growth rates increased (>2×10^{-3}mm/cyc), as K_{max} approached K_{Ic}.

Figure 55 shows the locations for the horizontal CT specimens taken from the AHH railhead. For example, specimen AHH-1B is the designation given to a fatigue specimen cut from the first plate, as measured from the railhead running surface. The center planes of the horizontal specimens are at 6.5 mm (level 1), 19.5 mm (level 2), and 32.0 mm (level 3).

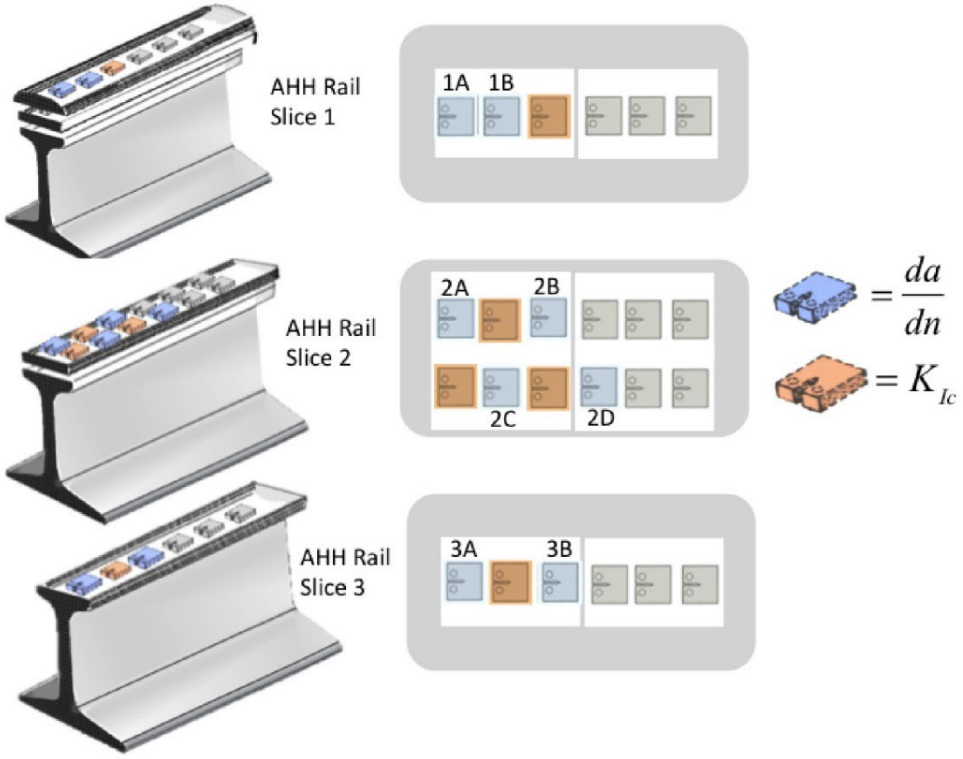

Figure 55. Designations for fatigue specimens taken from different levels in AHH rail

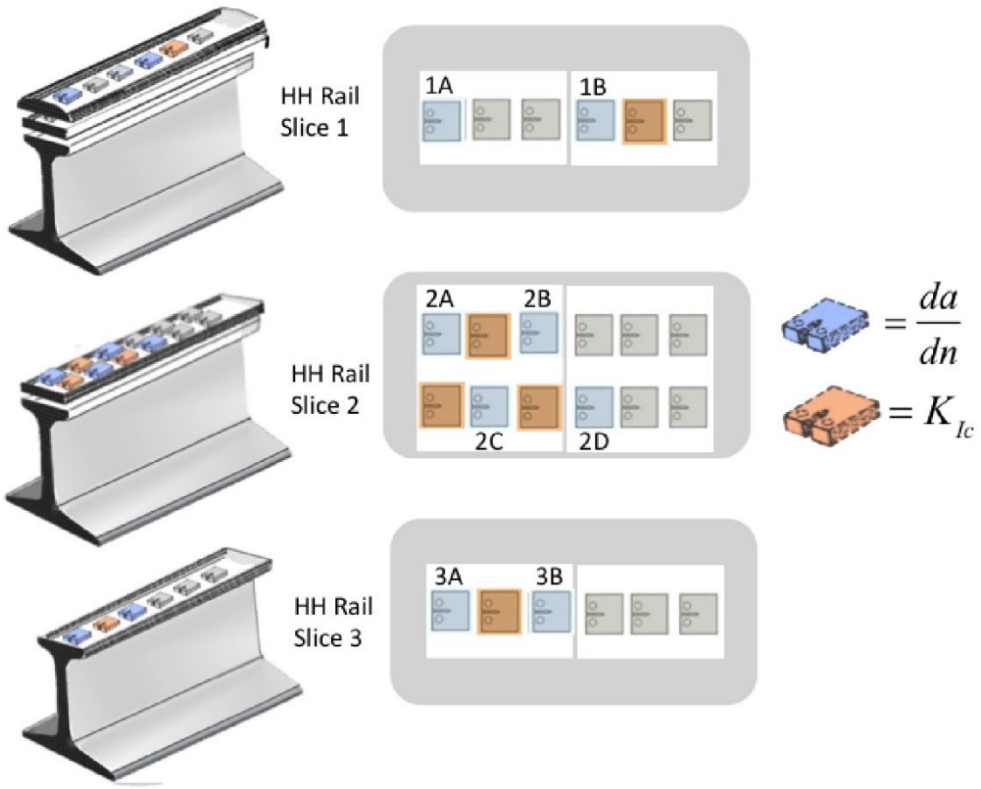

Figure 56. Designations for fatigue specimens taken from different levels in HH rail

Figure 57. Designations for fatigue specimens taken from different levels in SS and HAY84 rails

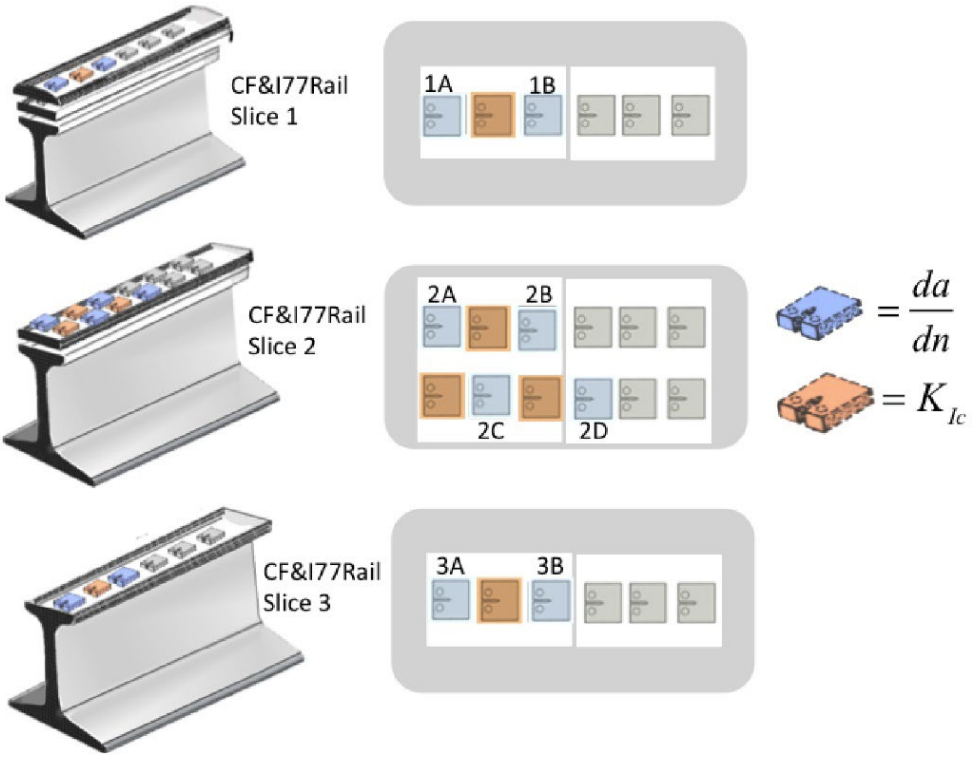

Figure 58. Designations for fatigue specimens taken from different levels in CF&I77 rail

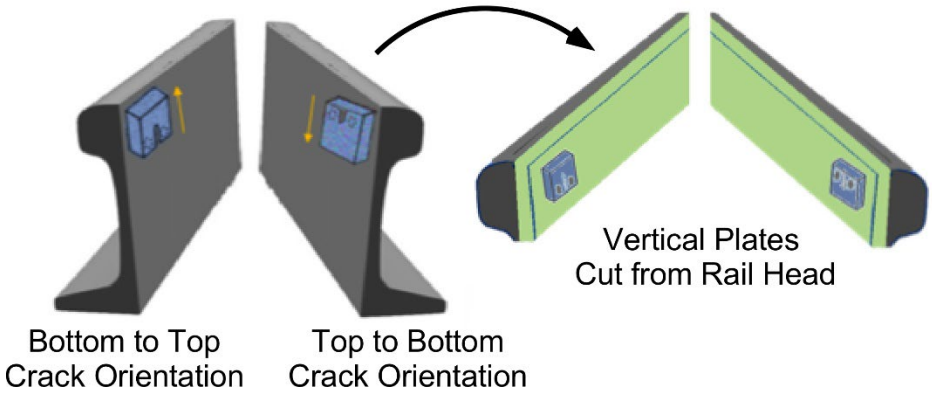

Figure 59. This schematic shows the orientation of CT specimens cut from vertical plates in railhead.

Figure 60 shows a typical plot from one of the crack growth rate fatigue tests. In this figure, a semi-log plot of the crack growth rate data (da/dn) is given as a function of ΔK, for specimen AHH-1B (see Figure 55). This test was conducted at an R-ratio of $R = 0.1$, $\left(R = K_{\min}/K_{\max}\right)$. In the plot, ΔK_T appears to be ~8 $\mathrm{MPa}\sqrt{\mathrm{m}}$. Very high crack growth rates, on the order of 2×10^{-3} mm/cyc, are recorded as ΔK approaches ~29 $\mathrm{MPa}\sqrt{\mathrm{m}}$. In this plot, three different nonlinear least-square curve fits were fit to the data:

Paris-Erdogan fit:
$$\frac{da}{dn} = C\left(\Delta K\right)^p \quad , \tag{0.0.4}$$

with, $C = 3.72\times10^{-10}$, $p = 4.18$.

Forman-Standard fit:
$$\frac{da}{dn} = C\frac{\left(\Delta K\right)^p}{K_c - \Delta K} \quad , \tag{0.0.5}$$

with, $C = 3.69\times10^{-7}$, $p = 2.52$, $K_c = 29.4$.

NASA NASGRO fit:
$$\frac{da}{dn} = C\left(\Delta K\right)^p \frac{\left(1-\frac{\Delta K_{th}}{\Delta K}\right)^m}{\left(1-\frac{\Delta K}{K_c}\right)^q} \quad , \tag{0.0.6}$$

with, $C = 1.37\times10^{-8}$, $p = 2.74$, $m = 0.278$, $q = 0.568$, $\Delta K_{th} = 8.5$, and $K_c = 29.5$.

As shown in Figure 60, the Forman-Standard curve fit provides a good representation of the crack growth rates at high ΔK, and the NASA-NASGRO fit provides a reasonable fit close to ΔK_T. Since the experimental effort in this study was focused on generating data in Region II, the broad midrange of crack growth rates where “power law” dependence prevails, the Paris-Erdogan crack growth rate fit was used to correlate the bulk of the fatigue data for this report.

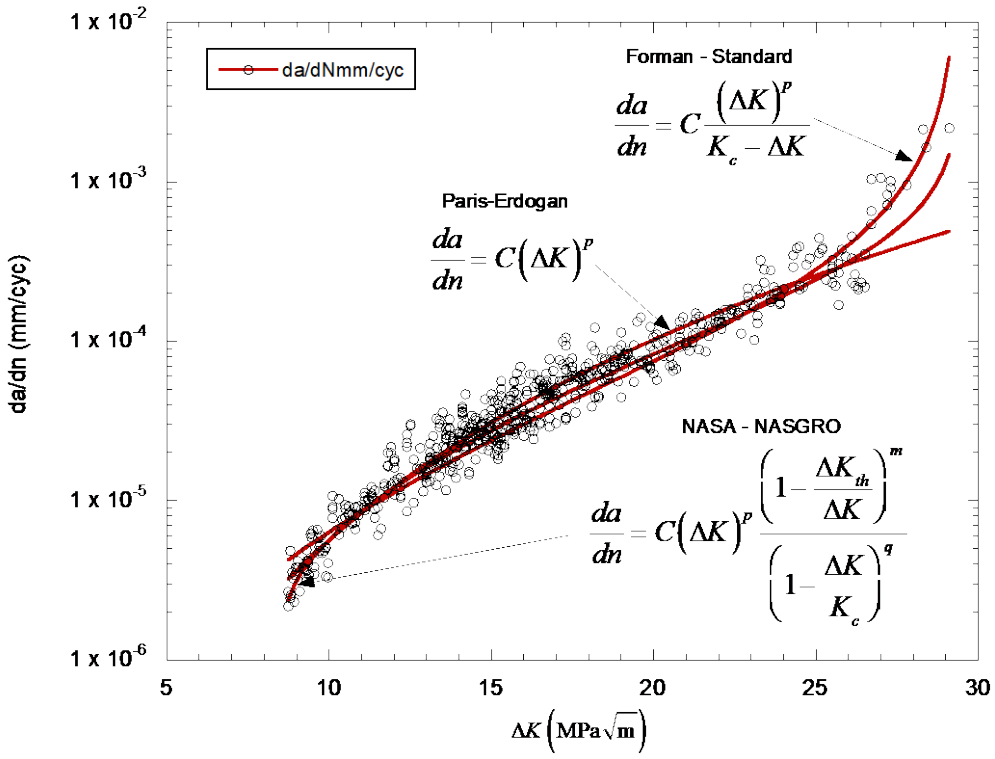

Figure 60. Crack growth rate data from horizontal AHH rail specimen AHH-1B (R=0.1). Curve fit parameters *C*, *p*, *m* and *q* are given in (0.0.4) - (0.0.6).

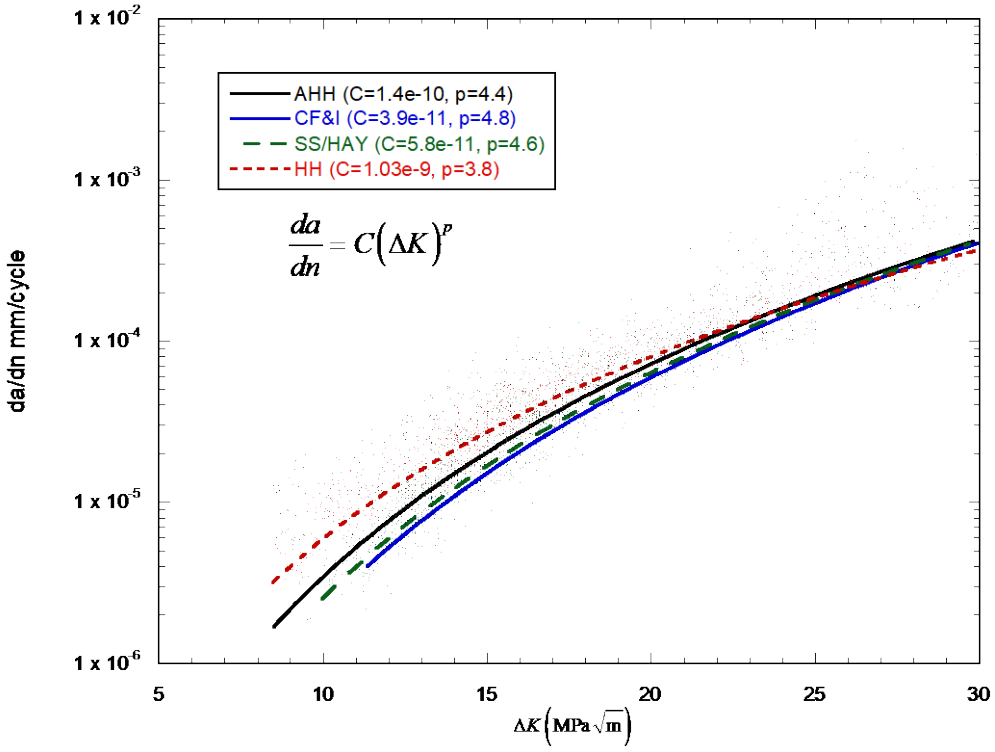

Figure 61. Average fatigue crack growth rates for horizontal cracking in all rails (*R*=0.1). All curve fits based on data from seven test specimens per rail type.

Figure 61 contains a plot of the fatigue crack growth rate data obtained from the horizontal plates shown in Figure 55–Figure 58, cut from the different rail types and tested at the same R-ratio (R=0.1). Test results from seven CT specimens were used to obtain the curve fits for each of the rail types shown in Figure 61. This plot shows the relative similarities in the fatigue crack growth rates in all the rails for the horizontally oriented CT specimens. The main difference in fatigue crack growth rates for the different rails seems to occur at low ΔK values. However, it should be noted that at low crack growth rates, the relative error associated with determination of Δa also becomes greater, and this may exaggerate the differences between the crack growth rates at small da/dn. Overall, the fatigue crack growth rate behavior as a function of ΔK is very similar for the different rails.

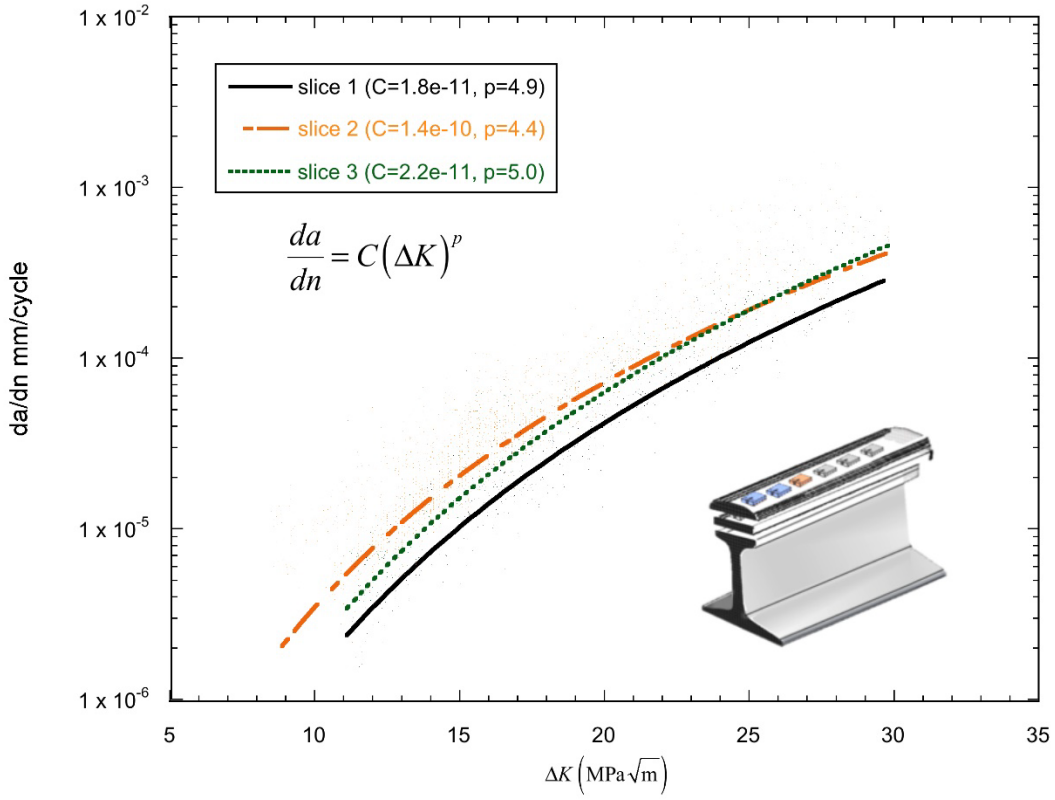

Figure 62. Fatigue crack growth rate in AHH rail at different slice levels. Slice 1 is closest to rail running surface, Slice 3 furthest. *R*=0.1.

Figure 62 shows the variation in the fatigue crack growth rates at different slice levels within the AHH rail. The curve fit for Slice 1 was obtained using data from two CT specimens, Slice 2 from four specimens, and Slice 3 from one CT specimen. Though the differences in crack growth rates at the different depths in the railhead are not great, it does appear that the crack growth rates are lowest in the layer closest to the rail's running surface (~6.5 mm beneath the running surface). In addition to fatigue measurements on horizontally cut layers, fatigue specimens were also fabricated from vertically cut CT specimens (Figure 59). Figure 63 compares the vertical fatigue crack growth behavior in the AHH rail with the horizontal fatigue behavior at various depths in the rail. In Figure 63, the dashed lines represent fatigue cracking measured in the specific horizontal planes depicted in the inset figure, while the solid red line represents the curve fit to

the vertical crack growth behavior. The vertical crack growth rate data lies between the crack growth rates measured from the first and third horizontal slice test specimens.

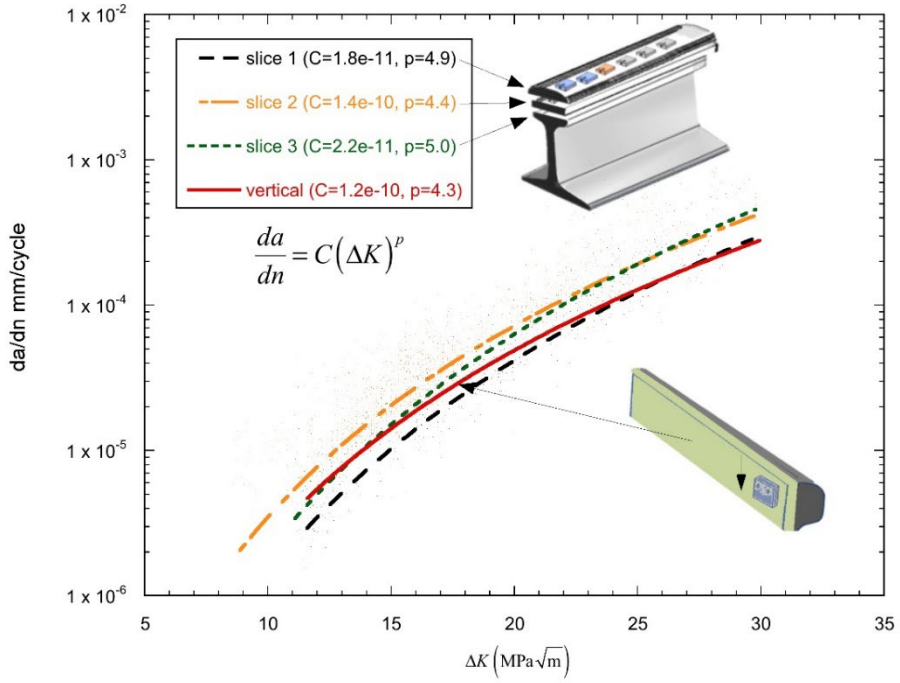

Figure 63. Comparison of average fatigue crack growth rates for horizontal and vertical cracking in AHH rail. *R*=0.1

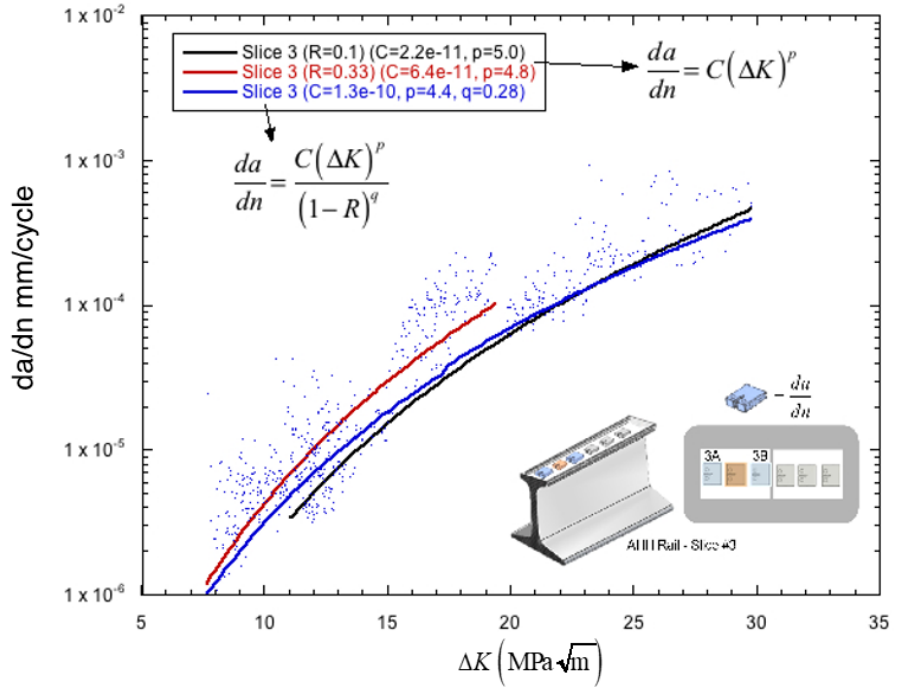

Figure 64. Comparison of horizontal fatigue crack growth rates at two different R-ratios, *R*=0.1 and *R*=0.33, in Slice 3 of AHH rail

Though ΔK is the primary parameter that controls fatigue crack growth rates, the *R*-ratio can exert an important secondary effect on fatigue crack growth. The *R*-ratio, defined as $R = K_{min} / K_{max}$, introduces a mean load on the test specimen in addition to the amplitude of the sinusoidal loading. The *R*-ratio effect can be particularly important for rails subjected to high residual stresses and thus is an important factor that should be quantified for accurate predictions of fatigue reliability in head hardened rails.

Figure 64 provides a comparison of crack growth rates at two different *R*-ratios, R = 0.1 (black line) and R = 0.33 (red line). The crack growth rates depicted in this figure are for specimens AHH-3A and AHH-3B, taken from Slice 3 in the AHH rail (see Figure 55). These two fatigue specimens were located on either side of the AHH fracture toughness specimen that had $K_{Ic} = 38.8\ \text{MPa}\sqrt{\text{m}}$ (Figure 51). Figure 64 exhibits classical R-ratio fatigue behavior, i.e., at the higher *R*-ratio there is an increased crack growth rate and lower ΔK_T values. Supplementing the Paris-Erdogan curve fit, an additional curve fit parameter, q, can be introduced to incorporate the stress ratio effect. One empirical form that is often used to include the *R*-ratio in the curve fit, is the so-called Walker equation given by

$$\frac{da}{dn} = \frac{C(\Delta K)^p}{(1-R)^q} \,. \tag{0.0.7}$$

When curve fitting *da/dn* data over a broad range of *R*-ratio values, *R* can be treated as an additional independent variable, which allows the characterization of *da/dn* behavior as a function of both ΔK and *R*. As shown in Figure 64, using the data from two sets of *R*-ratio tests, the three parameter least-squares fit results in an interpolated curve between the Paris-Erdogan curve fits obtained at the two different *R*-ratios. In this particular case, $C = 1.3 \times 10^{-10}$, $p = 4.4$, $q = 0.28$, for equation (0.0.7). However, in this study, *da/dn* testing was conducted only at two different *R*-ratios, $R = 0.1$ and $R = 0.33$. Thus, the benefit of considering *R* as a separate independent variable, for the purposes of curve fitting over such a limited range of *R*, is questionable. As shown in this figure, for the two different *R*-ratios, there is an overlap in the measured *da/dn* data only between $11\ \text{MPa}\sqrt{\text{m}} < \Delta K < 20\ \text{MPa}\sqrt{\text{m}}$. Thus, for this Walker curve fit, the *da/dn* data at $R = 0.33$ dominates the curve fit for $\Delta K < 11\ \text{MPa}\sqrt{\text{m}}$, and for $\Delta K > 20\ \text{MPa}\sqrt{\text{m}}$, the $R = 0.1$ data dominates. A much more accurate representation of the fatigue data is to simply give the Paris-Erdogan curve fits for the specific values of *R* as shown by the black and red curves in Figure 64. It should also be noted that for higher *R*-ratios, e.g., $R > 0.5$, K_{max} very quickly approaches critical K_c for small values of ΔK. Thus, the available ΔK range of data for a 3-parameter *da/dn* curve fit can be quite small at high *R*-ratios. This often leads to a situation where fitting the *q* term in the Walker equation (0.0.7) is essentially done by trial and error until a value is found that best consolidates the data along a single straight line on the log-log plot of *da/dn*.

The *R*-ratio results obtained from two adjacent vertical crack specimens is shown in Figure 65. The *da/dn* behavior for the vertical cracking appears to be very similar to the horizontal cracking shown in Figure 64.

Figure 66 provides a comparison of the vertical fatigue crack growth behavior in the HH rail with the horizontal fatigue behavior at various depths in the same rail. The fatigue crack growth rates in the HH rail are very similar to the behavior in the AHH rail (Figure 63). However, for the HH rail, the lowest horizontal crack growth rates were measured in Slice 3, the layer furthest away from the running surface. In the AHH rail, the lowest crack growth rates were measured in Slice 1. The higher crack growth rates in the HH rail for Slice 1 and Slice 2 were almost identical to each other. As was observed in the fatigue crack growth rate behavior for the AHH railhead, the vertical crack growth rates in the HH rail lie between the crack growth rates measured in the first and third horizontal slice test specimens.

The fatigue crack growth rate measurements in the AHH and HH rails appear to be similar. However, there are some subtle structural differences in the nature of the fatigue cracking. This is shown in Figure 67, which contains a side-by-side comparison of the fatigue/fracture surfaces for CT specimens AHH 2A (see Figure 55) and HH 2A (see Figure 56). These two specimens were cut from identical locations in the two different rails and tested under identical fatigue conditions (R=0.1). As can be seen in the photographs, the fatigue surfaces in the AHH rail are noticeably smoother than counterpart fatigue/fracture surfaces in the HH rail. This difference in fatigue fracture surface roughness was also noted in the fatigue tests conducted on the CCT test specimens.

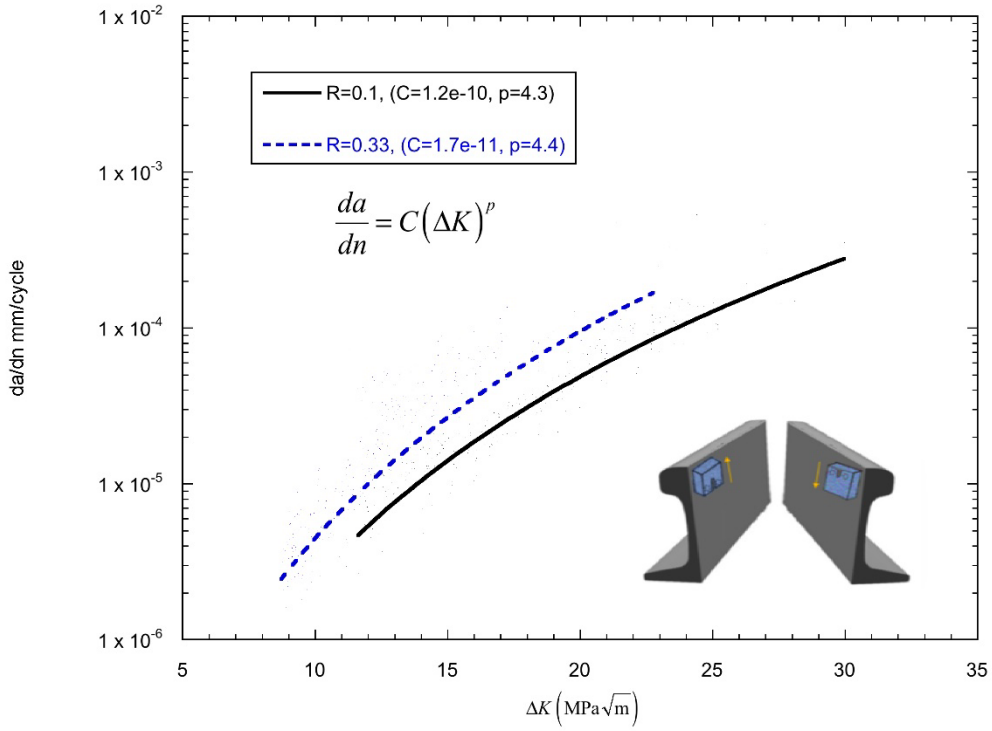

Figure 65. Comparison of vertical fatigue crack growth rates in AHH rail for CT specimens at two different *R*-ratios, *R*=0.1 and *R*=0.33

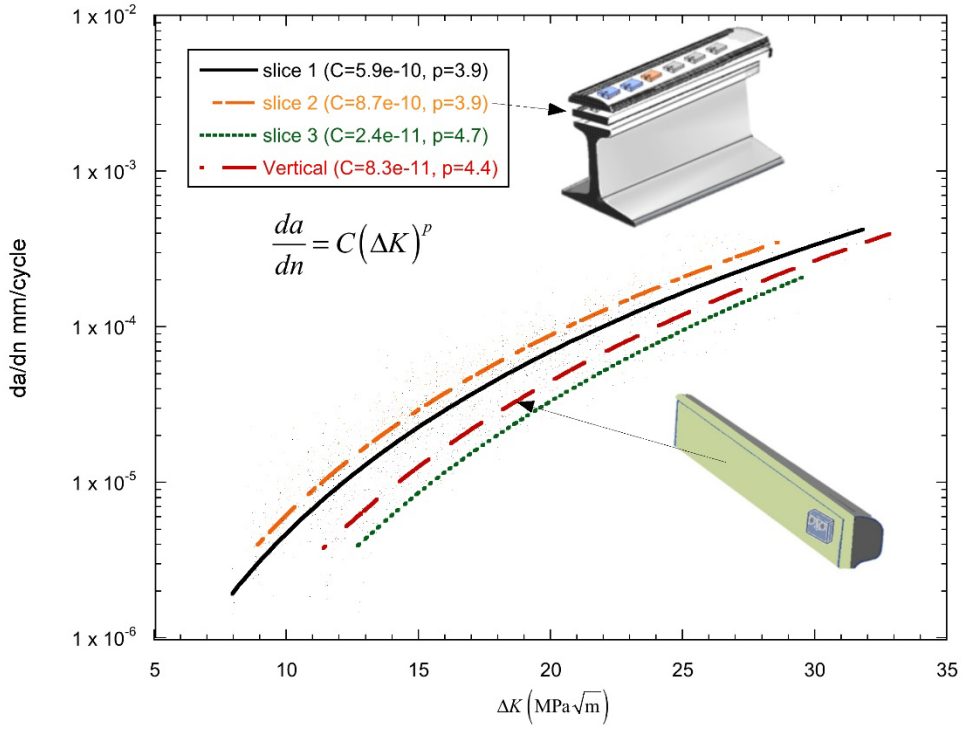

Figure 66. Comparison of fatigue crack growth rates for horizontal and vertical cracking in HH rail. *R*=0.1. Slice 1 (2 tests), slice 2 (4 tests), slice 3 (1 test), vertical (1 test)

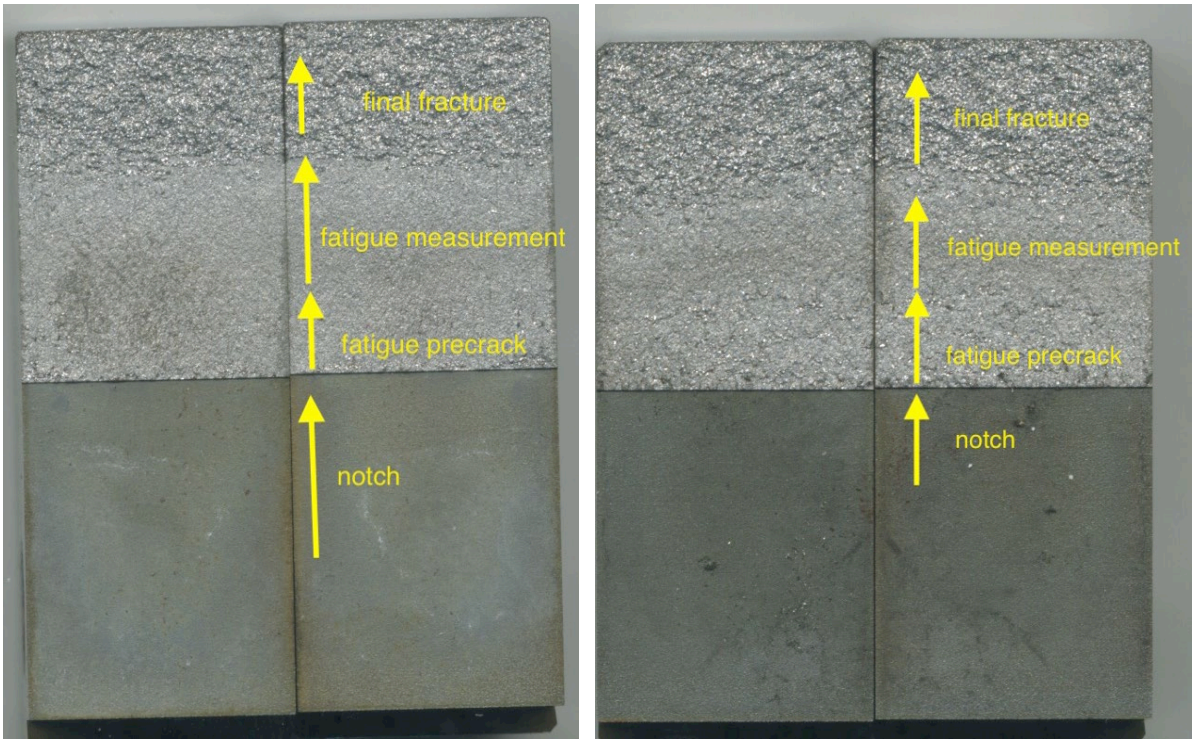

(a) (b)

Figure 67. Fatigue/fracture surfaces: (a) AHH Slice 2 (smooth fatigue crack surface), (b) HH Slice 2 (rougher fatigue crack surface), *R*=0.1

The fatigue curve fits for the HH rail at *R*-ratios 0.1 and 0.33 are given in Figures 68 and 71, for horizontal and vertical cracking, respectively. As observed in the AHH rails, the fatigue cracking at different *R*-ratios in the HH rails represents classical *R*-ratio behavior with increasing *R*, i.e., increased crack growth rates, lower ΔK_T, and a decrease in the maximum value of ΔK before the onset of rapid (Region III) crack growth rates. Figures 69 and 70 contain photographs of the fatigue fracture surfaces for the HH horizontal fatigue test specimens taken from Slice 3, i.e., location HH 3B and HH 3A (Figure 56), respectively. These two CT test specimens have similar, rough fatigue/fracture surfaces. Note that the discoloration on the crack surfaces was due to oxidation, which occurred several weeks after the original testing. Specimen HH 3B was tested at *R*=0.1 and HH 3A at *R*=0.33. Tests at these different *R*-ratios do not appear to have any significant effect on the relatively rough appearance of the fatigue surfaces. Referring to Figure 52, the fracture toughness at this location in the HH rail is also relatively high, measured to be $K_{Ic} = 42.1\ \text{MPa}\sqrt{\text{m}}$.

Figures 72–74 contain the fatigue crack growth results from the SS and HAY84 rails. The plots in Figure 72 are average *da/dn* results from both rails. The results for vertical cracking in Figure 74 are solely from the HAY84 rail. Figures 75–77 contain the fatigue crack growth rate measurements from the CF&I77 rail.

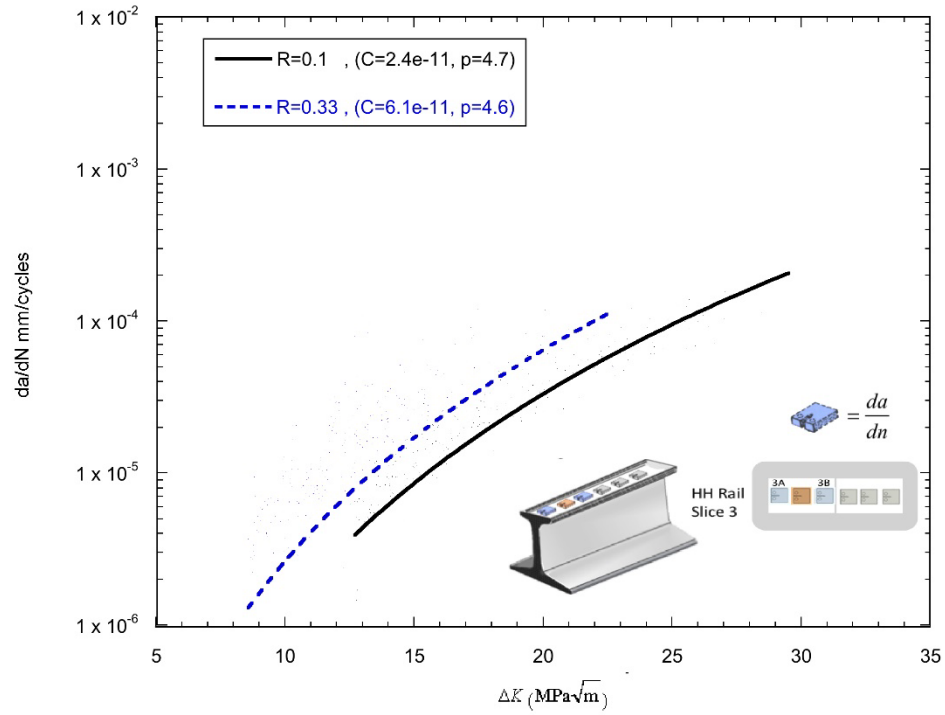

Figure 68. Comparison of horizontal fatigue crack growth rates at two different R-ratios in Slice 3 of HH rail, *R*=0.1 and *R*=0.33

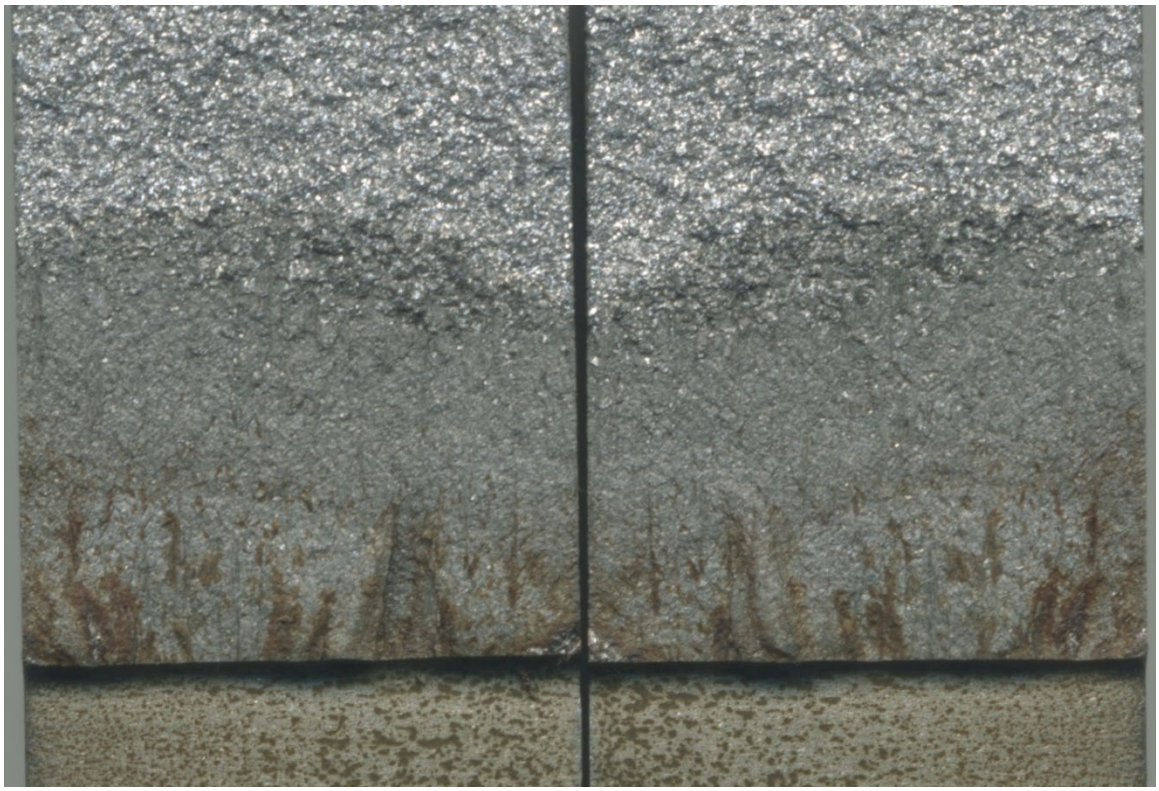

Figure 69. Fatigue/fracture surface for HH 3B tested at *R*=0.1

Figure 70. Fatigue/fracture surface for HH 3A tested at *R*=0.33

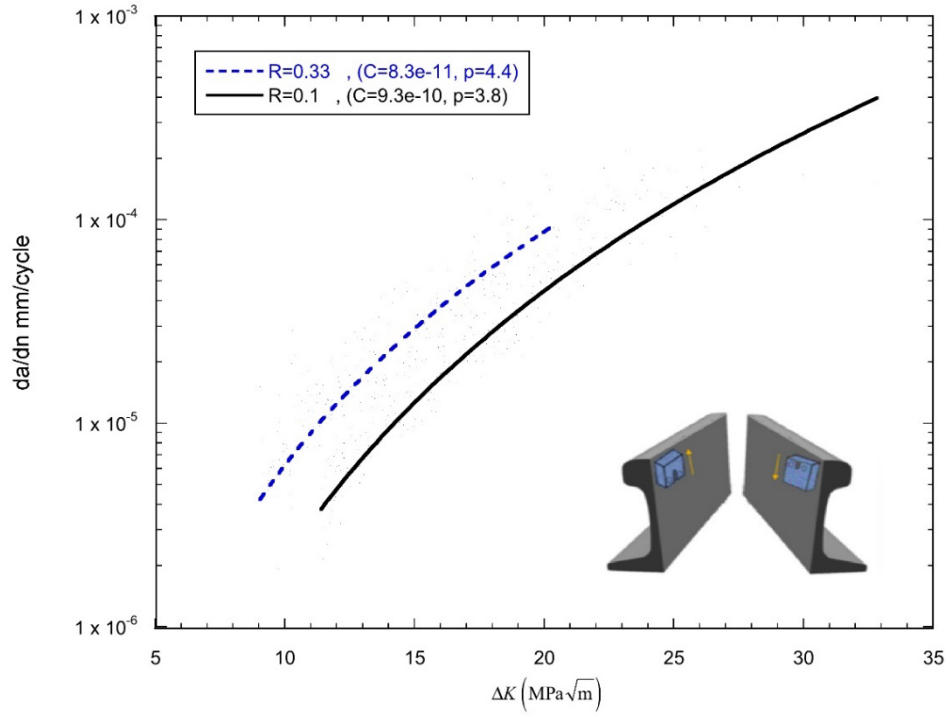

Figure 71. Comparison of vertical fatigue crack growth rates in HH rail for CT specimens at two different R ratios. *R*=0.1 and *R*=0.33

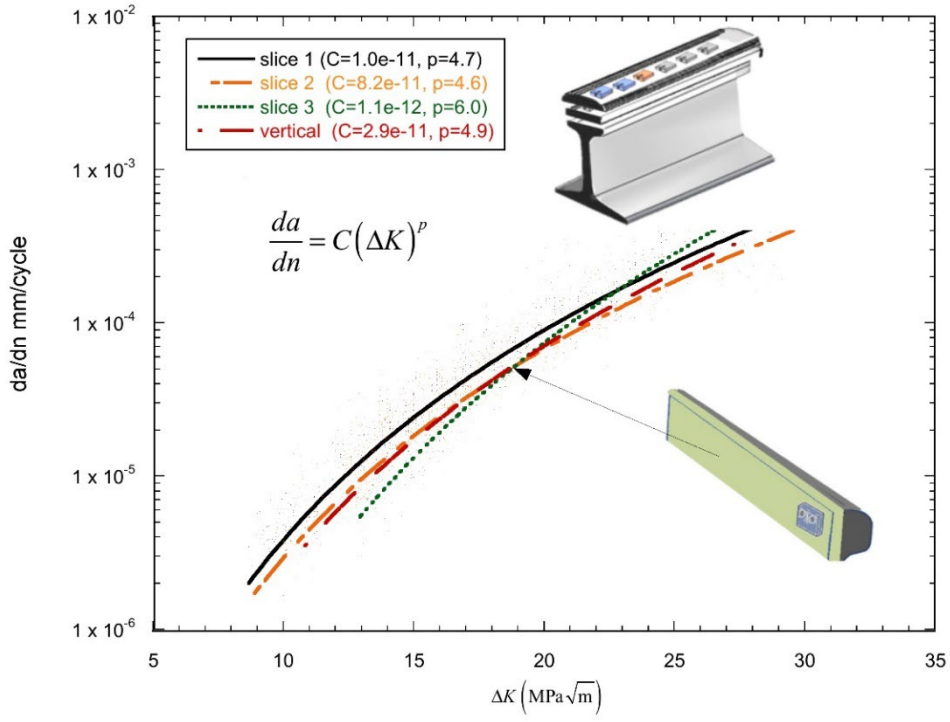

Figure 72. Comparison of fatigue crack growth rates for horizontal and vertical cracking in the SS and HAY84 rails, *R*=0.1

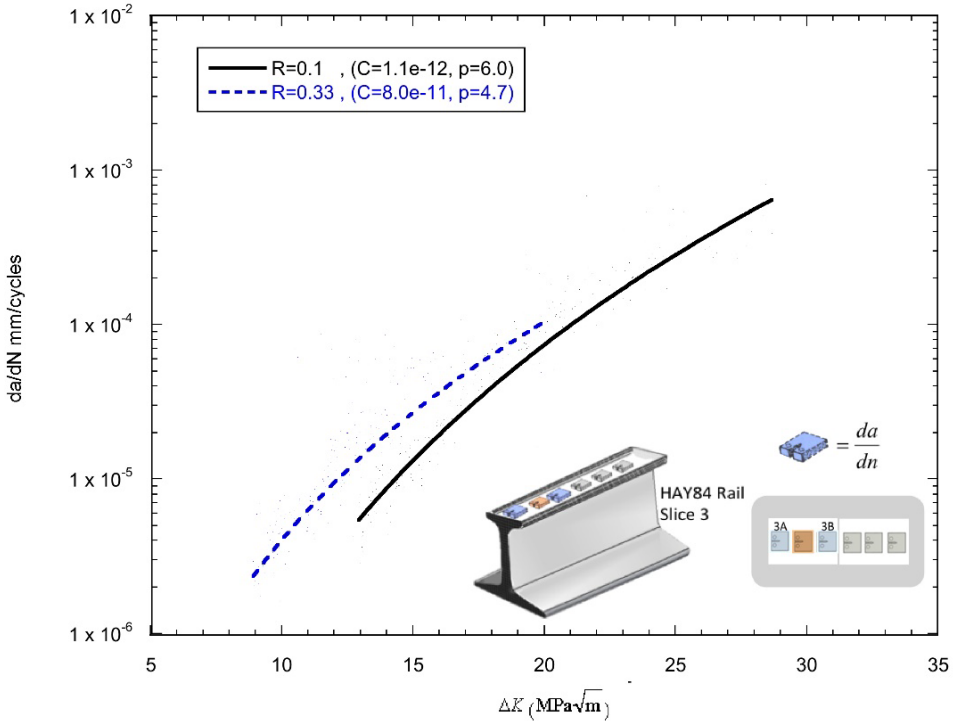

Figure 73. Comparison of horizontal fatigue crack growth rates at two different R-ratios in Slice #3 of HAY84 rail, *R*=0.1 and *R*=0.33

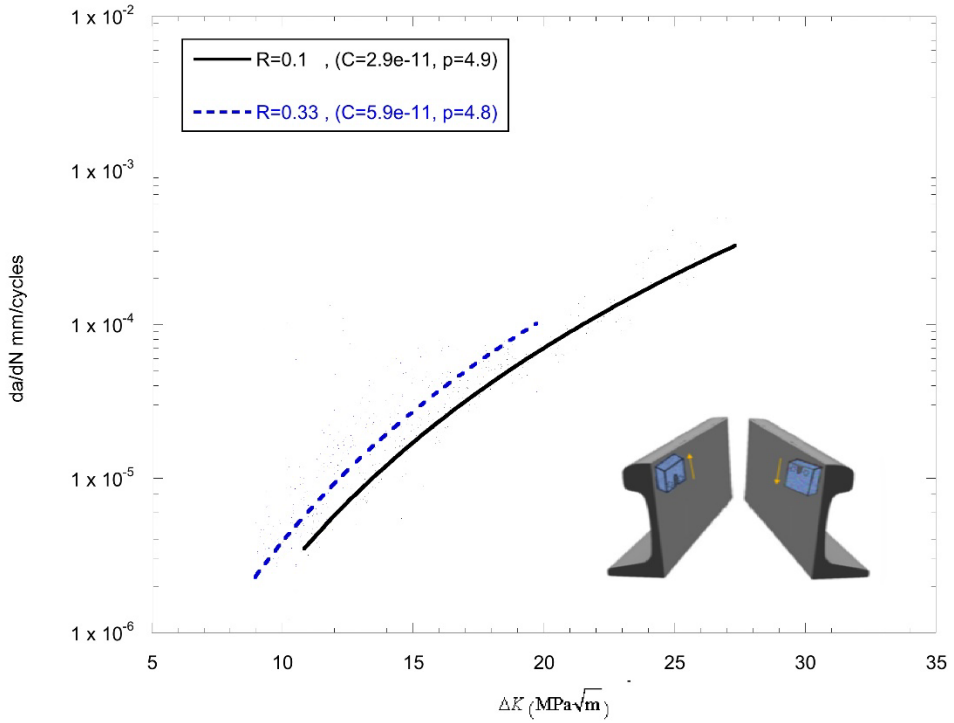

Figure 74. Comparison of vertical fatigue crack growth rates in the HAY84 rail for CT specimens at two different R ratios, *R*=0.1 and *R*=0.33

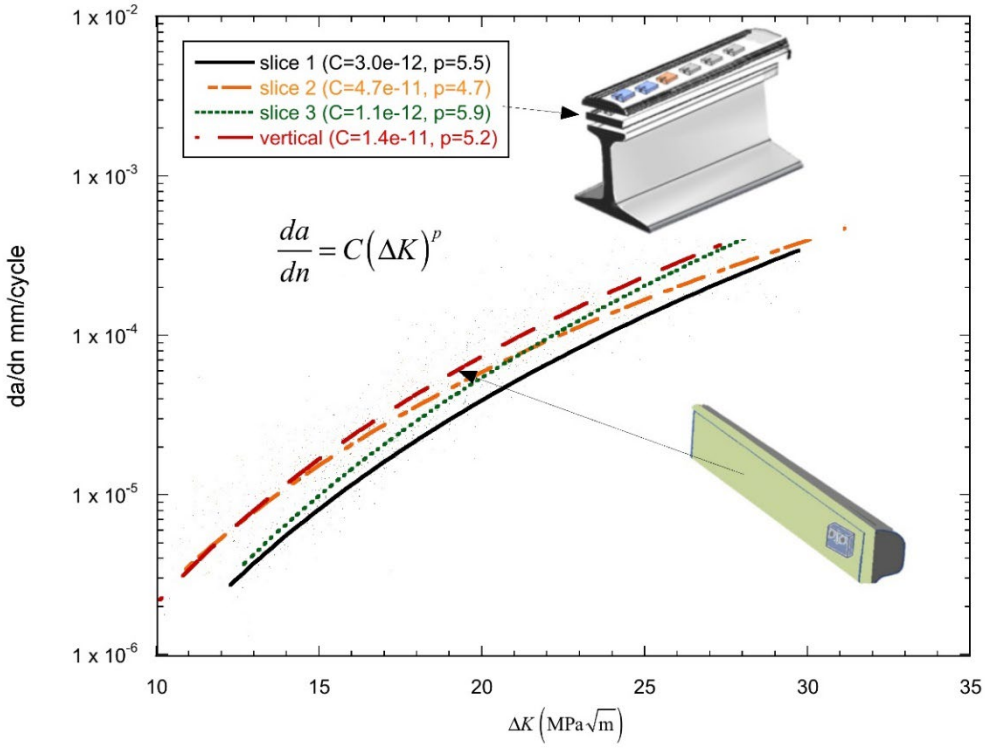

Figure 75. Comparison of fatigue crack growth rates for horizontal and vertical cracking in the CF&I77 rail, *R*=0.1

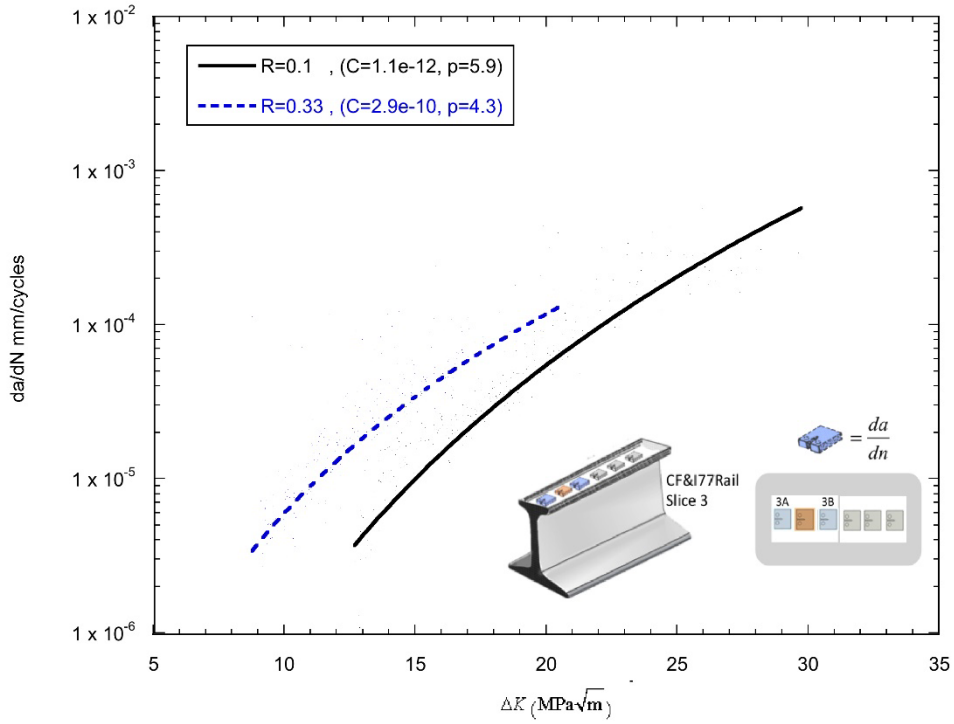

Figure 76. Comparison of horizontal fatigue crack growth rates at two different R-ratios in Slice 3 of CF&I77 rail, *R*=0.1 and *R*=0.33

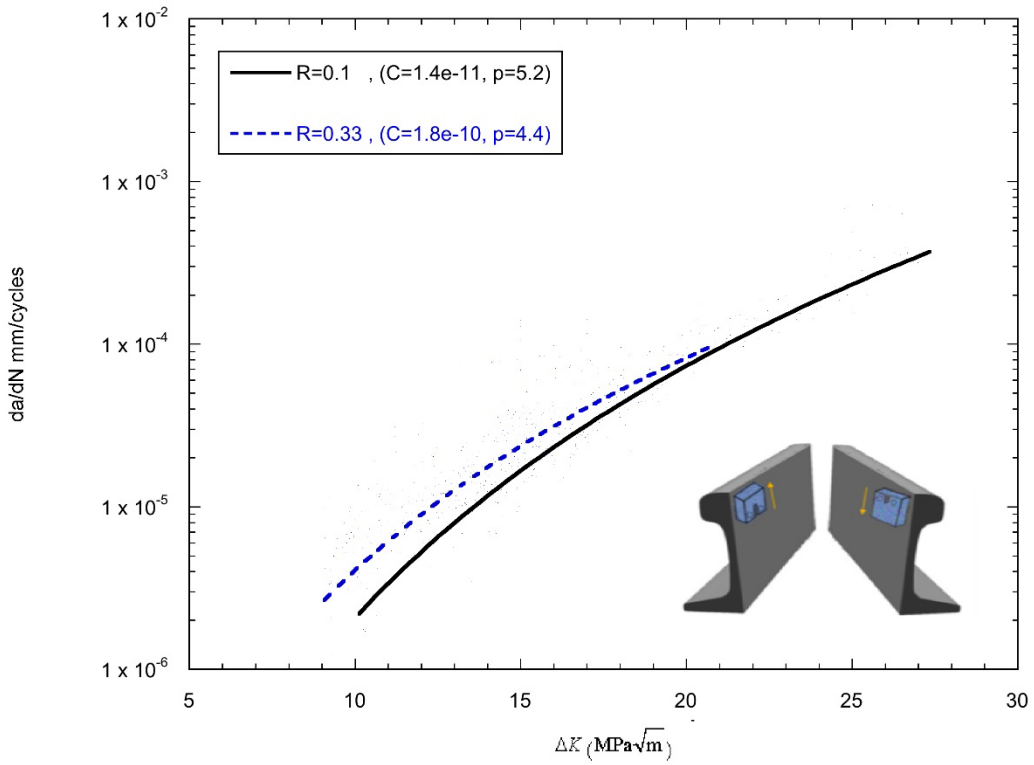

Figure 77. Comparison of vertical fatigue crack growth rates in CF&I77 rail for CT specimens at two different R ratios, *R*=0.1 and *R*=0.33

In addition to the CT test specimens, four large CCT specimens were also used to measure fatigue crack growth rates within the AHH and HH railheads. The CCT specimens were cut from long plates taken from the widest portion of the railheads (Figure 78). As shown in this figure, the CCT specimen widths span the entire width of the railhead. The gray area in Figure 78 indicates the location of the notch/precrack. Figure 79 gives the dimensions of the CCT specimen prepared for the fatigue tests. The CCT specimens had a 0.010-in-width notch cut using wire electrical discharge machining (EDM) prior to precracking, and the specimens were loaded in uniaxial tension via pin loading (Figure 80). The fatigue testing of the CCT specimens was conducted at Laboratory Testing, Inc. (LTI) in Hatfield, PA, under the supervision of Dr. M. Adler.

The main purpose of conducting fatigue tests on the much larger CCT specimens is that, unlike the CT test specimens, there is a high likelihood the CCT specimens will have a significant residual stress component normal to the crack surface. If there is a significant variation in the residual stresses across the width of the railhead, this should be continued over to the CCT plate cross-section, even though the material (and residual stresses) above and below the CCT plates have been removed due to cutting. The tensile residual stress component that exists in the axial direction in the interior of the railhead arises during the railhead hardening process. A sufficiently high tensile residual stress component normal to the crack surface in the CCT specimen will cause an increase in the fatigue crack growth rates compared with the residual stress-free CT specimens.

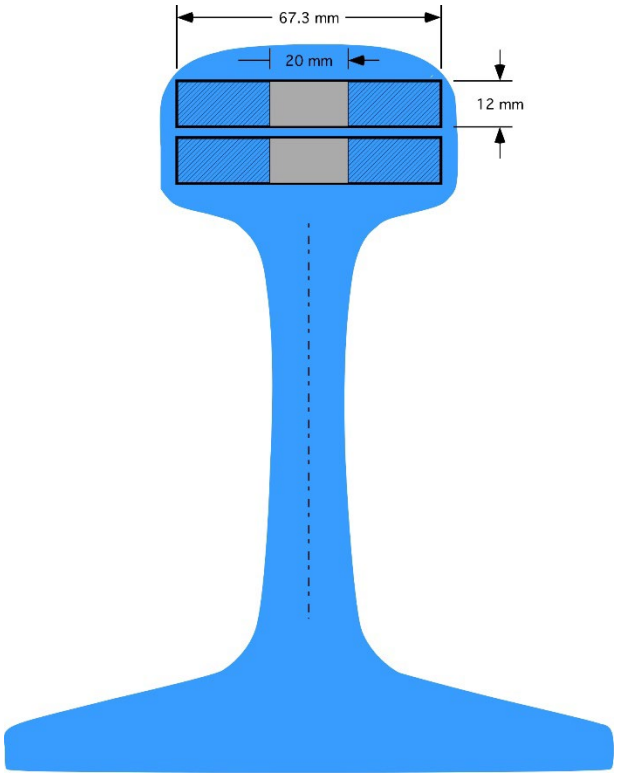

Figure 78. Cross-section view of CCT fracture specimens cut from railheads

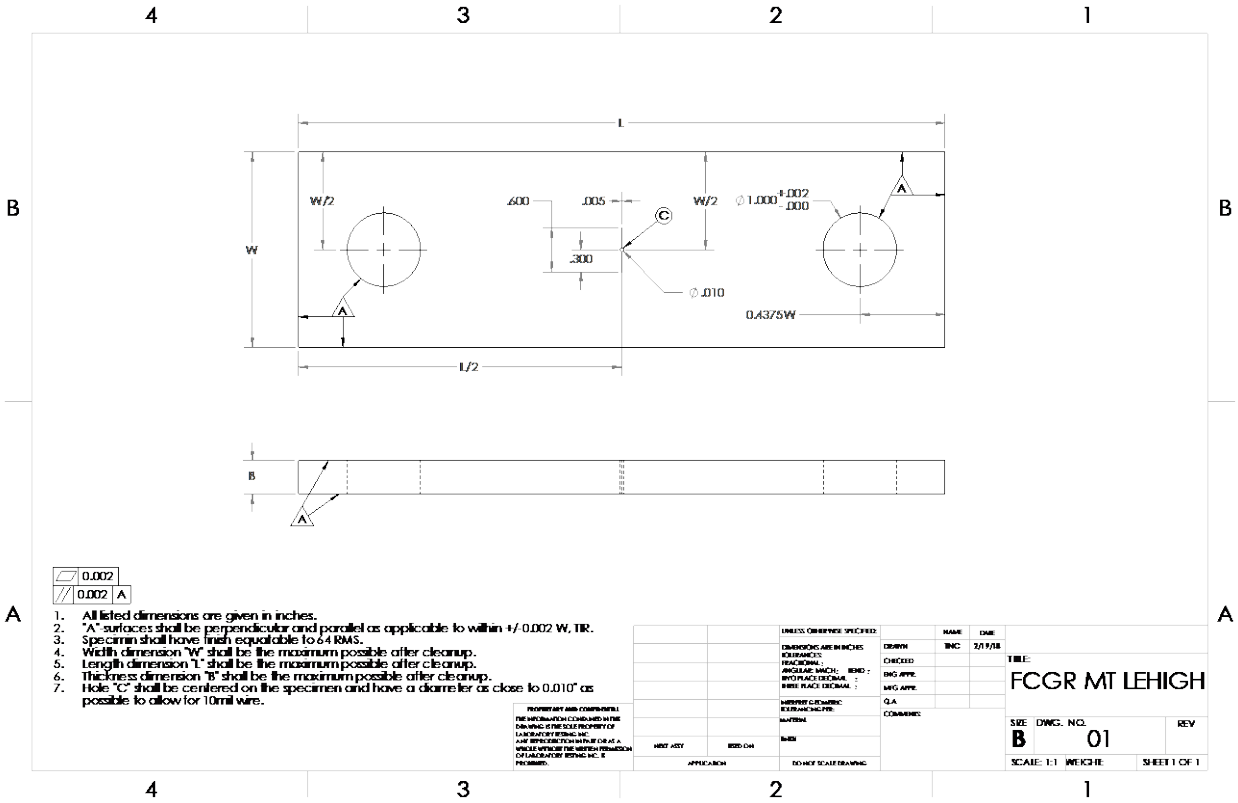

Figure 79. Dimensions used for center cracked test specimen

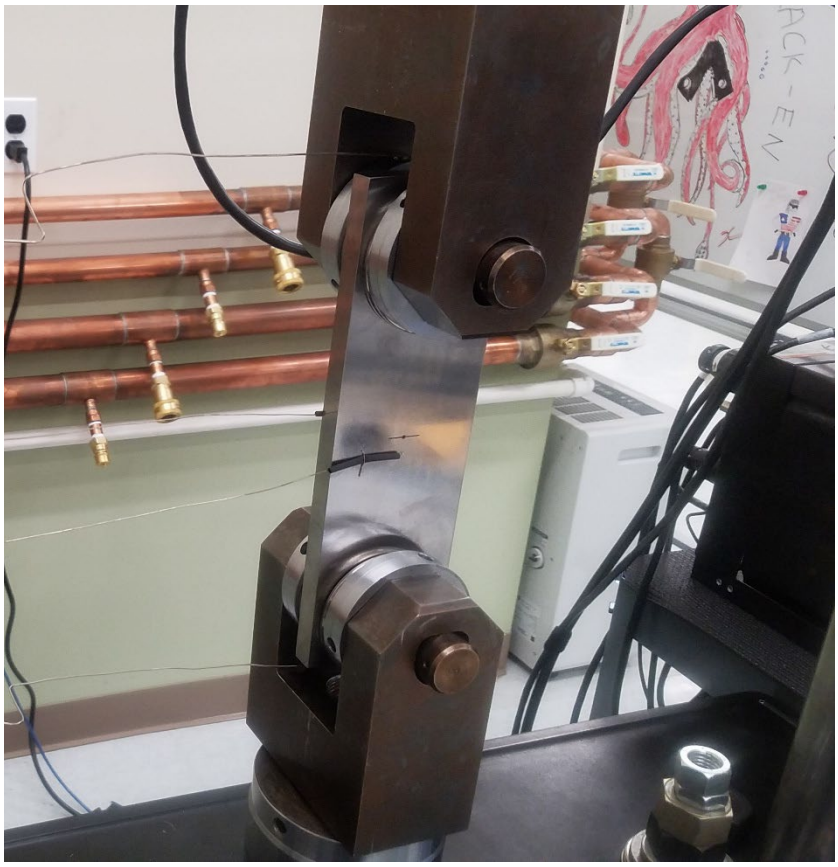

Figure 80. Testing of center cracked tension (CCT) specimen at LTI

The *da/dn* measurements at different *R*-ratios for the CT specimens can be considered to represent a baseline, i.e., residual, stress-free measurements. This cannot necessarily be assumed for the CCT specimens, due to their much larger size, where the specimen width spans the entire cross-sectional width of the hardened head. The apparent differences in crack growth rates from the two different specimen types for the HH rail can be seen in Figure 81. The figure shows that the crack growth rates obtained from the CCT tests were generally higher than the crack growth rates obtained from the CT specimens, tested at an *R*-ratio of *R*=0.1. In addition, the CCT testing seems to enter the Region-III, i.e., high crack growth rate fatigue behavior at ~ ΔK= 26 $\mathrm{MPa}\sqrt{\mathrm{m}}$. This is indicative of a lower fracture toughness than an HH rail specimen with negligible residual stress, e.g., $K_{Ic} > 35$ $\mathrm{MPa}\sqrt{\mathrm{m}}$ (Table 8). A better match with the CCT crack growth rates occurs when compared with the CT crack growth rates performed at *R*=0.33 (Figure 82).

Figure 83 shows the fatigue surface taken from the HH rail CCT specimen. This photograph is taken looking down on the left side of the central crack surface with the wire EDM notch surface to the right and the rough fatigue crack surface on the left. The roughness of the fatigue surface is like the rough fatigue surfaces observed in the CT specimens (Figures 69 and 70).

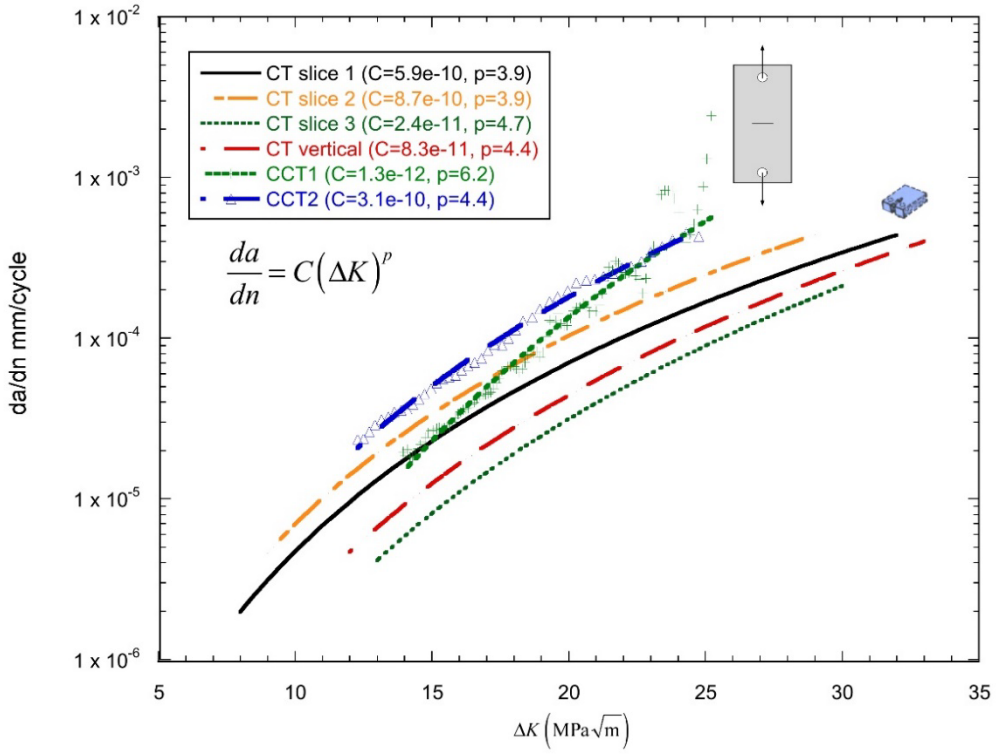

Figure 81. Comparison of fatigue crack growth rates from CT and CCT specimens for HH rail, *R*=0.1.

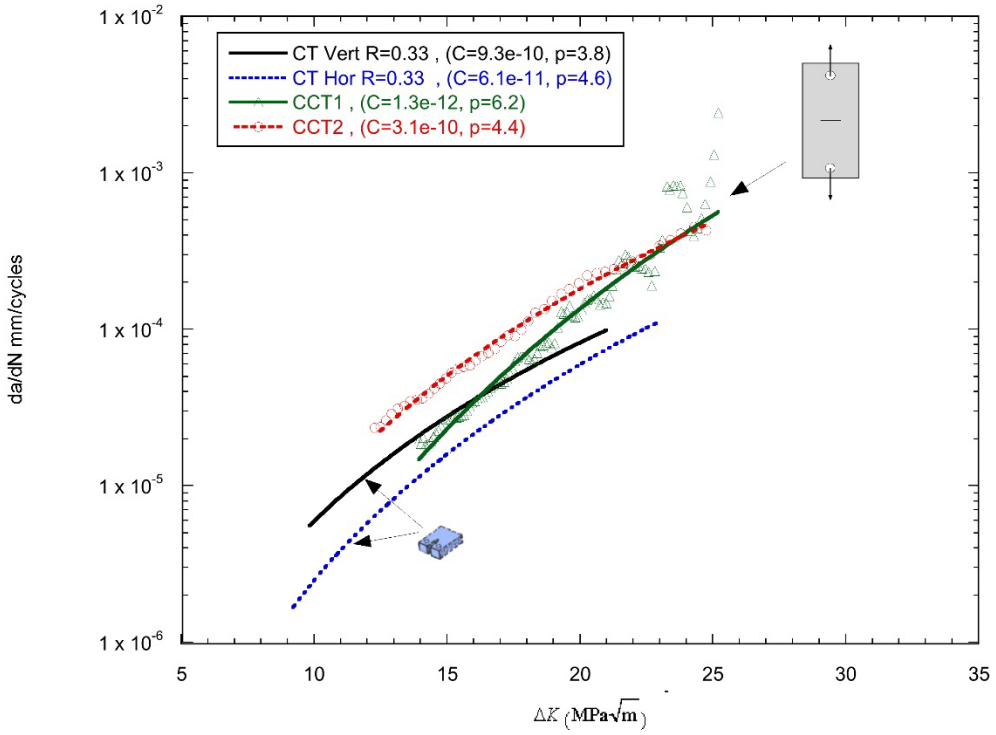

Figure 82. Comparison of fatigue crack growth rates from horizontal and vertical CT specimens (*R*=0.33) with CCT specimens from the HH rail

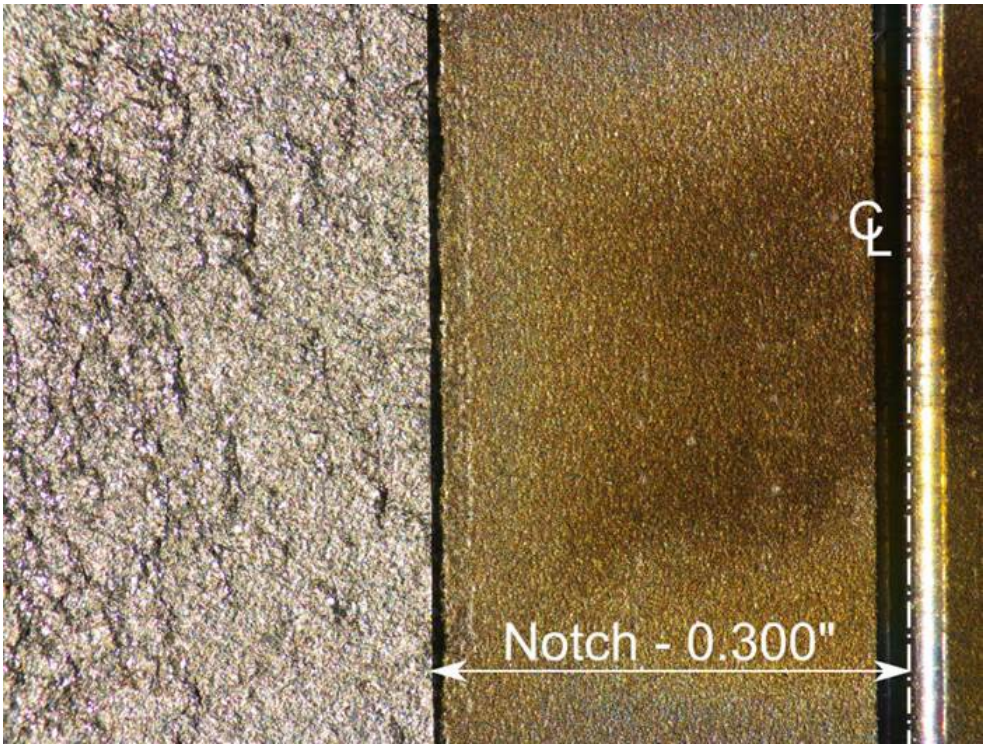

Figure 83. Fatigue/fracture surface taken from HH rail CCT test specimen showing rough fatigue crack surface

Figure 84 compares the crack growth rate from the AHH CCT specimen with the crack growth rates from the AHH CT specimens cut from different layers in the AHH rail. The crack growth rates in the CCT specimen are greater than the crack growth rates measured using CT specimens cut from any of the horizontal layers in the rail. The research team again speculated that the higher crack growth rates for the AHH CCT specimen were due to higher residual stresses that may be present in the larger CCT test specimen. For example, Figure 85 compares the CCT crack growth rates for the AHH rail with crack growth rates obtained from CT specimens tested at R=0.33 (both vertical and horizontal specimens). The CCT test results seem to be consistent with crack growth rates from CT specimens measured at an elevated R-ratio, e.g., R>0.33.

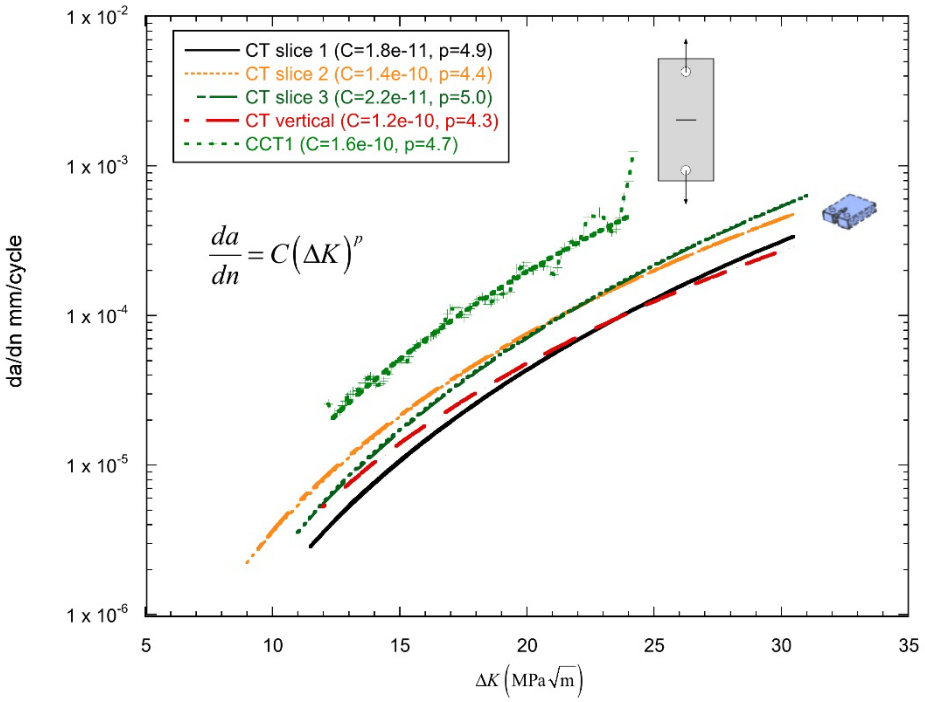

Figure 84. Comparison of fatigue crack growth rates from CT and CCT specimens for AHH rail. *R*=0.1

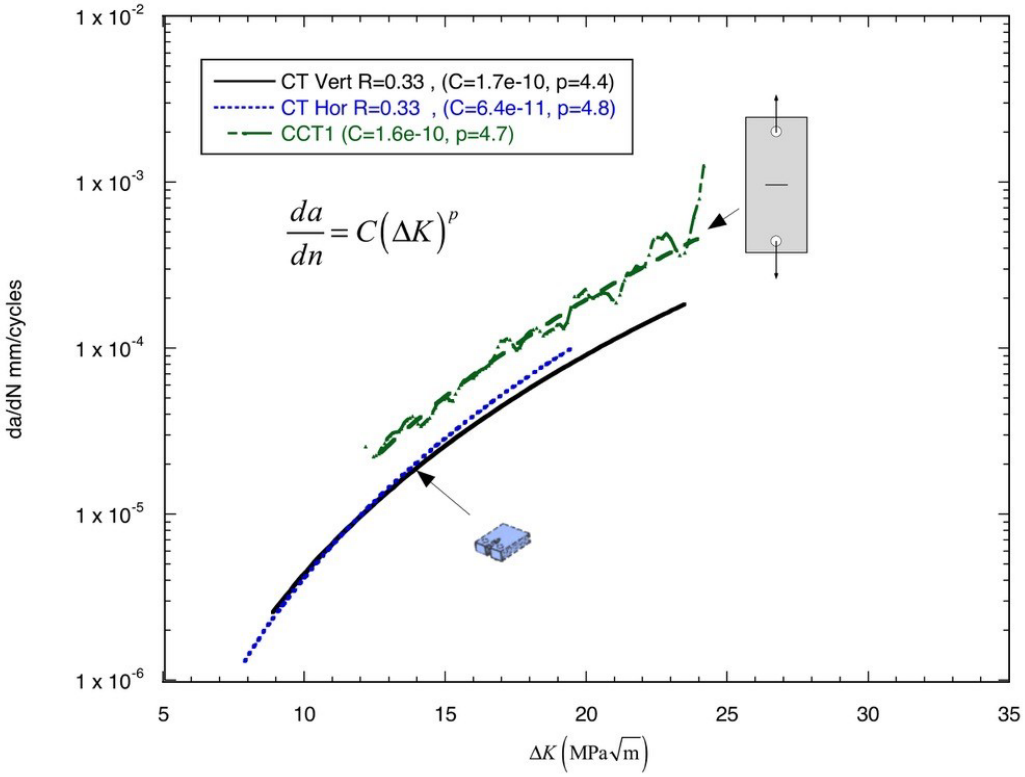

Figure 85. Comparison of fatigue crack growth rates from horizontal and vertical CT specimens (*R*=0.33) with CCT specimens from the AHH rail

2.8 Residual stresses

The importance of the residual stress effects on fatigue crack growth rates in legacy rails has been extensively investigated by Orringer, et al. [9, 10]. The investigation was based on the simulated fatigue service tests conducted at the Facility for Accelerated Service Testing (FAST) of the Transportation Technology Center in Pueblo, CO. The data was collected over the course of five months of simulated fatigue service tests and showed that fracture growth rates fell into two groups, as shown in Figure 86(a).

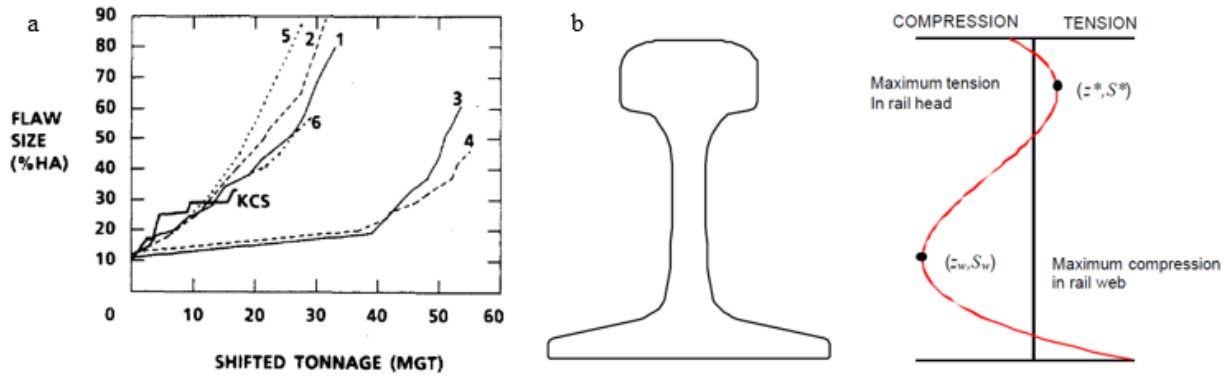

Figure 86. Residual stresses effect on legacy rails: (a) detail fracture growth curves with differences attributed to residual stresses [10], and (b) approximate distribution of the residual stresses through the rail height [8]

Since all the tested rails were similar and subjected to the same loading conditions, the significant differences in the observed crack growth rates between two rail groups (1, 2, 5, and 6 vs 3 and 4) in Figure 86 (a) were attributed to the differences in railhead residual stress.

There are several sources of residual stresses in rails: roller-straightening, heat treatment of the railhead, and wheel-rail contact. Modern rails produced for continuously welded track are roller-straightened (i.e., cold-worked) to meet strict tolerances on residual vertical camber and horizontal sweep. The residual stress field resulting from this process is approximately axially uniform except for about 18 in at each rail end. Previous experimental stress analyses have characterized the axially uniform region, which includes a tensile axial stress in the railhead [2]. Another important source of residual stresses in rails is the wheel-rail contact stress that causes local yielding of the rail. Previous microhardness measurements showed that the railhead is work-hardened by the wheel-rail contact to a depth of about 0.25 cm below the running surface and inward from the gage face. The axial residual stress is compressive in this region, and its magnitude approaches the work-hardened yield strength. An internal pocket of axial tension is also found in the heads of both roller-straightened and manually straightened rails [10]. While the authors recognize the importance of the residual stresses caused by the local plastification due to wheel-rail contact, reliable quantification of these stresses would require extensive experimental measurements conducted on service-worn rails, which is beyond the scope of the current project.

Introduction of the head-hardening process of modern rails produces a slight hardness gradient (as discussed above) as well as the residual stress. The non-uniform cooling of the railhead results in a non-uniform, self-equilibrating stress distribution through the height of the rail, which effectively contributes to the stress range as well as the R value. An example of the

residual stress distribution through the height of the rail section is shown in Figure 86 (b) [8]. The compressive residual stress near the running surface of the rail turns into tension for most of the head. As a result, a propagating detail fracture can encounter changing residual stresses. Thus, accurate assessment of residual stresses in modern head-=hardened rails is necessary for determining its influence on the fatigue crack growth rate and for establishing optimum inspection intervals.

A series of neutron diffraction measurements was performed at NIST's Center for Neutron Research and at Fraunhofer Institute to determine 3D stress state in the modern rails investigated in this study. Since all rails investigated here were unused, the residual stresses in these rails are due to the head-hardening process and roller-straightening (i.e., no wheel-rail contact effects). Eight mm thick plane stress cross-sectional rail slices cut from all investigated rails were used to measure in-plane residual stress distribution. Additionally, a longitudinal residual stress measurement in the AHH rail was conducted using a 3D half-rail specimen, cut along its axis of symmetry (Figure 91).

In the next section of the report, the authors discuss a basic principle of the neutron diffraction measurement method as well as its limitations affecting the number and type of specimens used. They also describe detailed finite element analyses conducted to optimize the specimens and aid in interpretation of the results, followed by a discussion of the measurement results obtained by NIST and Fraunhofer.

2.8.1 Neutron Diffraction Measurements

Neutron diffraction measurement technique relies on behavior of the diffracted beam of neutrons, which follow Bragg's law:

$$2d\,sin\theta = n\lambda \tag{1}$$

where d is the atomic lattice spacing, θ is the diffraction angle, and λ is the wavelength. Internal stress in the crystallographic material, such as steel, causes changes in the lattice spacing, i.e., $\Delta d = d - d_0$. This change leads to change in the diffraction angle $\Delta\theta$, which can be accurately measured using a beam with constant wavelength λ (Figure 87).

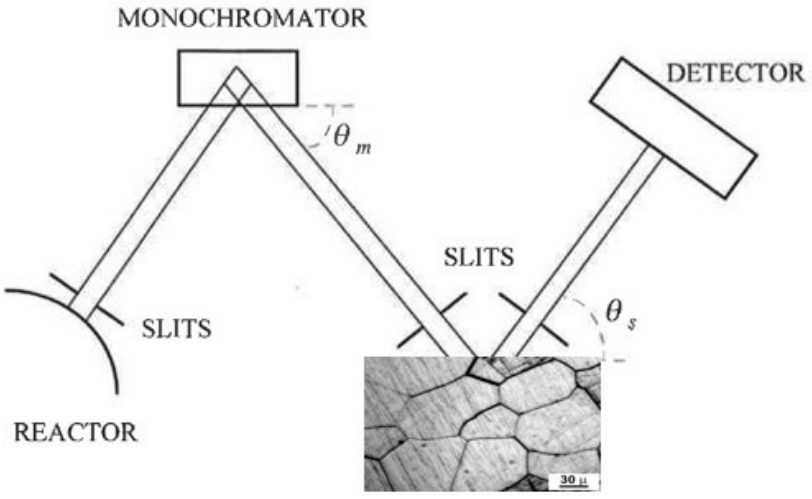

Figure 87. Neutron diffraction measurement schematic [3]

By differentiating Bragg's law and using the reference configuration in the stress-free condition (d_0, θ_0), strains and stresses in the material can be determined, as follows:

$$\Delta\theta = -\frac{\Delta d}{d_0} tan\theta_0 = -\varepsilon\, tan\theta_0 \;\rightarrow\; \varepsilon = -\Delta\theta\, cot\theta_0 \;\; ; \;\; \sigma = E\varepsilon \tag{2}$$

One of the main advantages of using neutron diffraction (as opposed to x-ray diffraction) is deeper penetration of neutrons into engineering materials (i.e., cm rather than mm for synchrotron x-rays or μm for laboratory x-rays). However, significant beam time is necessary to achieve sufficient penetration depths for accurate measurements inside the material, which constrains the size of the specimens that can be efficiently characterized. On the other hand, cutting the rail specimens for neutron diffraction measurements relieves residual stresses. Thus, careful planning of different cuts is necessary, along with quantification of the stress relief mechanisms introduced by these cuts. This was performed using detailed finite element analyses, as discussed in the following section of the report.

2.8.2 Specimen Optimization and Residual Stress Analyses

Residual stresses are 3D and self-equilibrating, which indicates a complicated distribution through the height and width of the railhead. Specimen optimization is therefore a compromise between minimizing the beam time (i.e., measurement time) by minimizing the specimen size, and preserving the residual stress state that exists in a full rail. Cutting the rail introduces free boundaries and relieves stresses in the direction normal to the cut surface. Thus, the specimen geometry must be considered in the context of the direction of stresses being investigated. Lateral and transverse residual stresses can be effectively determined using thin rail slices. Longitudinal stresses, on the other hand, require a long rail specimen that preserves the stress distribution along the rail. Figure 92 gives an example of the residual stresses measured by Luzin, et al. [4] using full rail sample of 530 mm length (top row) and corresponding thin slice measurements (bottom row).

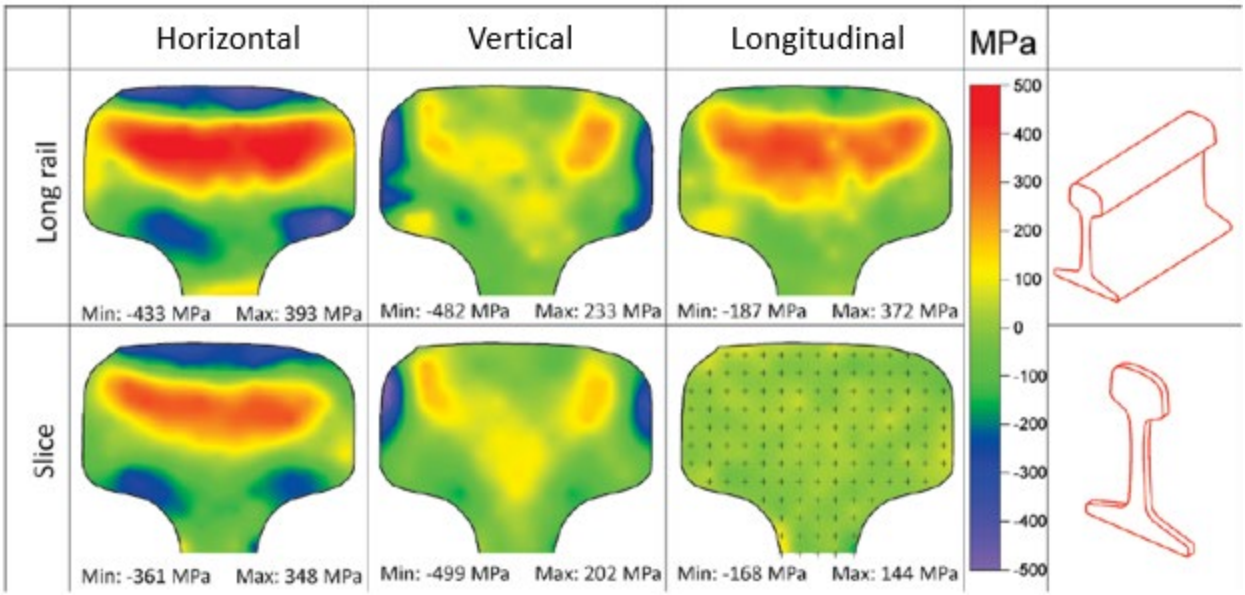

Figure 88. Example of residual stress measurements using full rail sample (top) and thin rail slices (bottom) [4]

The 530 mm long rail sample used by Luzin, et al. required approximately 3 months of beam time to determine the longitudinal stresses. This is highly impractical, considering the limited number of nuclear facilities that perform neutron diffraction measurements. While lateral and transverse stresses are important, the most consequential stress component for detail fracture growth is the longitudinal one. Thus, it is more important to determine the minimum size and shape of the rail specimen that preserves the longitudinal stress distribution. This was performed by investigating the effects of different types of rail specimen cuts and resulting change in the stress distribution. The research team first investigated two transverse cuts to determine the minimum rail specimen length. Subsequently, they investigated the effect of the longitudinal cut along the mid-section of the rail that splits the long rail specimen in half (longitudinally). The effects of these cuts on the residual stress state in the rail are analyzed using detailed finite element simulations.

Transverse Cuts

The main objective of the analysis conducted in this study is to determine the minimum length of the rail specimen that preserves the longitudinal residual stress. A detailed finite element representation of the full rail (136RE) geometry was used to reach this objective. Since residual stresses are elastic, the material model used in the analyses is also elastic.

There are many approaches to introduce self-equilibrating residual stresses into the rail finite element model. The approach followed here involves introducing two virtual cuts to the infinite rail model and applying longitudinal stress that is equal and opposite to the one measured in the legacy rail (as shown in Figure 86 [b]), modified to ensure that it is self-equilibrating (i.e., both the total force and moment are zero). This is equivalent to cutting the physical rail and relieving the locked-in residual stresses and then reapplying equal and opposite self-equilibrating stress to one of the free rail surfaces. This exercise was repeated for different effective lengths of the models (ranging from 10–30 cm) to examine the distance over which the applied stresses decay. The analysis results obtained with a 12 cm rail model (half-length due to symmetry) are shown in Figure 89.

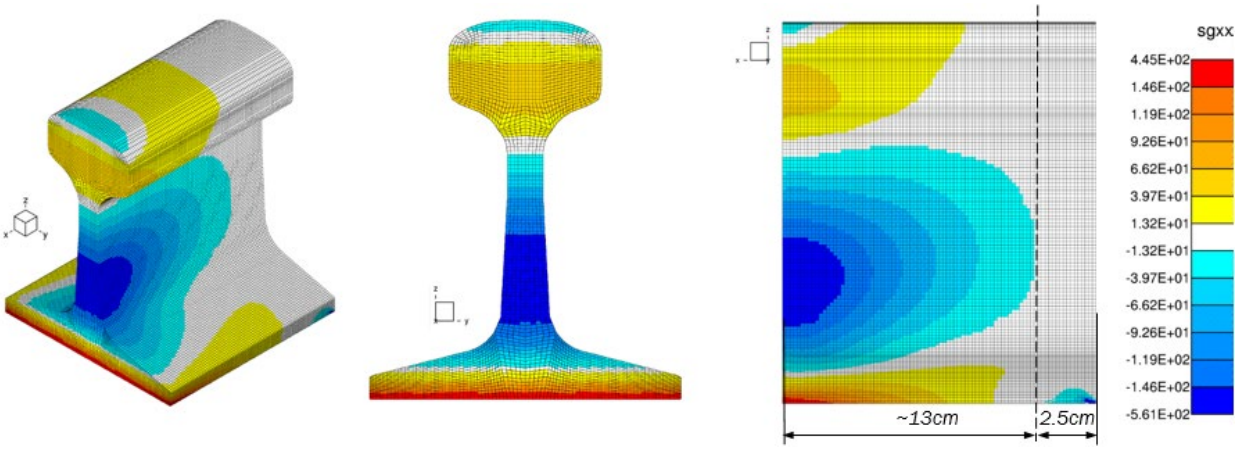

Figure 89. Longitudinal residual stress distribution, 15cm rail model (units MPa)

The results show the expected pattern of longitudinal stresses that match the applied stress near the application surface (left side of the model in Figure 89) and relatively fast decay as the free end is approached. The distance over which the stresses decay is approximately 13 cm, which is

less than the height of the rail (18.5 cm—136RE). The analysis was repeated using longer models, until the length over which the stresses decay did not increase significantly. Since there was no significant increase in the decay length calculated using both 20 cm and 25 cm rail models when compared to the 15 cm rail model, the minimum length of the rail specimen was determined to be 30 cm (i.e., 2 x 15 cm).

It is also worthwhile to examine the lateral stress in the rail resulting from application of the longitudinal stress. These results are presented in Figure 90.

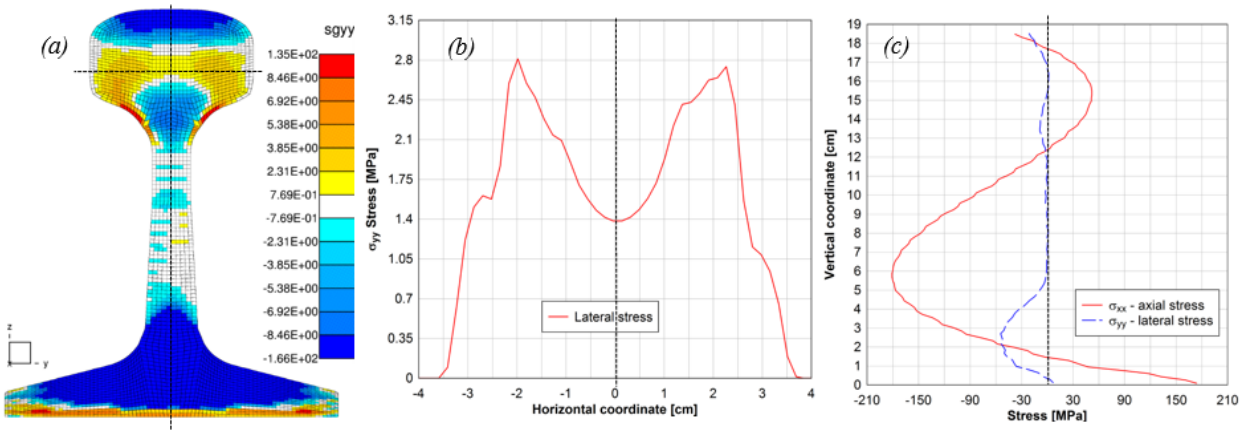

Figure 90. Lateral stress induced by the application of the longitudinal stress: (a) lateral stress maps on the rail surface where longitudinal stress was applied, (b) lateral stress across the width of the railhead, (c) longitudinal and lateral stresses along the height of the rail (units MPa, length in cm)

The analysis results indicate that the lateral stress caused by the application of the longitudinal stress is practically negligible. This suggests that the effect of longitudinal stress on the lateral stress is not significant for this rail geometry. It would be important to understand if reverse is also true, i.e., investigate the longitudinal stress caused by the application of the lateral stress. This is consequential for investigation of the effects of the longitudinal cut along the middle section of the rail, which will be considered next.

Longitudinal Cut

Considering the available beam time for the residual stress measurements at any neutron diffraction beam facility, further specimen size reduction is necessary. A longitudinal cut through the middle section of the rail was proposed, as shown in Figure 95.

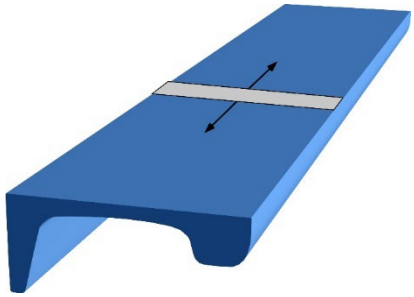

Figure 91. Proposed rail specimen for longitudinal stress measurements: cut along mid-section of the rail

Interpretation of the residual stress measured with the rail specimen shown above requires careful consideration of the effect of the longitudinal cut on the stress distribution inside the rail. Clearly, a longitudinal cut will significantly change the lateral (i.e., horizontal) stress distribution in the rail. It is not clear, however, what effect it will have on the longitudinal stress state.

The transverse cuts analyses discussed above indicated that application of the longitudinal stress has limited influence on the lateral stress. If the influence of lateral stress on the longitudinal stress state is also limited, then the longitudinal cut would primarily affect the lateral stress in the rail, while the longitudinal stress would remain approximately the same as before the cut was introduced. This scenario was analyzed using the same methodology as the transverse cut investigation. A detailed finite element model of the rail is used with a longitudinal cut shown in Figure 92. Lateral stress σ_{yy} is applied onto the free surface created by the cut, where the stress distribution is obtained from the literature data (Kelleher, et al. [9]). The applied stress was modified to ensure that it is self-equilibrating. Additionally, the maximum stress levels were reduced by a factor of 10 to ensure elastic behavior of the new half-rail section. This is equivalent to longitudinally cutting the physical rail and relieving the locked-in stresses, then reapplying equal and opposite self-equilibrating transverse stress to the surface created by the cut. The finite element model along with the applied transverse stress is shown in Figure 92.

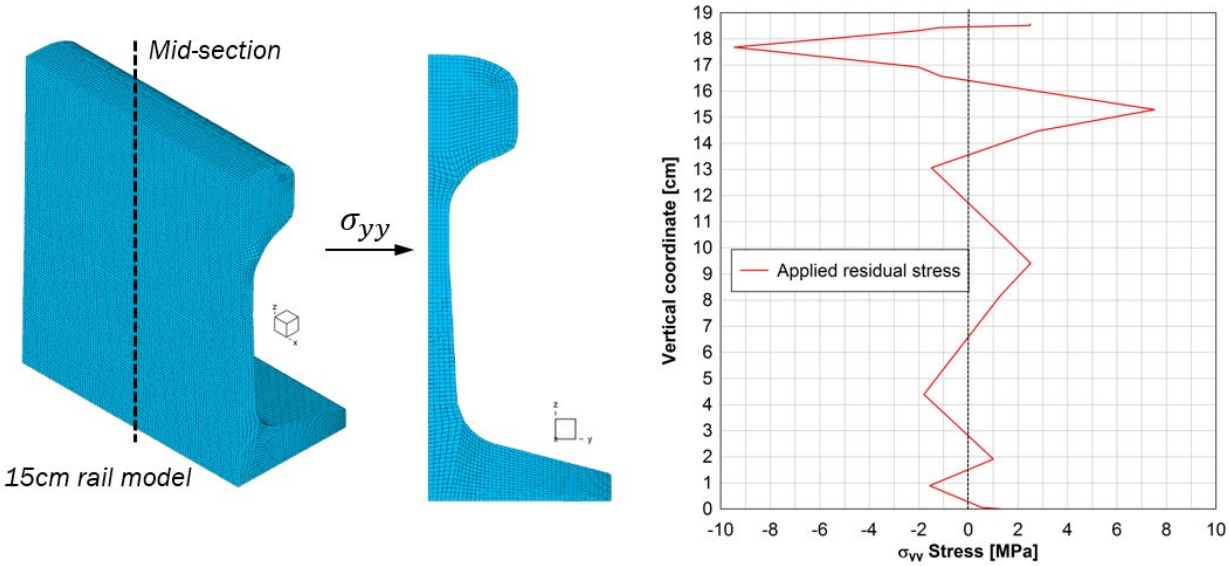

Figure 92. Investigation of the effect of longitudinal cut: 15cm half-rail model with lateral stress applied on the surface of the cut (applied lateral stress profile [9])

The results of the half-rail finite element analysis are given in Figure 93. The analysis results indicate that the longitudinal stress induced by the application of the lateral stress is on the same order as applied lateral stress. This means that significant changes of the lateral stress result in similar changes in longitudinal stress. Since the magnitude of the lateral residual stresses in the rails is typically similar to the longitudinal stress (Figure 88 [4]), relieving the lateral stress by introducing the investigated cut has a significant effect on the longitudinal stress state. In other words, the longitudinal cut does change the state of both lateral and longitudinal stresses in considered rail geometry (136RE).

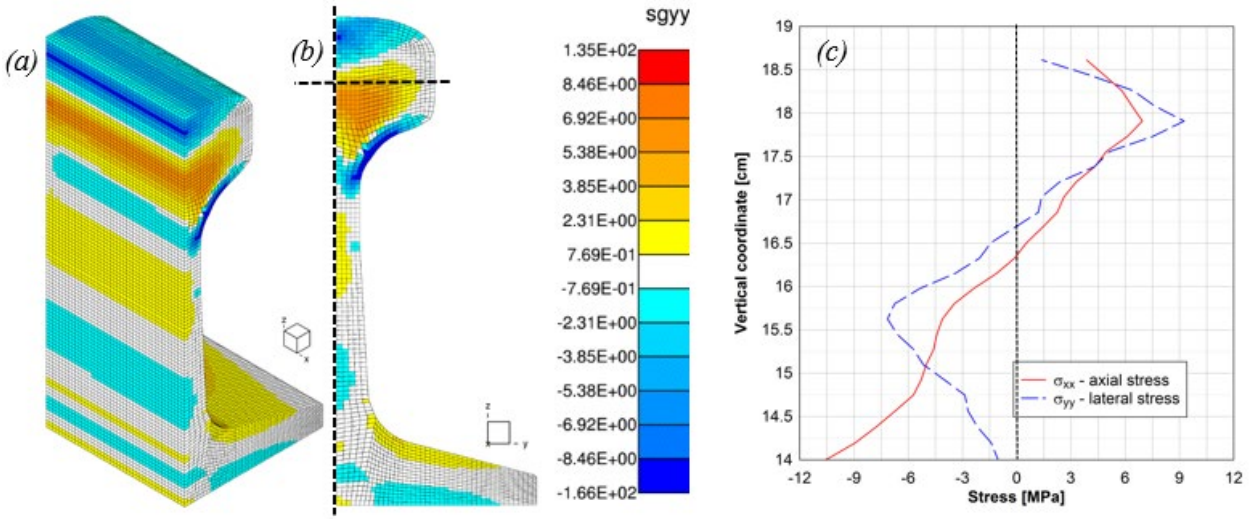

Figure 93. Longitudinal stress induced by the application of lateral stress: (a) applied lateral stress maps on the longitudinal middle surface—isometric view, (b) applied lateral stress on the middle surface of the rail, (c) longitudinal and lateral stresses along the height of the railhead (units MPa, length in cm)

The residual stress analyses discussed above indicate a complex interaction between different stress components in the rail. Thus, cutting the rail for neutron diffraction measurements requires careful investigation of the effects of various cuts on the residual stress state. We note that the analyses discussed here were performed based on data from published literature, as opposed to stress measurements conducted in support of the project. This is because the analyses were conducted to optimize the specimen and were completed before measurements were taken. Additionally, and more importantly, half-rail specimens (Figure 91) were used to measure the longitudinal residual stress, which are affected by the longitudinal cut, as the analysis above shows. Thus, the residual stress measurements taken here, while very important and valuable, provide only a partial representation of longitudinal residual stresses. Obtaining a complete representation would require solution of an inverse problem, i.e., determining the stress state that existed in the rail before the cut, based on stresses measured using cut specimen (i.e., half-rail – Figure 91). This will be pursued as part of the follow-up effort.

2.8.3 Neutron Diffraction Residual Stress Measurements

Dr. T. Gnaupel-Herold conducted residual stress measurements using neutron diffraction techniques at NIST's Center for Neutron Research. Three separate sets of residual stress measurements were conducted at NIST: 1) plane stress residual stress measurements on 8 mm thick cross-section slices taken from AHH, HH, and SS rails (Figure 94), 2) plane stress residual stress measurements on 8 mm thick cross-section slices taken from the HAY84 and CF&I77 rails, and 3) 3D residual stress measurements using half of an AHH rail cut along its axis of symmetry (Figure 91 and Figure 94 [b]). The residual stress measurements for the planar slices were conducted using a wavelength of 1.637 Å over a gauge volume of 42.875 mm^3 (3.5 x 3.5 x 3.5 mm cubes). The reported residual stress values are based on a grid spacing interval of 3 mm x 3 mm, with the grid plane located at the half-thickness of the rail slice, as shown in Figure 95.

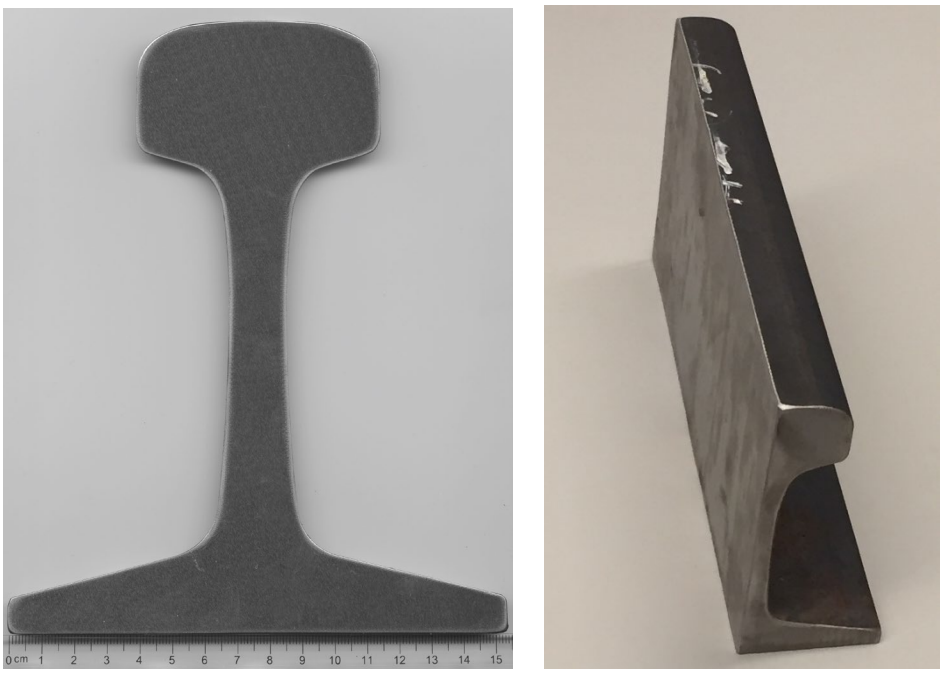

(a) (b)

Figure 94. Specimens for the residual stress measurements: (a) 8-mm thick cross-sectional slice used for plane stress measurements (i.e., no longitudinal component) and (b) 300mm half-rail specimen used for longitudinal residual stress measurement

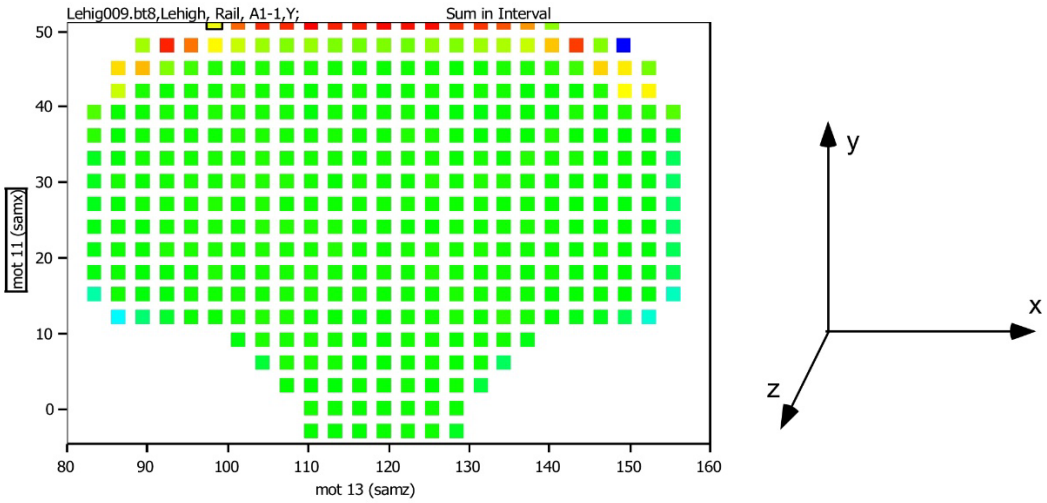

Figure 95. Grid of 384 residual stress measurement areas (3-mm x 3-mm each) in slice mid-plane (a different coordinate system was used than the one in Section 2.8.2.)

As expected, the neutron diffraction residual stress measurements showed that the longitudinal stress component σ_{zz} (note different coordinate system than used in the analyses in Section 2.8.2) is zero for all planar slices. The σ_{xx} (lateral) and σ_{yy} (transverse) stress contours for the HH, AHH, and SS rails are shown side by side in Figures 96–97. A minimum lateral

compressive residual stress, $\sigma_{xx} = -262$ MPa, was measured close to the running surface of the HH rail (Figure 96 [a]) and a maximum tensile residual stress, $\sigma_{xx} = 102$ MPa, was measured close to the center of the head in the AHH rail (Figure 96 [b]). Figure 97 shows that the maximum and minimum σ_{yy} stress components both occur in the SS rail: $\sigma_{yy}^{min} = -192$MPa, $\sigma_{yy}^{max} = +162$MPa. The details of these maximum measured residual stress values from contour plots Figs. 96a, 96b, and 97c are shown enlarged in Figures 98–100.

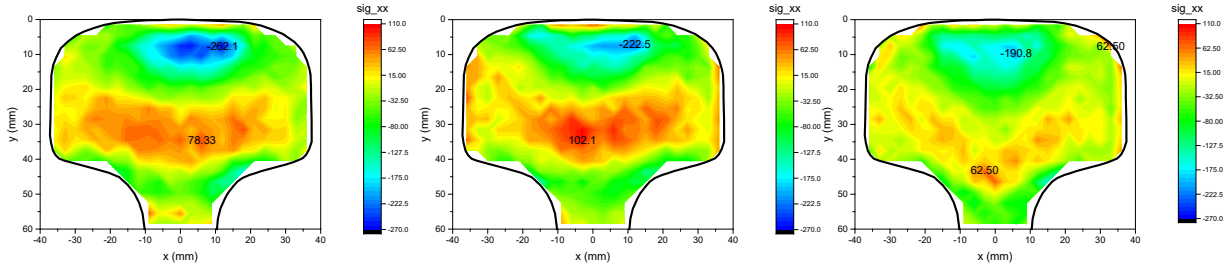

(a) (b) (c)

Figure 96. Contour plots comparing the lateral residual stress component σ_{xx} in rails: (a) HH, (b) AHH, and (c) SS respectively, scale -270 MPa (blue), 110 MPa (red)

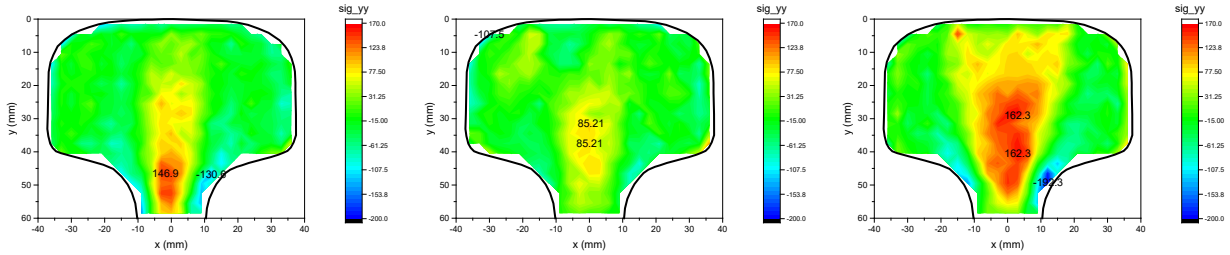

(a) (b) (c)

Figure 97. Contour plots comparing the transverse residual stress component σ_{yy} in rails: (a) HH, (b) AHH, and (c) SS respectively, scale -200 MPa (blue) – 170 MPa (red)

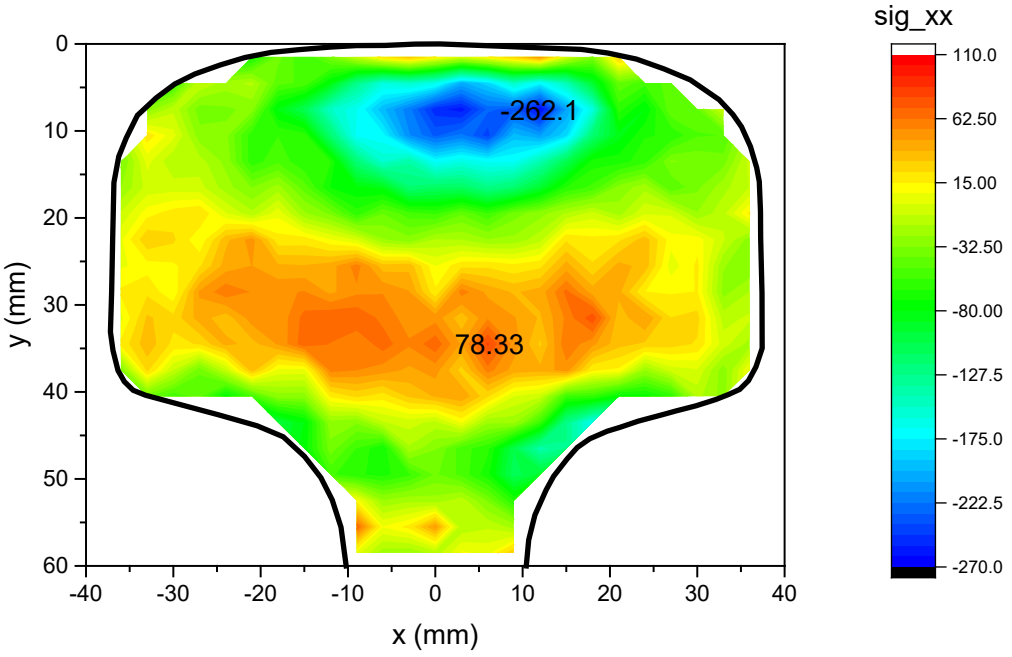

Figure 98. Enlargement showing lateral residual stress contours for HH rail (σ_{xx})

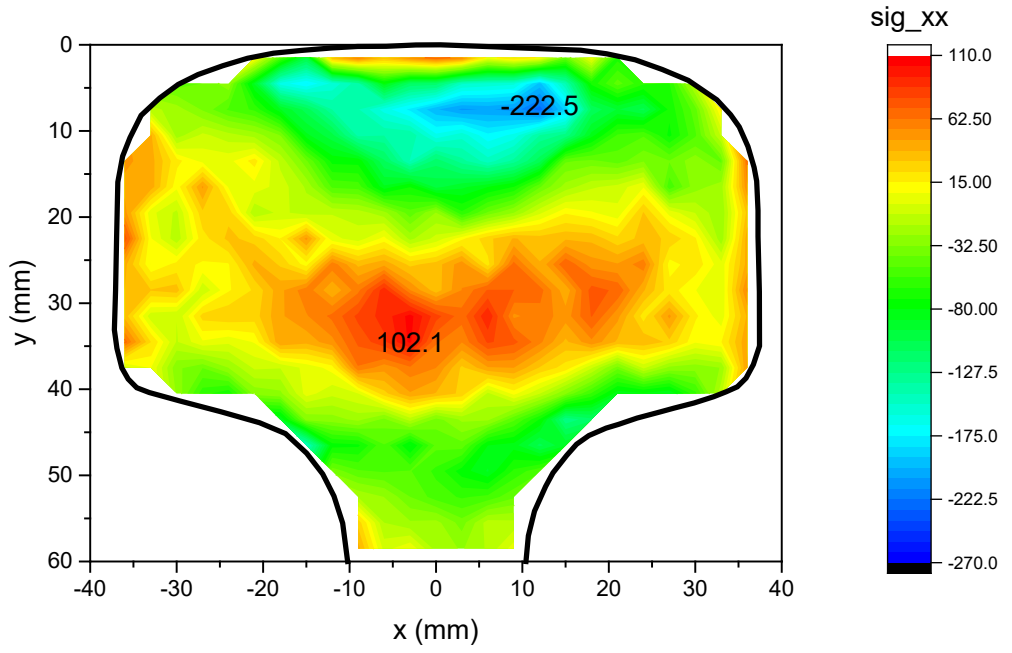

Figure 99. Enlargement showing lateral residual stress contours for AHH rail (σ_{xx})

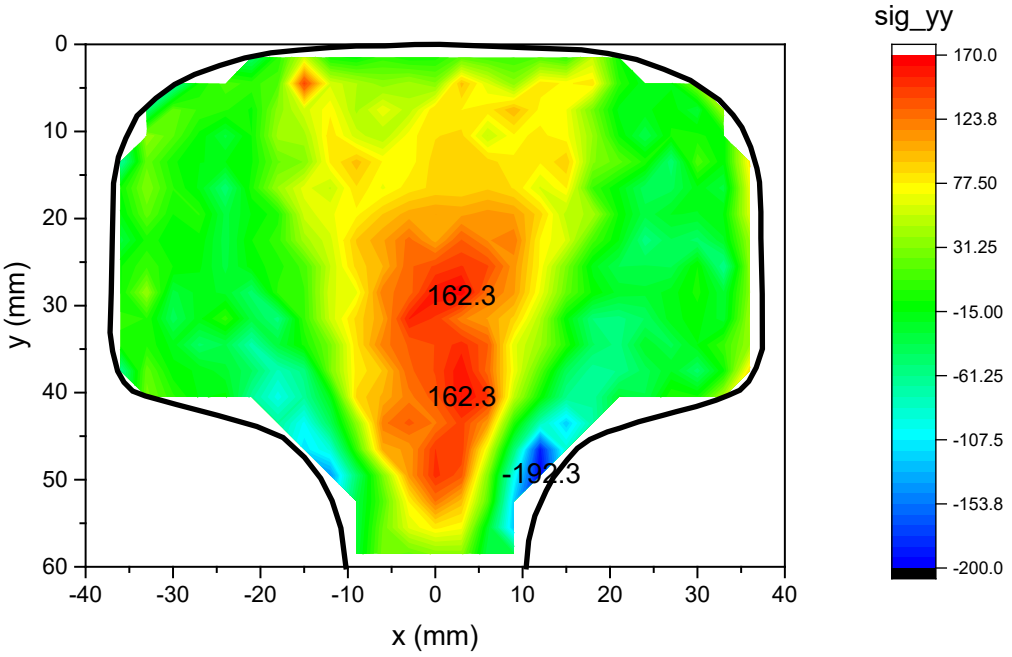

Figure 100. Enlargement showing transverse residual stress contours for SS rail (σ_{yy})

Figure 100 shows that in the SS rail, the maximum σ_{yy} in tension is located in the central portion of the railhead, while the maximum compressive σ_{yy} occurs on the rail surface at the transition from the flange to the railhead.

NIST also measured the planar residual stresses, σ_{xx}(lateral) and σ_{yy} (transverse), in the legacy rails, HAY84 and CF&I77. The stress components for the HAY84 rail are shown in Figure 101 and for the CF&I77 rail in Figure 102. The residual stresses in the legacy rails are considerably lower than the stresses measured in the modern rails. As can be seen by comparing these figures, the minimum and maximum residual stresses are slightly higher in the HAY84 rail. For example, in the HAY84 rail (Figure 101) the minimum and maximum σ_{xx} residual stress components are $\sigma_{xx}^{\min} = -144$MPa, $\sigma_{xx}^{\max} = +57$MPa, and the minimum and maximum σ_{yy} residual stress components are $\sigma_{yy}^{\min} = -89$MPa, $\sigma_{yy}^{\max} = +77$MPa. This contrasts with the residual stresses in the CF&I77 rail (Figure 102), where the equivalent minimum and maximum σ_{xx} residual stresses are $\sigma_{xx}^{\min} = -55$MPa, $\sigma_{xx}^{\max} = +56$MPa, and the minimum and maximum σ_{yy} residual stresses are $\sigma_{yy}^{\min} = -39$MPa, $\sigma_{yy}^{\max} = +52$MPa.

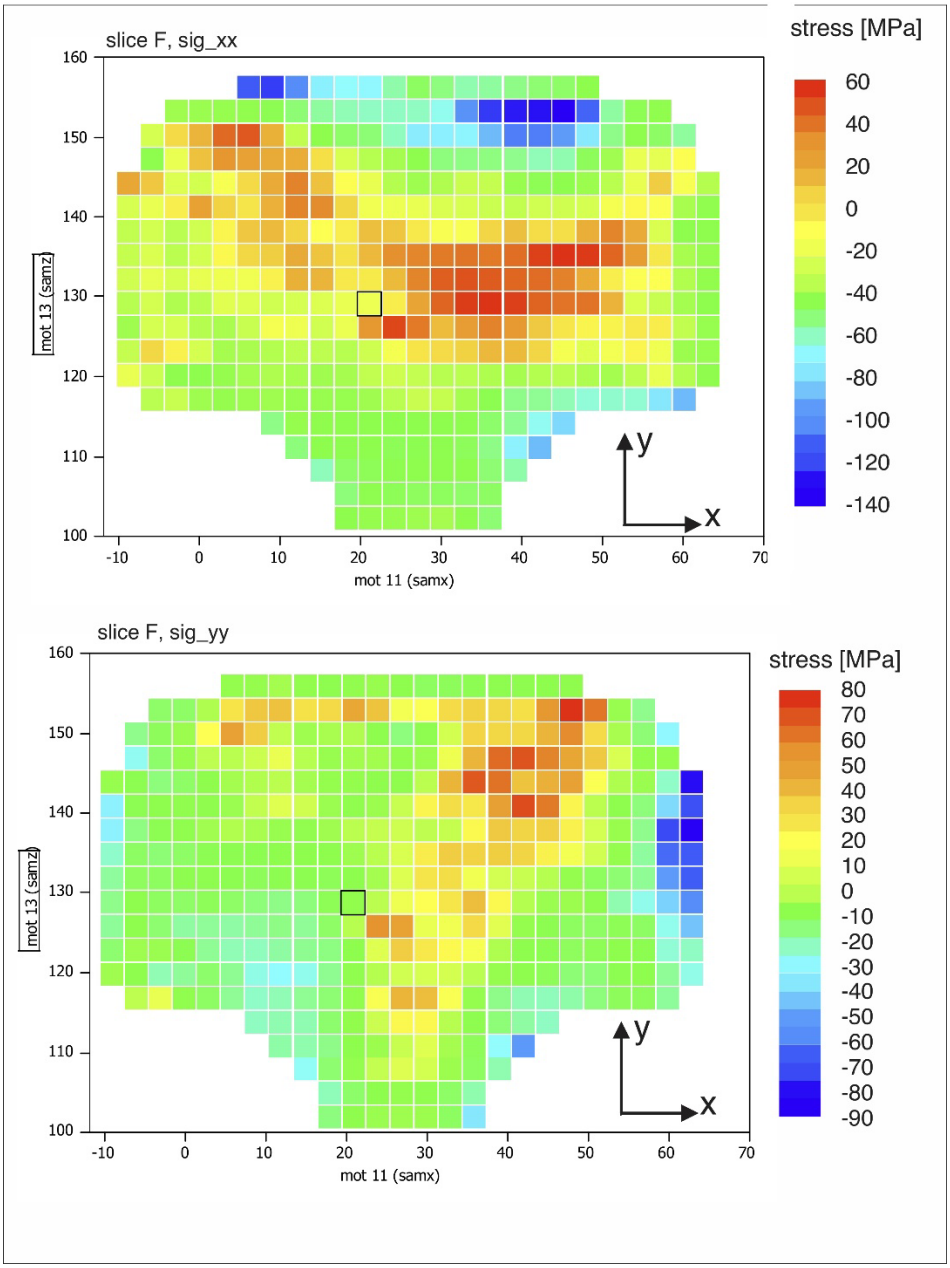

Figure 101. Residual stresses σ_{xx} and σ_{yy} in the legacy HAY84 rail

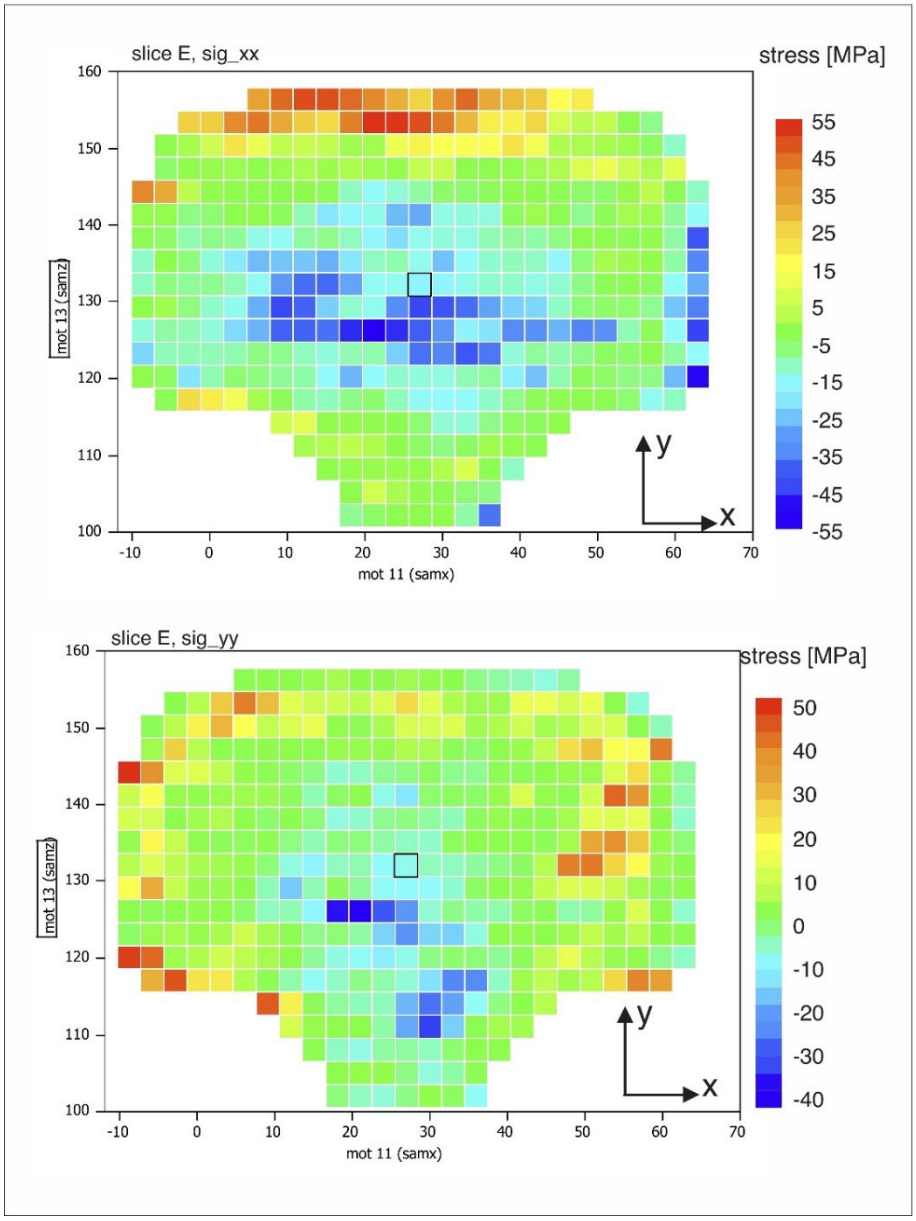

Figure 102. Residual stresses σ_{xx} and σ_{yy} in the legacy CF&I77 rail

Measurement of the longitudinal residual stresses using neutron diffraction cannot be conducted using the rail slices discussed above, since cutting these slices relieves the longitudinal stresses. A full 3D section of rail is needed to measure longitudinal residual stresses (Section 2.8.2), which is very challenging, as it requires an excessive amount of beam time (e.g., weeks of continuous measurement). Dr. M. Farajian of IWM attempted to make a limited number of longitudinal residual stress measurements at selected points in the upper corner of the AHH rail. For these measurements, a 300 mm long section of the AHH rail was placed in the neutron beam source at the Helmholz-Zentrum Berlin (HZB). Figure 103 shows the AHH rail test specimen in the HZB neutron diffraction residual stress measurement facility. Unfortunately, because of difficulties in making these measurements within a very limited time, only preliminary residual

stress measurements were obtained at the desired points (Figure 104). The completion of these measurements, when beam time can be obtained at HZB, is a recommend item for future work.

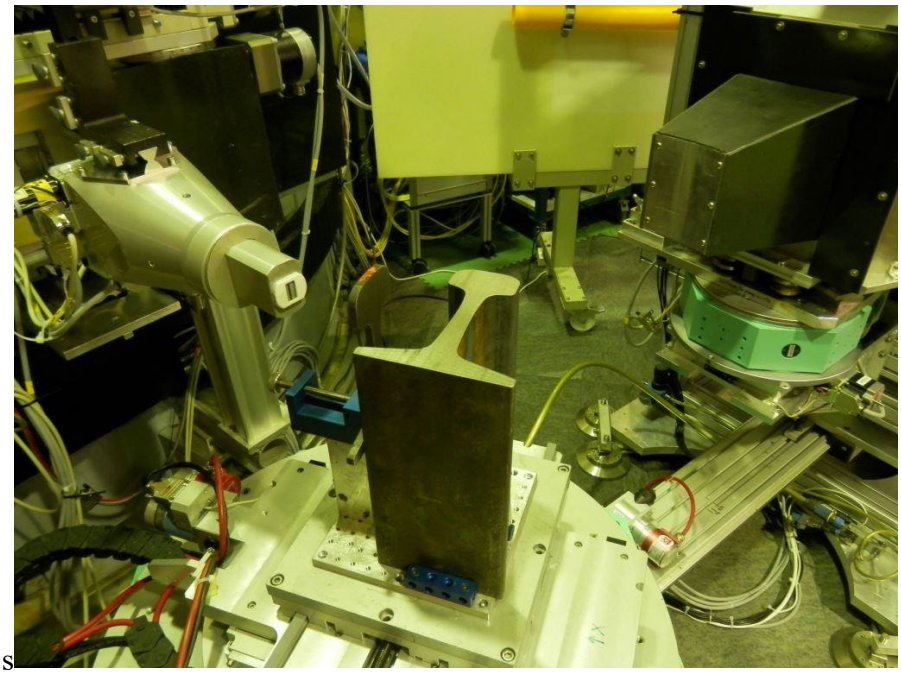

Figure 103. Residual stress measurements on a 300 mm section of the AHH rail using the neutron source at Helmholz-Zentrum Berlin (HZB)

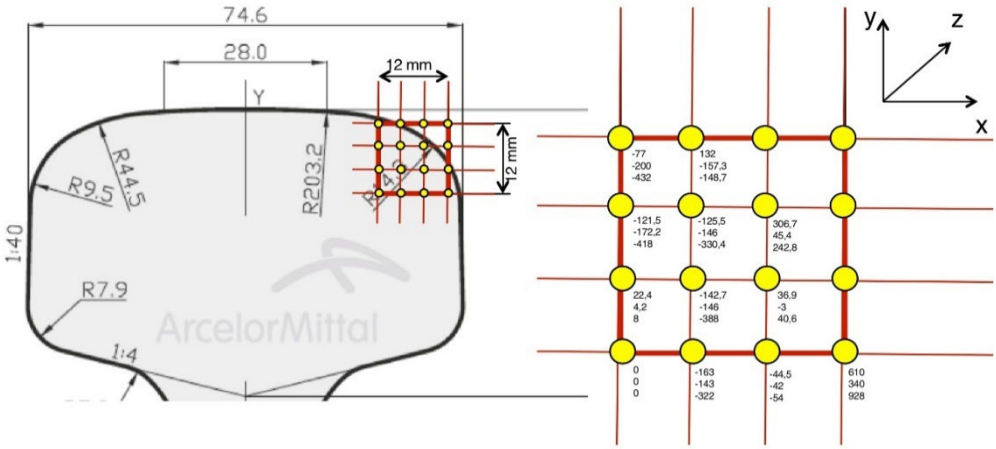

Figure 104. Preliminary longitudinal residual stress measurements from corner of AHH rail

After consultation with Dr. Gnaupel-Herold at NIST, the research team decided to attempt neutron diffraction residual stress measurements on a 300 mm long section of the AHH rail cut down the rail's axis symmetry (Figure 94 [b]). This reduction in the mass substantially reduces the necessary beam time, but at the expense of altering the internal residual stresses, as discussed in Section 2.8.2. From the analyses, the team concluded that it is possible to combine finite element simulation with the residual stress measurements on half of the rail to approximate the longitudinal residual stresses. This will be investigated in detail in the next phase of the project.

Before examining the longitudinal residual stresses measured with a half-rail specimen shown in Figure 94 (b), it is useful to investigate the lateral and transverse stresses and compare the results with the corresponding measurements made with the rail slices. Figure 105 shows a comparison of the lateral stress component (σ_{xx}) measured on the mid-plane of the long half-rail section, with the same stress component measured on the symmetric 8 mm thick (plane stress) slice (Figure 99). The difference between these two residual stress measurements is striking. As expected, on the vertical plane of symmetry, σ_{xx} becomes smaller on the free surface of the split rail (Figure 105 [a]). However, it is not clear why large compressive stresses are reported at the top and bottom of the specimen (Figure 105 [a]), which appears to violate the traction-free boundary condition on the cut vertical plane of symmetry. Additionally, the tensile lateral stress measured on the vertical mid-plane of the half-rail section is significantly higher than the corresponding level obtained for the same rail with the plane stress slices. In the Figure 105 (a) image, $\sigma_{xx}^{\min} = -209$MPa, $\sigma_{xx}^{\max} = +236$MPa. In the symmetric, plane stress, cross-section, Figure 105 (b), $\sigma_{xx}^{\min} = -227$MPa, $\sigma_{xx}^{\max} = +105$MPa.

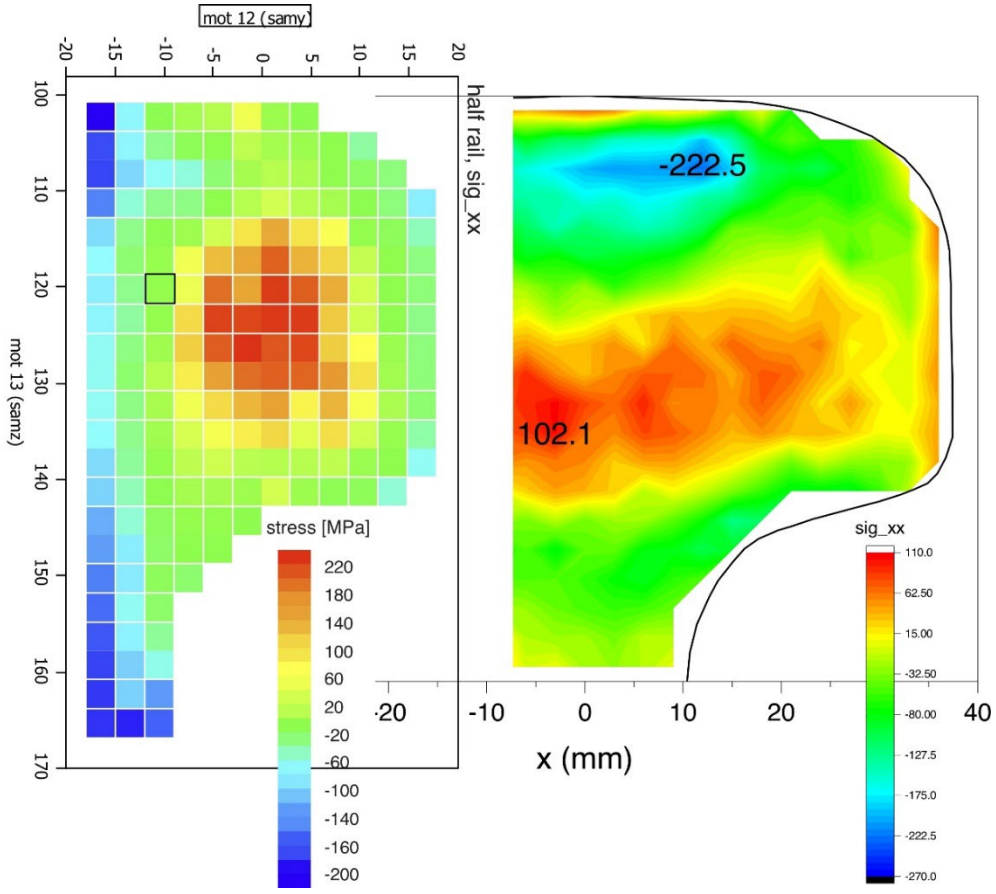

Figure 105. Comparison of the lateral residual stresses (σ_{xx}) measured in AHH rails: (a) σ_{xx} measured in 300-mm long half-rail section, (b) σ_{xx} measured in 8-mm thick planar section (Figure 99)

Figure 106 shows a similar comparison for the transverse stress component (σ_{yy}). In Figure 106 (a), $\sigma_{yy}^{min} = -188$MPa, $\sigma_{yy}^{max} = +221$MPa. In the symmetric, plane stress cross-section shown in Figure 106 (b), $\sigma_{yy}^{min} = -172$MPa, $\sigma_{yy}^{max} = +152$MPa. While the peak compressive and tensile values appear similar, the distribution is not. Based on the available results, it is difficult to attribute these differences to any effect. However, it can be concluded that cutting the rail specimens for neutron diffraction measurements of residual stresses is highly consequential for the actual stress distribution. This also indicates that the interaction between different stress components is even more consequential than suggested by the results of the finite element analyses discussed in Section 2.8.2.

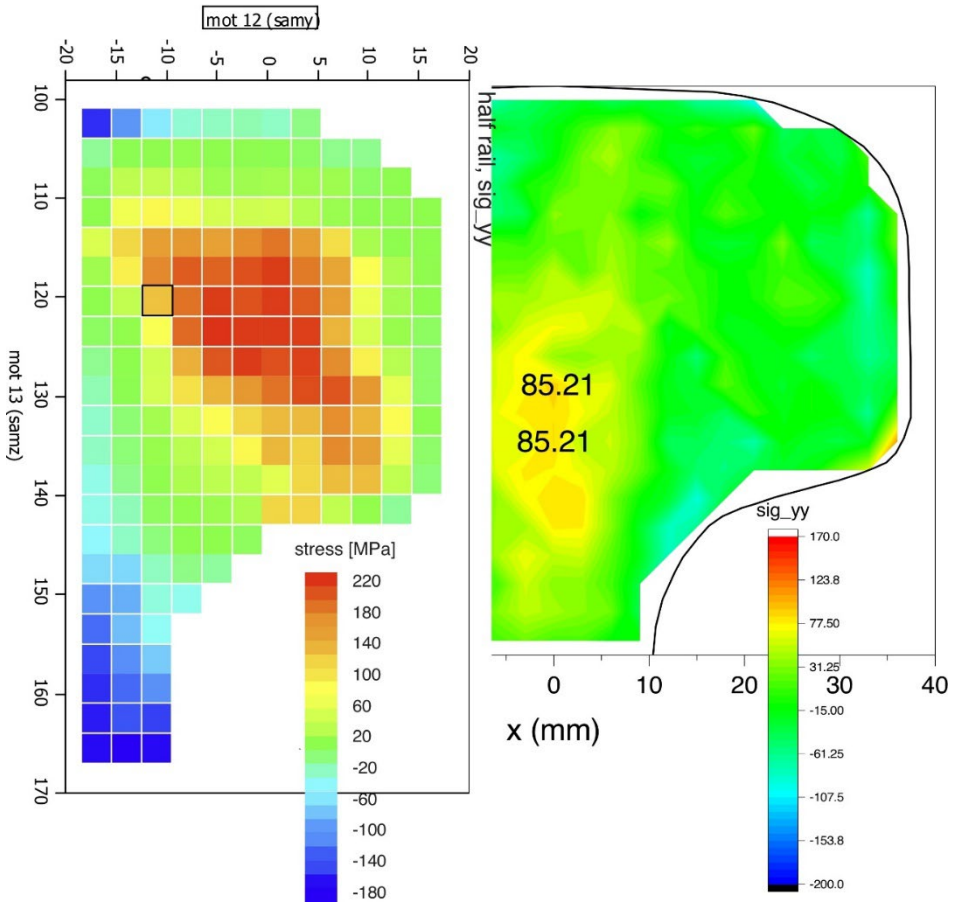

(a) (b)

Figure 106. Comparison of the transverse residual stresses (σ_{yy}) measured in AHH rails: (a) σ_{yy} measured in 300 mm long half-rail section, (b) σ_{yy} measured in 8-mm thick planar section (Figure 101 [b])

Figure 107 shows the longitudinal stress component (σ_{zz}) measured in the center (i.e., mid-length) of the half-rail sample. The peak compressive stress is $\sigma_{zz}^{min} = -222$MPa and the peak tensile stress is $\sigma_{zz}^{max} = +356$MPa. High tensile stress in the railhead is especially important for

transverse fracture growth. The authors note, however, that the stress distribution shown in Figure 107, as well as the comparative analysis of the lateral and transverse stresses obtained with a 3D half-rail and plane stress slices, point to complicated interaction between the stress components and significant effects of cutting the rail specimen. This makes a clear interpretation of the measured values and distribution of longitudinal residual stresses challenging.

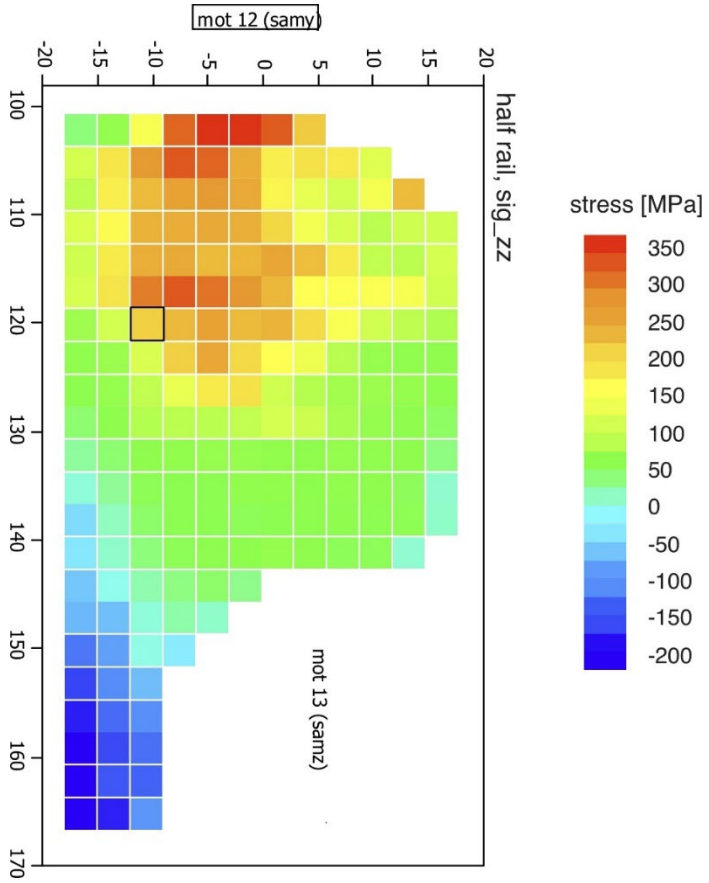

Figure 107. Longitudinal (σ_{zz}) stress component measured in the split 300 mm long AHH rail

The analysis of the residual stress measurements conducted with the 3-D half-rail specimen points to complexities of the residual stress distribution in rails as well as significant challenges related to their measurement. Ideally, the residual stress measurements in all directions should be conducted with a full 3-D rail section (as opposed to half-rail) and repeated multiple times to verify the accuracy. Given the beam time required to perform such measurements, this is simply prohibitive. At the same time, clear interpretation of the residual stress state based on partial measurements conducted with half-rail specimens or plane stress slices, proved nearly impossible. These challenges can be alleviated, to a certain degree, through detailed finite element simulations aimed at recreating the stress state in the rail before it was cut. This however requires solution of the inverse problem, which is also challenging. A residual stress analysis effort is envisioned for the next phase of this project, with a goal of approximating a full 3D residual stress distribution. However, we recognize that a separate, dedicated multi-year effort is required to fully understand the residual stress distribution in rails. Such an effort should involve both extensive new measurements supplemented by detailed finite element analysis.

3. Data Summary and Reduced Testing Protocol

One of the main objectives of this project was to perform a thorough investigation of the effects of the microstructural gradient and residual stresses on detail fracture propagation in head-hardened rails, in reference to legacy rails. This information is necessary to determine if the rail inspection interval established for legacy rails, is valid for head-hardened rails. A comprehensive experimental program supplemented by advanced numerical analysis was developed and executed here. This resulted in multiple fundamental insights into key effects and their relative importance for detail fracture growth in rails. These insights can be used to establish a reduced testing protocol for characterization of rails not included in the current study.

Based on the experimental data collected for five representative rails (two modern head-hardened, one modern control, and two legacy rails), trends of behavior were identified (Table 9). These trends can be considered representative of rails today, which provides a basis for reduced testing protocol outlined in Table 9.

Table 9. Summary of the trends in collected data and recommendation for inclusion in the reduced testing protocol

Experimental Tests Performed	Test Standard	Conclusion and Trends	Inclusion in Reduced Testing Protocol
Chemical analysis of legacy rail steel	AREMA	Chemical composition for all rails within (or exceeding) AREMA guidelines	Yes
Tensile test data	AREMA	Tensile data consistent with previous measurements [11] and AREMA standards	Yes, select railhead location
Hardness data	AREMA	Hardness consistent (or exceeding) with AREMA guidelines.	Yes, railhead
Light optical microscopy (LOM) – interpretation of the hardness map	-	Uniform perlitic microstructure for all rails; thickness of decarb layer observed	No
Hitachi 4300 High Resolution Field Emission SEM – samples removed based on LOM results	-	Cementite / ferrite spacing responsible for hardness and strength variations	No
Compact tension (CT) specimens – K_{Ic} plane strain toughness	ASTM E399	Fracture toughness fairly uniform across all rails and within each railhead.	Yes, select locations
Compact tension specimens – fatigue tests (da/dN tests); additional verification tests with center cracked tension specimen (CCT)	ASTM E647	The fatigue crack growth rate behavior as a function of ΔK is similar for all investigated rails.	Yes, selected locations
Neutron diffraction residual stress measurements		Prohibitive beam time needed for full 3D characterization; Significant interaction between stress components; Large longitudinal residual stress – critical for detail cracks; Need for a dedicated residual stress effort	Yes, measure residual stress in CCT specimens before testing *Need for a separate residual stress research program*

4. Conclusion

In this study, the team performed a comprehensive fatigue and fracture characterization effort for modern head-hardened rails in reference to legacy rails. The main objective of the program was to determine if the head-hardening process, designed to improve the wear resistance of rails, resulted in reduction of fatigue life. This was achieved by detailed investigation of the fatigue crack growth rates and fracture properties of the rail material as well as spatial variability of these properties inside the railhead. Additionally, residual stress measurements were conducted to determine their magnitude and distribution. The key findings are as follows:

1. The head-hardened rails are significantly harder and stronger than legacy rails. Maximum hardness and strength occur near the running surface of the railhead, which significantly improves wear resistance.
2. All investigated rails (modern [head-hardened] and legacy [non-head-hardened]) have a uniform pearlitic microstructure except near the surface of the railhead, where a mixed ferrite/pearlite microstructure is observed. This is caused by decarburization that leads to local carbon depletion during high temperature processing. The depth of the decarburized layer is approximately 1 mm for all rails with varying density of ferrite, which is highest in the HAY84 rail and lowest in the AHH rail.
3. Despite significant hardness and strength variation between different rails, fracture toughness is mostly uniform across all rails: mean $K_{Ic} = 36.4\ MPa\sqrt{m}$ with a standard deviation of $\sigma = 2.3$). Variation of toughness within each railhead at different depths from the running surface is like toughness variation across all rails. For example, mean toughness in the AHH railhead: $K_{Ic} = 37.8\ MPa\sqrt{m}$ with a standard deviation of $\sigma = 2.8$; SS and HAY84 railheads: $K_{Ic} = 35.0\ MPa\sqrt{m}$ with a standard deviation of $\sigma = 1.9$; CF&I77 railhead: $K_{Ic} = 41.3\ MPa\sqrt{m}$ with a standard deviation of $\sigma = 3.8$.
4. Fatigue crack growth rate is also similar across all rails, with the biggest difference occurring at low ΔK. However, at low crack growth rates, the relative error associated with determination of Δa is also greater, which could lead to overestimation of the differences between the crack growth rates across all rails. Overall, the fatigue crack growth rate behavior as a function of ΔK is very similar for all investigated rails.
5. Residual stresses due to head hardening and roller straightening are significant, with longitudinal stresses reaching the highest level of approximately ~350MPa. Accurate neutron diffraction measurement of full 3D distribution of residual stresses is challenging due to the prohibitively long beam time required to penetrate the rail material. Cutting smaller rail samples, such as plane stress slices and half-rail samples reduces the necessary beam time, making direct measurements possible. Unfortunately, this also leads to complicated 3D stress redistribution, which makes interpretation of the residual stress state very challenging. Further investigation of the residual stress distribution as well as the wheel-rail contact influence is needed for a complete assessment of the residual stress effect on transverse crack growth in modern rails.
6. Detailed characterization of the microstructure and fatigue and fracture properties across all investigated rails, including spatial variability within each rail, provided fundamental insights into the key effects that can be attributed to the head hardening process. This

allows distinguishing the first and second order effects and developing a reduced testing protocol for a general characterization of rails. This testing protocol can be used to characterize other types of rails that have not been investigated as part of this project.

Increasing the hardness and strength of material to improve its wear resistance can be expected to reduce toughness and increase fatigue crack growth rate. In the case of modern, head-hardened rails, this is not the case. The results of this study show that the head hardening process of modern rails does not significantly reduce their toughness or fatigue crack growth resistance. This indicates that fatigue—rather than abrasive wear—can become the limiting factor for the overall life of the rail, which places higher emphasis on rail inspection and fatigue life assessment.

While this conclusion has been reached based on the investigation of five specific rails, they are considered representative of most rails that exist today.

5. References

1. Bramfitt, B. and Fletcher, F., "A Perspective on the Manufacture of Modern-Day High-Strength Steel Rail," presented at the AREMA 2013 Annual Conference and Exposition.
2. Budianksy, B. and Hutchinson, J.W., "Analysis of Closure in Fatigue Crack Growth" *J. Appl. Mech.*, vol. 45, no. 2, pp. 267–276, 1978, doi: 10.1115/1.3424286.
3. Gnaupel-Herold, T., Brand, P.C., and Prask, H.J., *Neutron Diffraction Investigation of Residual Stresses in Transverse/Oblique Rail Slices Subjected to Different Grinding Strategies - NISTIR 6305*, 1999.
4. Luzin, V., et al., "Neutron residual stress measurements in rails," *Neutron News*, vol. 24, no. 3, pp. 9–13, 2013, doi 10.1080/10448632.2013.804353.
5. Lyons, M.L., Jeong, D.Y., and Gordon, J.E., "Fracture Mechanics Approach to Estimate Rail Wear Limits," *Proceedings of the 2009 ASME Rail Transportation Division Fall Technical Conference*, October 20–21, 2009, pp. 137–146, doi 10.1115/RTDF2009-18035
6. Jeong, D.Y., Tang, Y.H., Orringer, O., *Estimation of Rail Wear Limits Based on Rail Strength Investigations*, DOT/FRA/ORD-98/07, 1998.
7. Jeong, D.Y., Tang, Y.H., Orringer, O., and Perlman, A.B., *Propagation Analysis of Transverse Defects Originating at the Lower Gage Corner of Rail*, DOT/FRA/ORD-98/06, 1998.
8. Jeong, D.Y., *Correlations Between Rail Defect Growth Data and Engineering Analyses, Part I: Laboratory Tests*, UIC/WEC Joint Research Project on Rail Defect Management Report, U.S. Department of Transportation, Volpe National Transportation Systems Center, 2003.
9. Kelleher, J., Prime, M.B., Buttle, D., Mummery, P.M., Webster, P.J., Shackleton, J., and Withers, P.J., "The Measurement of Residual Stress in Railway Rails by Diffraction and Other Methods," *Journal of Neutron Research,* vol. 11, no. 4, pp. 187–193, 2003, doi 10.1080/10238160410001726602.
10. Orringer, O., Morris, J.M., and Jeong, D.Y., "Detail Fracture Growth in Rails: Test Results," *Theoretical and Applied Fracture Mechanics*, vol. 5, issue 2, pp. 63–95, 1986, doi 10.1016/0167-8442(86)90019-4.
11. Orringer, O., Tang, Y.H., Gordon, J.E., Jeong, D.Y., Morris, J.M., and Perlman, A.B., *Crack Propagation Life of Detail Fractures in Rails*, DOT/FRA/ORD-88/13, 1988.
12. Orringer, O., Control of Rail Integrity by Self-Adaptive Scheduling of Rail Tests, DOT/FRA/ORD-90/05, 1990.
13. Pazdanowski, M., *Residual Stresses as a Factor of Railroad Rail Fatigue*, Technical transactions Civil Engineering, 4-b/2014, 2014.
14. Sih, G.C. and Tzou, D-Y., "Three-dimensional transverse fatigue crack growth in rail head," *Theoretical and Applied Fracture Mechanics*, vol. 1, issue 1, 103–115, 1984, doi 10.1016/0167-8442(84)90024-7.

15. Wineman, S.J., “Residual Stresses and Web Fracture in Roller-Straightened Rail,” Ph.D. dissertation, Dept. of Mechanical Engineering, MIT, 1991 http://hdl.handle.net/1721.1/26829.

16. Zhan, X. and Wang, S., “Research on the Improvement of Rail Head Hardening Technology on Railway,” *Proceedings of the Eastern Asia Society for Transportation Studies*, vol. 5, 263–271, 2005.

Appendix A. Hardness Values as a Function of Position

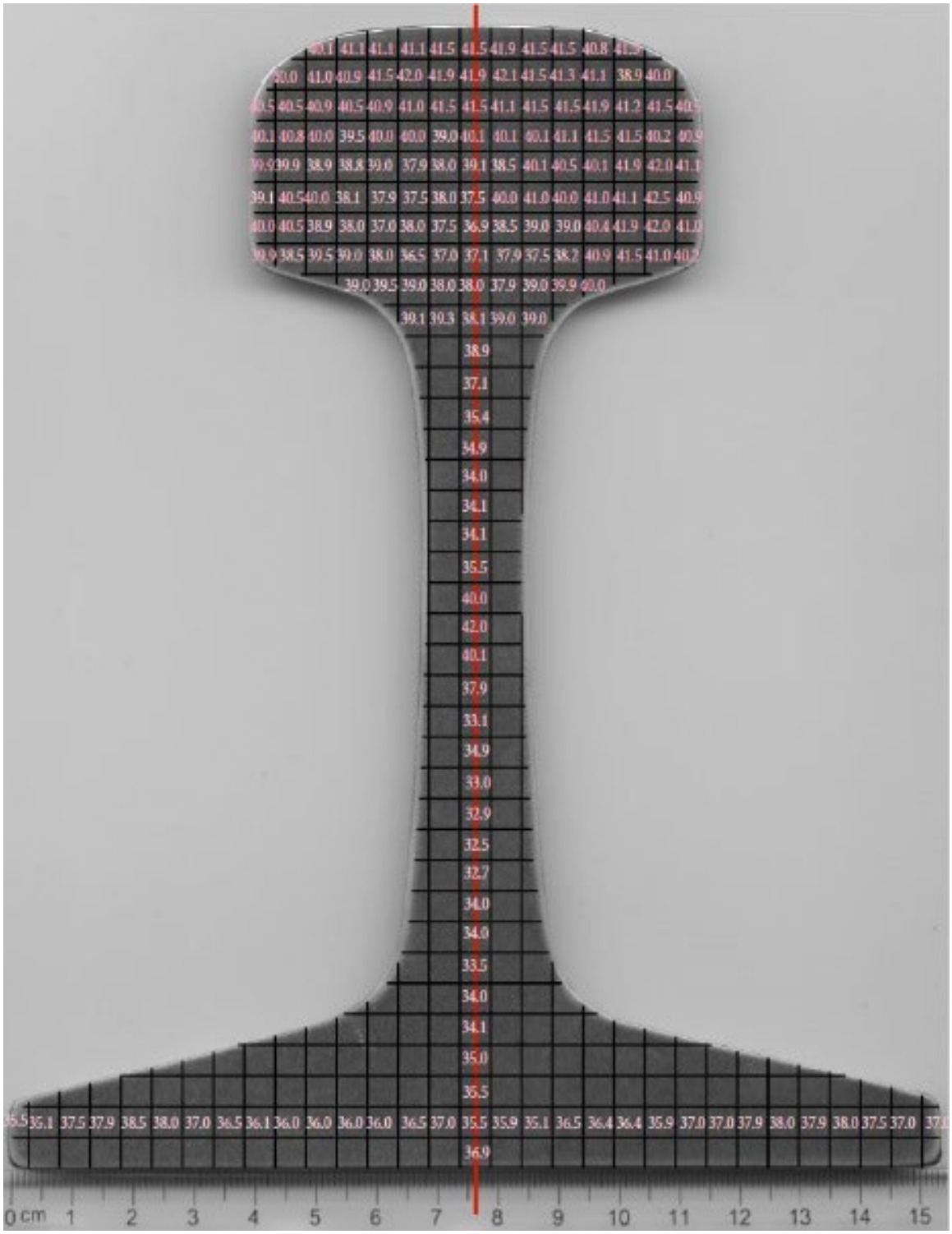

Figure 108. AHH Rail showing measured HRC hardness values

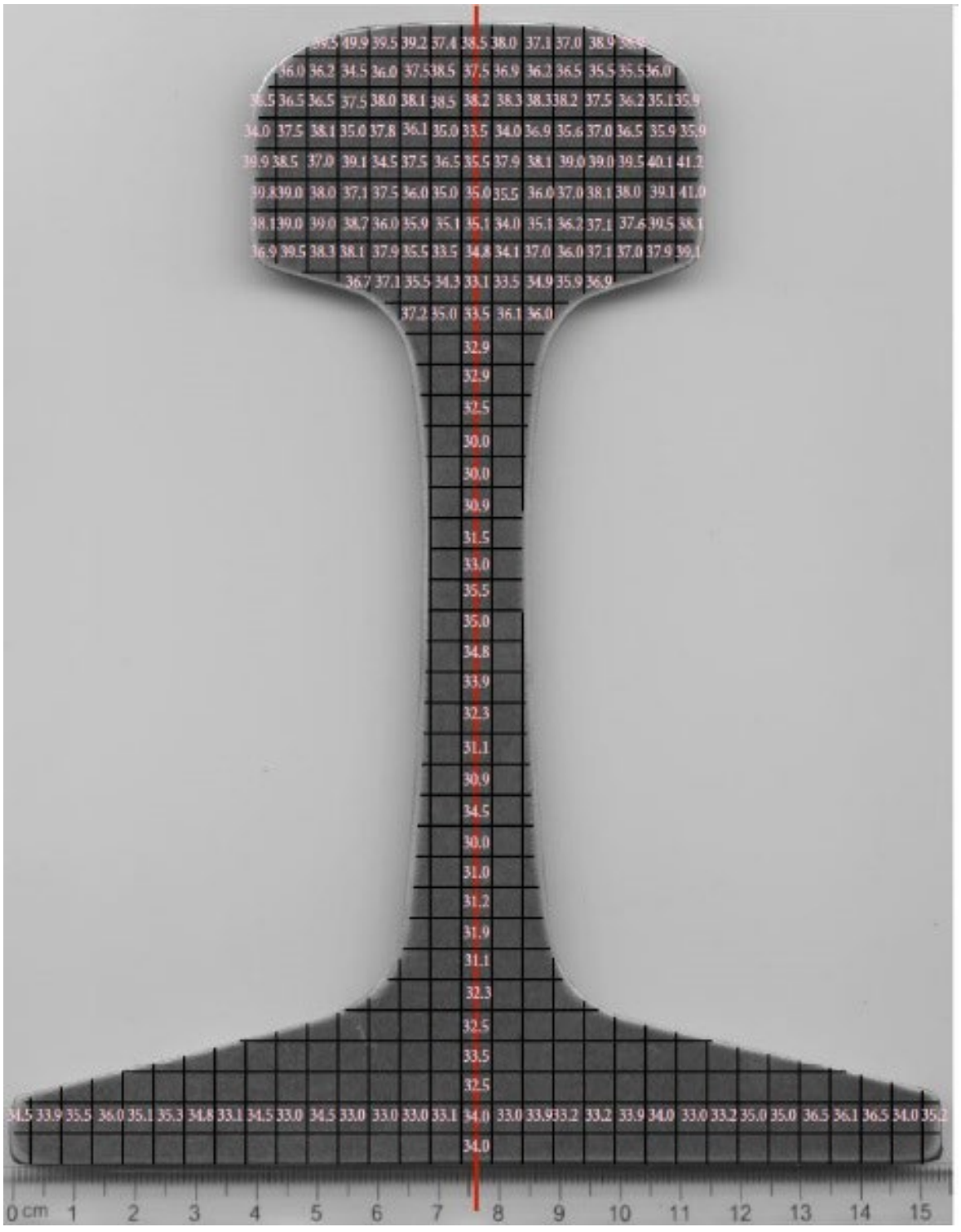

Figure 109. HH Rail showing measured HRC hardness values

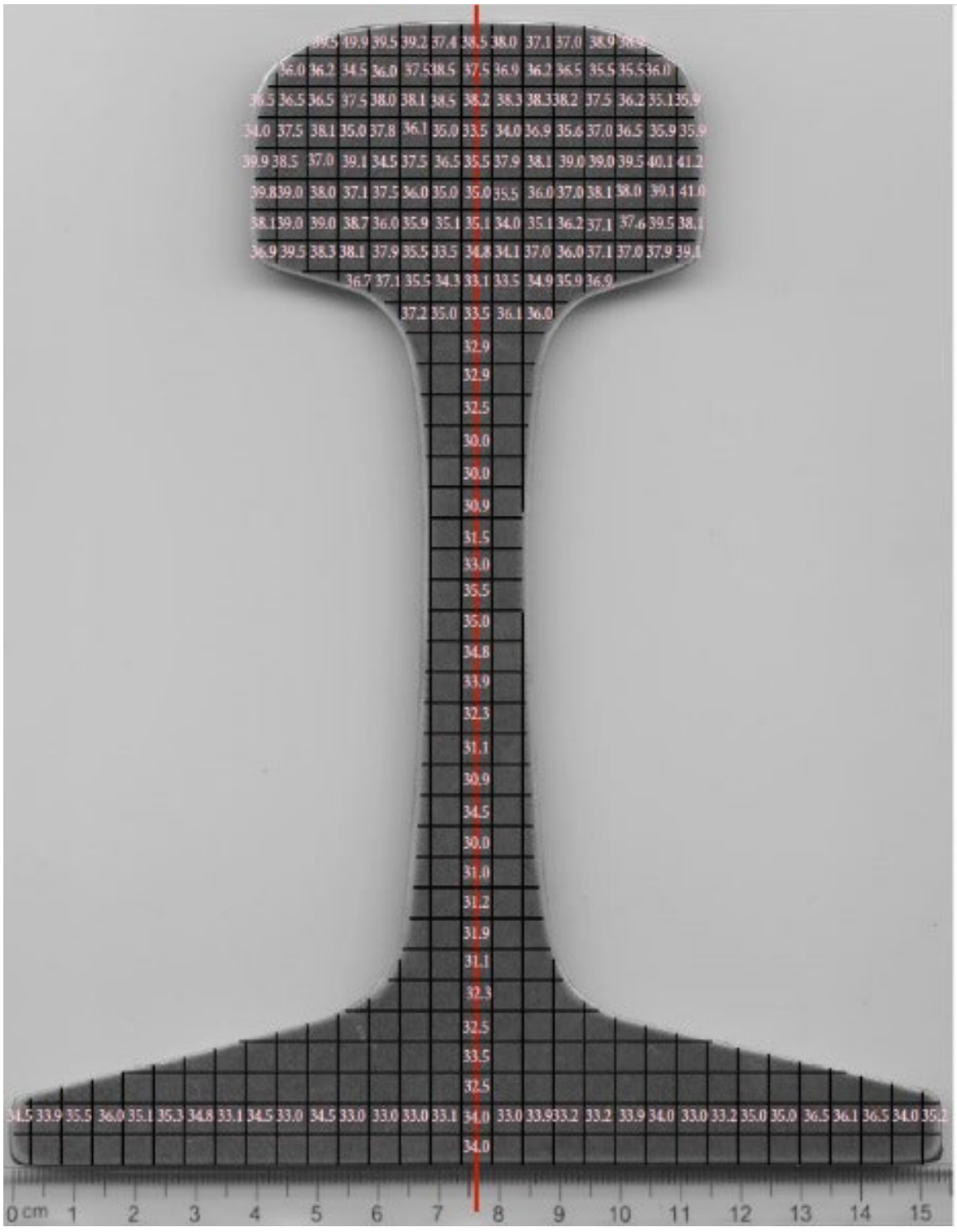

Figure 110. SS Rail showing measured HRC hardness values

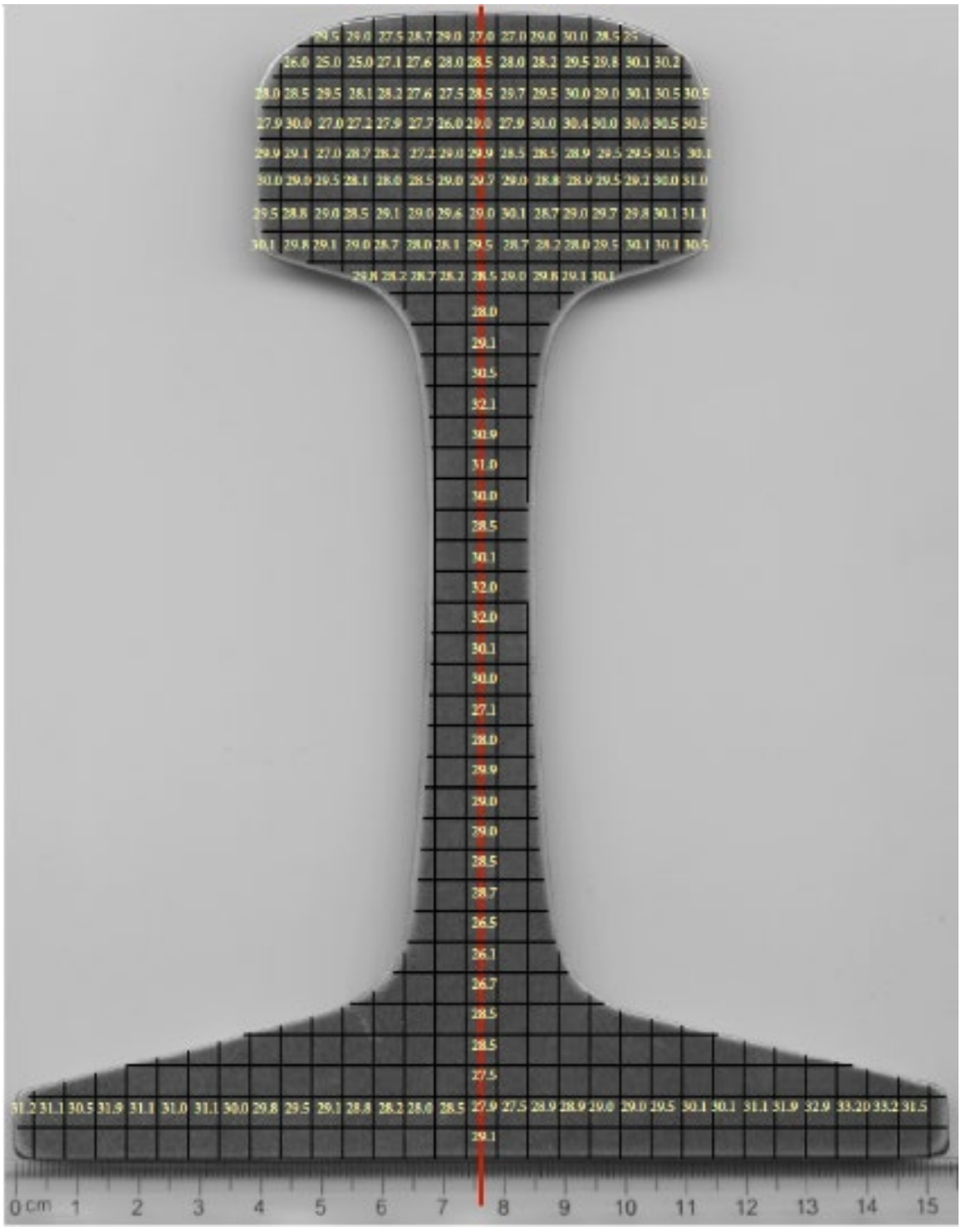

Figure 111. HAY84 Rail showing measured HRC hardness values

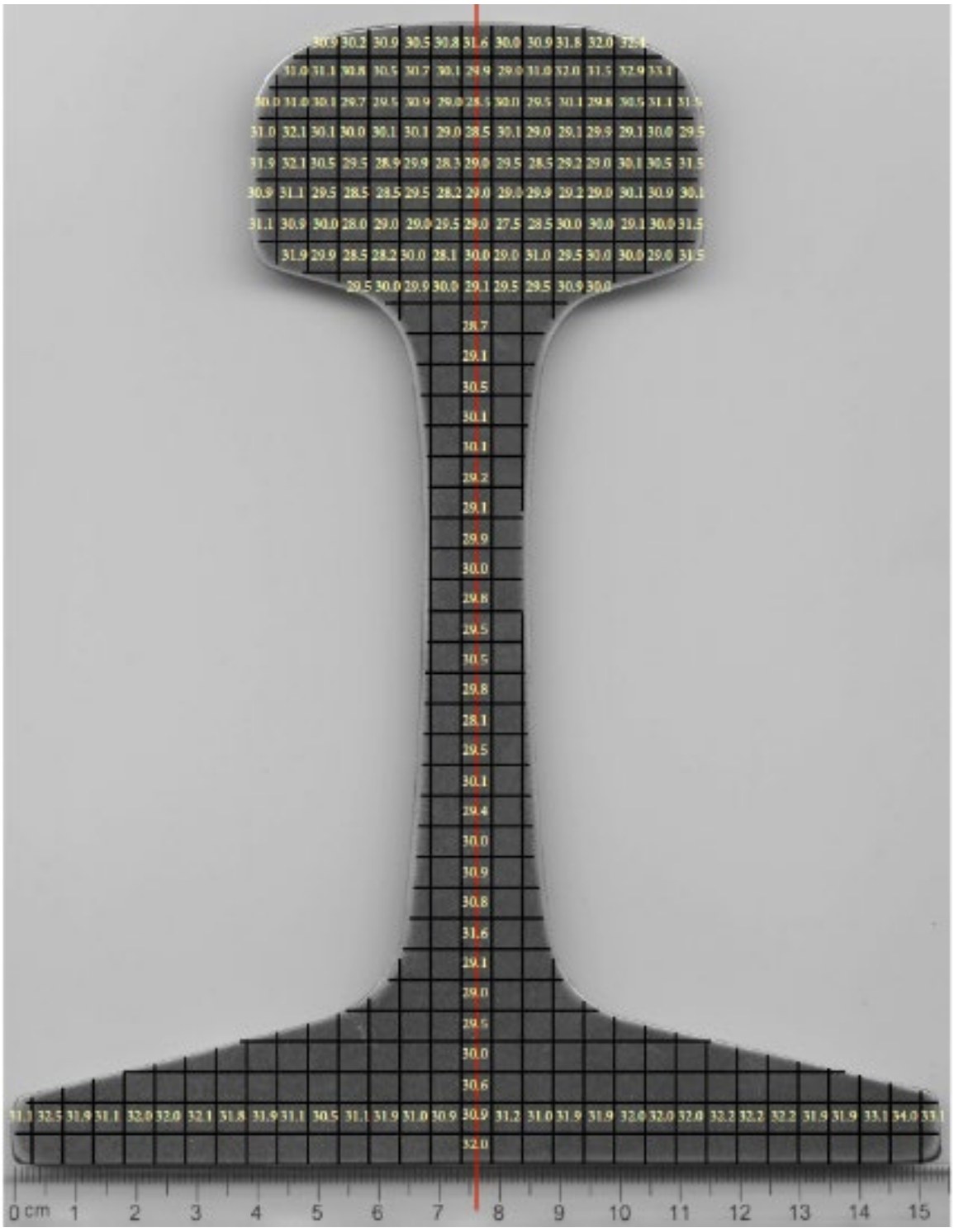

Figure 112. CF&I77 Rail showing measured HRC hardness values

Appendix B. Tensile Stress Strain Curves

As depicted in Figure 113, the standard offset method was used to determine the tensile yield strength in accordance with ASTM E8 standards. Referring to Figure 113, *om* is the specified value of the offset, *mn* is drawn parallel to *OA*, determining *r*, i.e., the intersection of *mn* with the stress-strain curve. In reporting values of yield strength obtained by this method the specified value of the offset was 0.2 percent. Typical stress/strain curves for each of the rails, taken from layer 2 in the railheads (see Figure 38), are given in Figure 114–Figure 118.

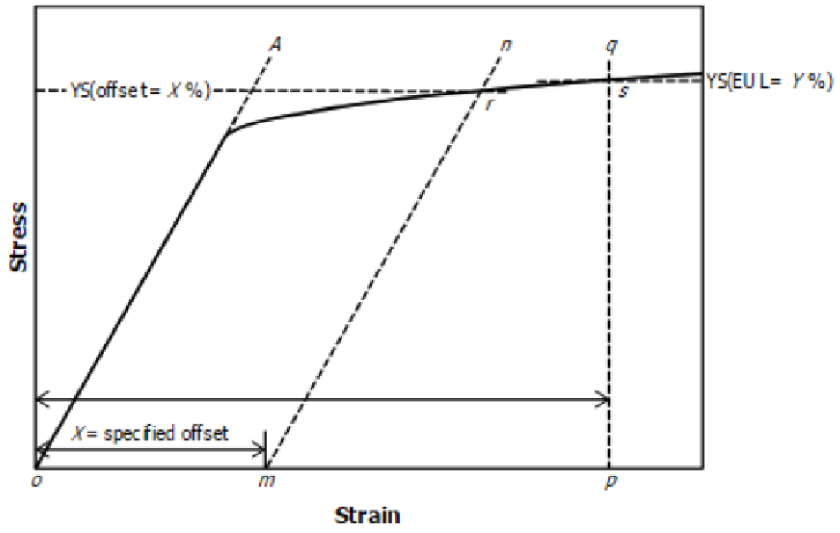

Figure 113. Determination of yield stress based on 0.2 percent offset

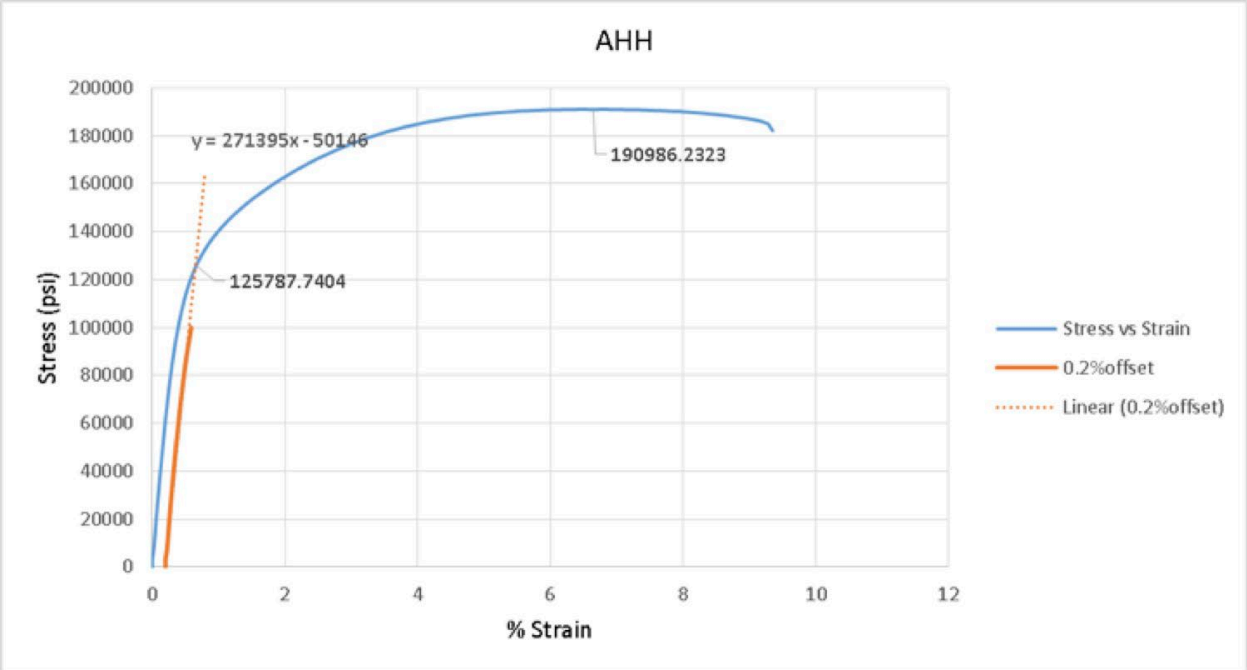

Figure 114. Stress vs Strain for AHH rail, layer 2

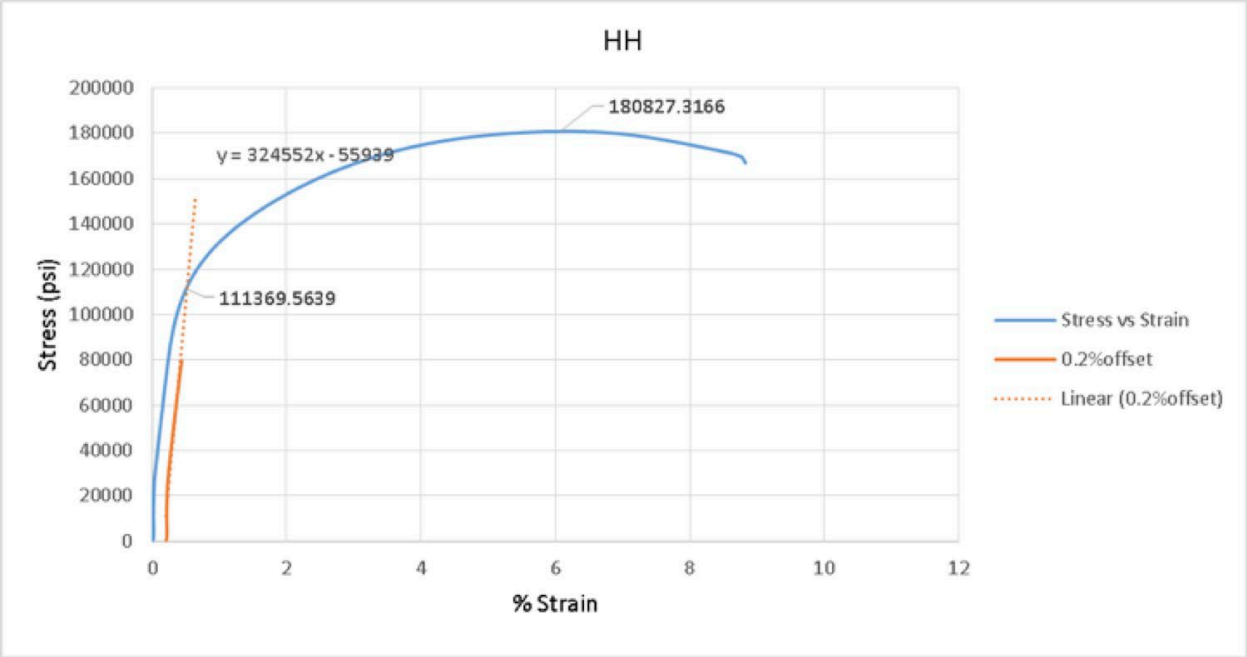

Figure 115. Stress vs Strain for HH rail, layer 2

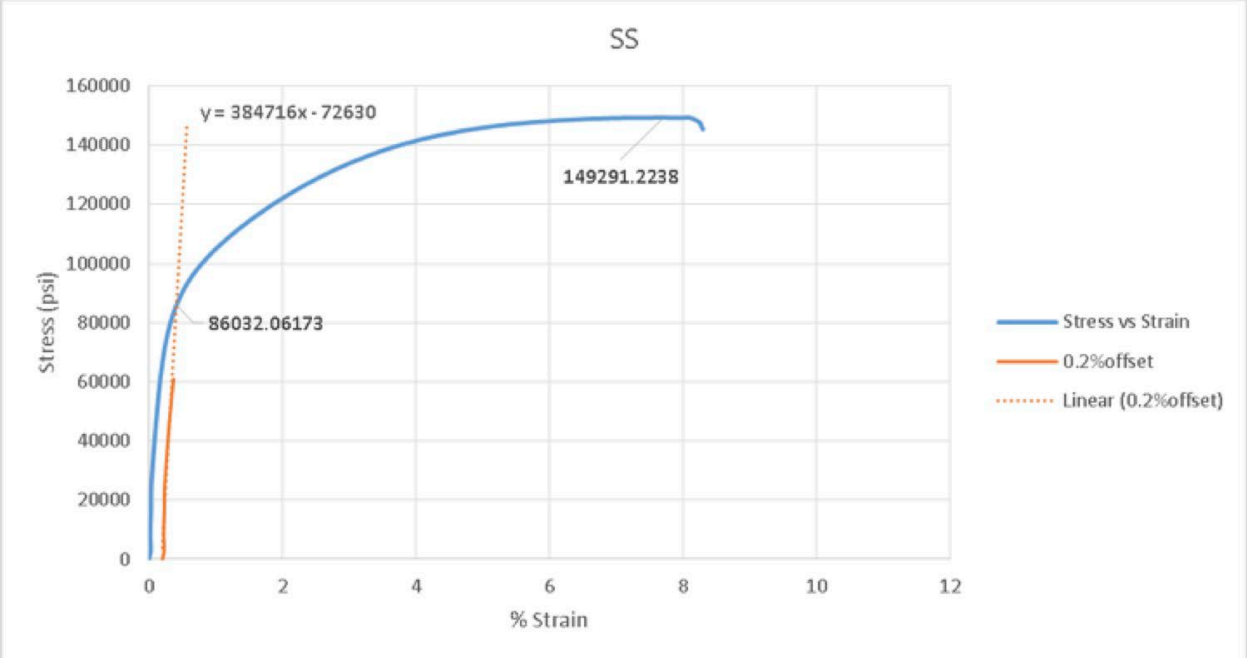

Figure 116. Stress vs Strain for SS rail, layer 2

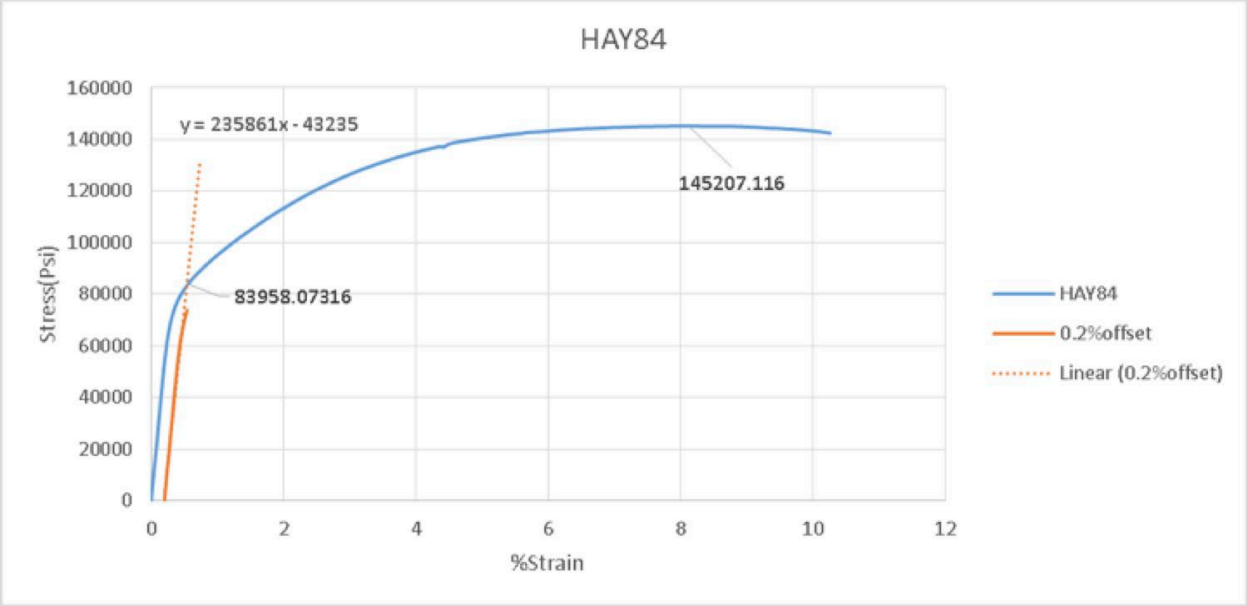

Figure 117. Stress vs Strain for HAY84 rail, layer 2

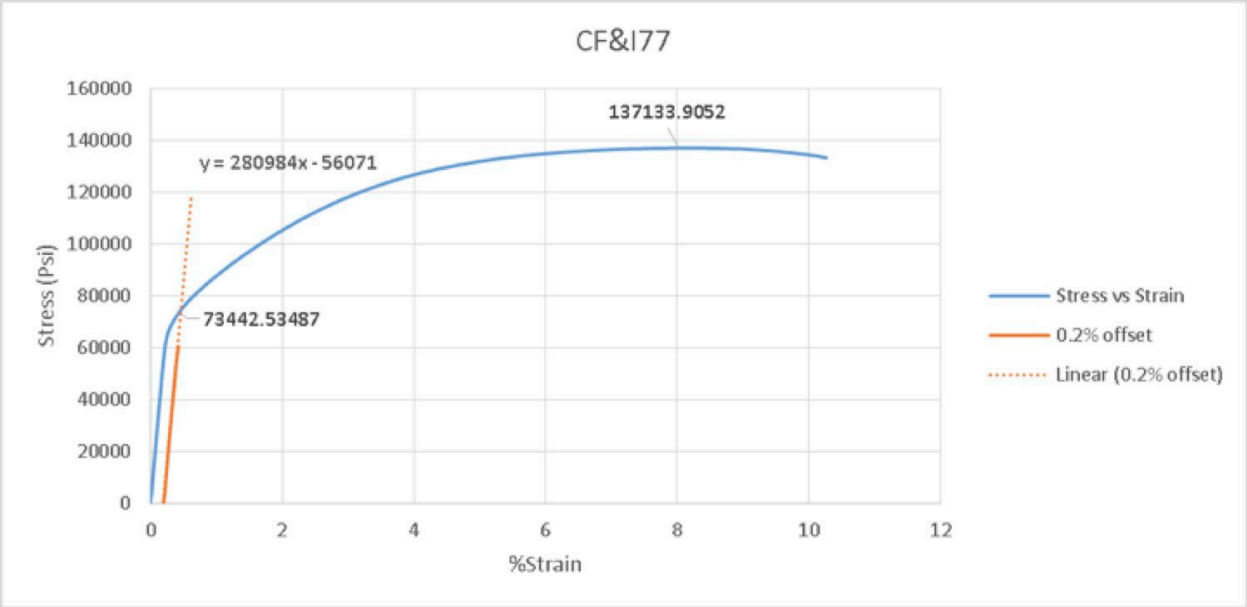

Figure 118. Stress vs Strain for CF&I77 rail, layer 2

Appendix C. Load vs COD Curves for Fracture Toughness

A valid K_{Ic} test requires the determination of a preliminary conditional result, K_Q, which is determined from a graphical construction based on the load-displacement test record, where the displacement is the crack opening displacement (COD) measured at the mouth of the crack. The crack opening displacement in the fracture testing is measured using a clip gauge extensometer (Figure 49). The clip gauge is attached to the CT specimen using machined knife-edges at the mouth of the crack (Figure 47). If, after testing, the calculated value of K_Q satisfies the necessary small scale yielding requirements specified in the ASTM E399 Standards, K_Q can be reported as a valid K_{Ic} value.

When a pre-cracked CT test specimen is loaded to failure, one of three types of valid load versus displacement (COD) curves are possible (see Figure 119). Depending on the actual load-displacement curve that occurs during a test, a value for the critical load, P_Q, is selected, which is then used to calculate K_Q based on the tabulated stress intensity factor solution.

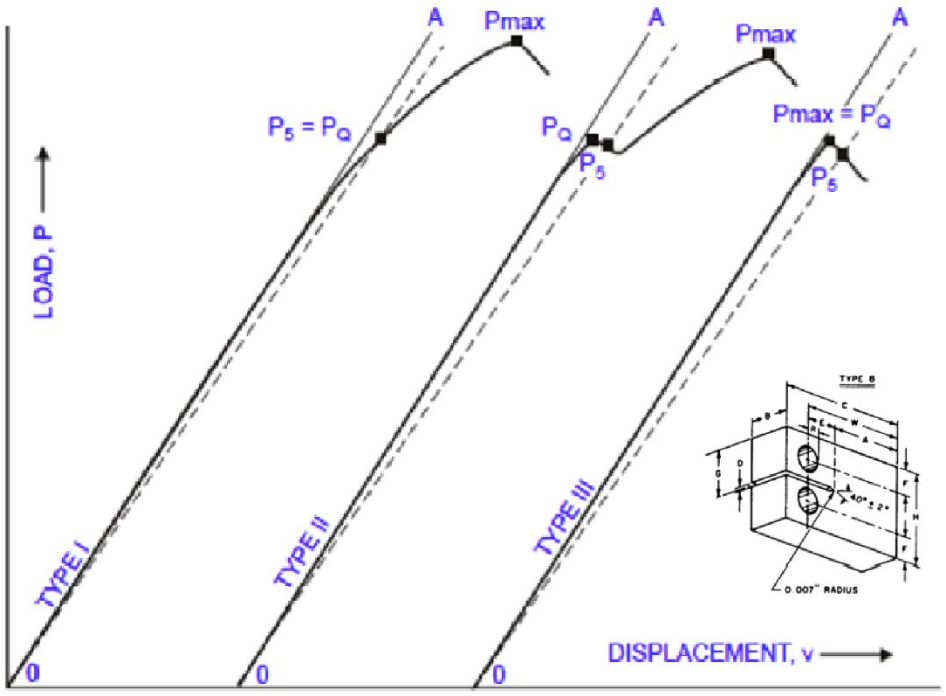

Figure 119. Typical load displacement curves encountered during fracture toughness testing

To obtain P_Q, a line OA is drawn tangent to the initial linear portion of the load-displacement curve. A second line, designated as O_{P5}, and called the 5 percent Secant line, is constructed with a slope equal to 95 percent of the initial load line. The point at which the load-displacement curve and the 5 percent Secant line intersect, determines the point P_5 as shown in Figure 119.

P_Q is determined by the specific load-displacement behavior for a particular test specimen. If the curve is smooth and deviates only slightly from linearity before reaching the ultimate failure load at P_{max}, then it is referred to as a Type I curve as shown in Figure 119 and $P_Q = P_5$. Alternatively, a Type II curve will exhibit a small amount of unstable crack growth, often referred to as pop-in, which occurs before the curve deviates from linearity by five percent. For a Type II curve, P_Q is defined at the pop-in load (Figure 119). A specimen that fails before achieving five percent nonlinearity, is described as a Type III curve. In this case, $P_Q = P_{max}$, as shown in Figure 119. With P_Q determined from the load-displacement curve, K_Q is calculated using the following formula valid for CT specimens:

$$K_Q = f\left(\frac{a}{W}\right)\sigma_Q\sqrt{\pi a}\,, \tag{8}$$

where

$$f(a/W) = 16.7 - 104.7(a/W) + 369.9(a/W)^2 - 573.80(a/W)^3 + 360.5(a/W)^4 \tag{9}$$

and

$$\sigma_Q = \frac{P_Q}{BW}\,. \tag{10}$$

The average crack length a at fracture is determined by directly measuring the crack length on the fractured crack surface at five equally spaced points (0, 0.25, 0.5, 0.75, 1) along the crack front (see Figure 50). The calculations for determining K_{Ic} for an AHH rail CT specimen, based on the load-displacement measurements depicted in Figure 120, will be given as an example. In this particular case the relevant geometric parameters are: 1) crack length $a = 0.0125\ \mathrm{m}$, 2) width $W = 26\ \mathrm{mm}$, and 3) thickness $B = 12.5\ \mathrm{mm}$. Thus, $a/W = 0.48$ and from (9) $f(a/W) = 7.34$. From the load-displacement curve (Figure 120), the value of $P_Q = 7684\ \mathrm{N}$, and from (10), $\sigma_Q = 7684/(26 \times 12.5) = 23.64\ \mathrm{MPa}$. Using equations (8) and (9) K_Q is determined to be: $K_Q = 34.4\ \mathrm{MPa}\sqrt{\mathrm{m}}$. The value of σ_Y was measured as $\sigma_Y = 792\ \mathrm{MPa}$. Thus, it can quickly be established that the value of K_Q satisfies the plane strain requirements (0.0.1)–(0.0.3) for reporting a valid plane strain fracture toughness (K_{Ic}) value. The additional ASTM requirements that 0.45<(a/W)<0.55 and $P_{max} \le 1.1P_Q$ are also satisfied in this test, thus for this specific test, $K_{Ic} = 34.4\ \mathrm{MPa}\sqrt{\mathrm{m}}$. Not all fracture toughness tests conducted in this study resulted in valid K_{Ic} values. In most of the invalid cases, there were minor deviations from the strict ASTM specifications, e.g., the initial fatigue crack front was insufficiently straight, or P_{max} was slightly greater than P_Q, etc. Though the values of K_Q from these tests were still within the range of valid K_{Ic} values, they are not reported as K_{Ic} values. Representative load-

displacement plots that were used for determining K_{Ic} values for all five rails used in this study are shown in Figure 120–124. In each of these figures the P_Q, P_{max}, and K_Q values are given on the plots.

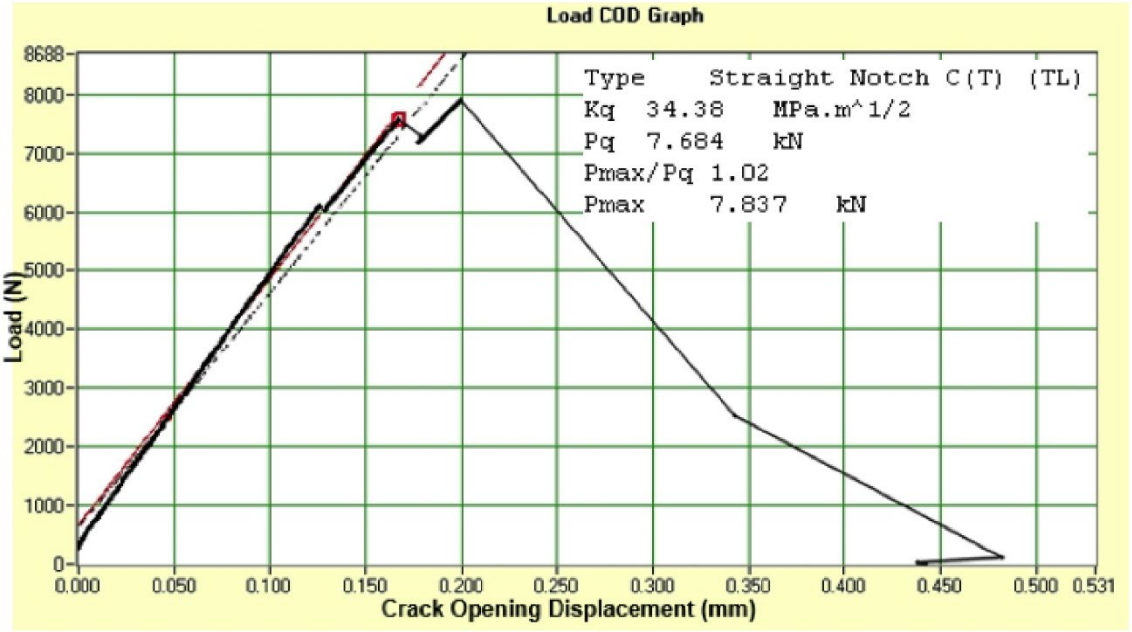

Figure 120. Load vs COD for AHH Rail Fracture Toughness Test

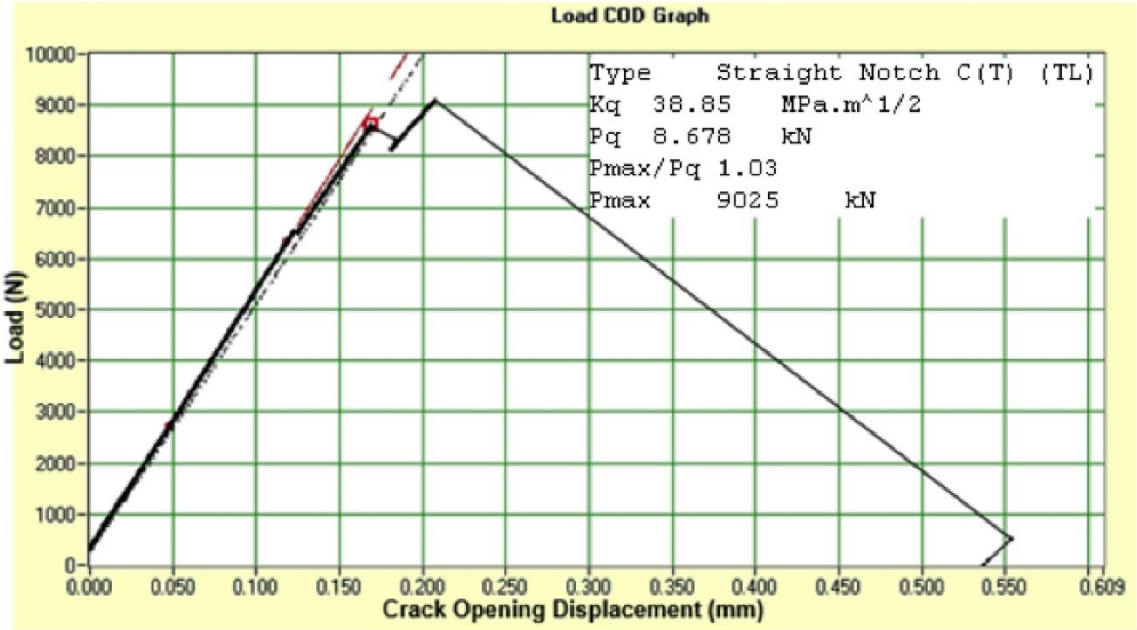

Figure 121. Load vs COD for HH Rail Fracture Toughness Test

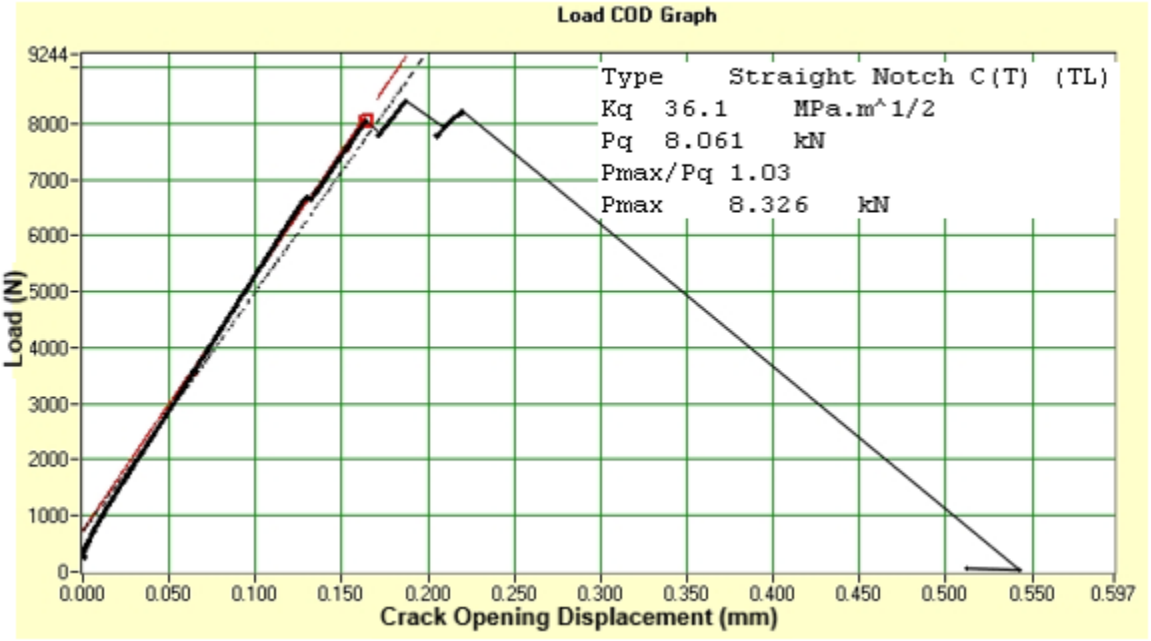

Figure 122. Load vs COD for SS Rail Fracture Toughness Test

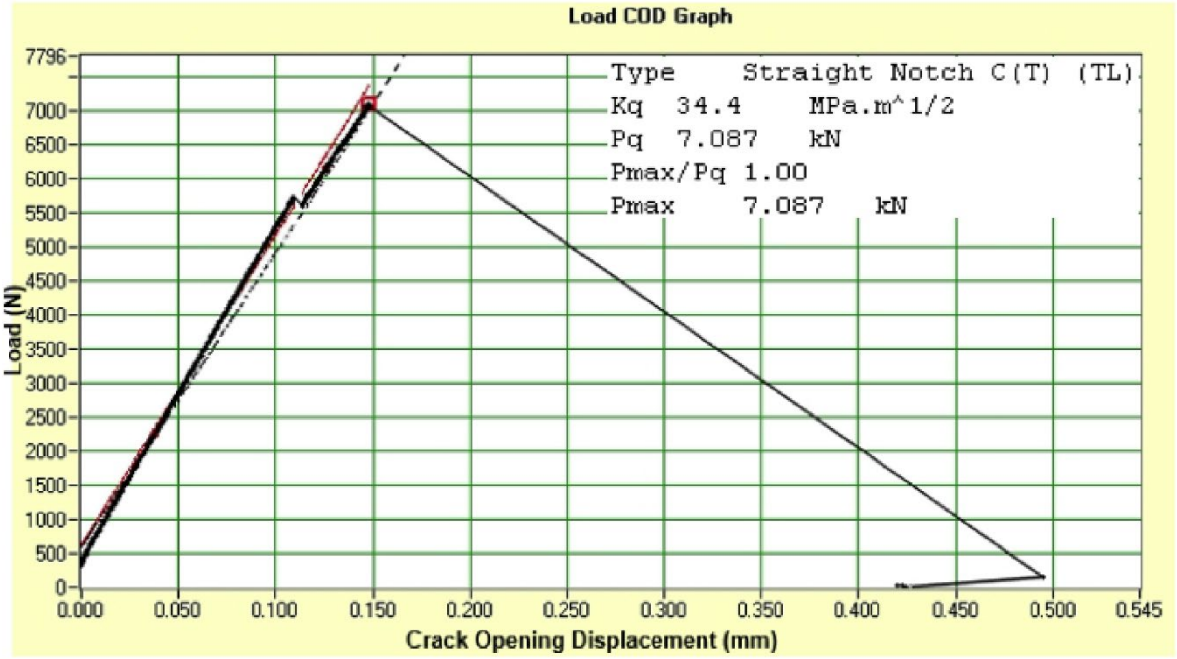

Figure 123. Load vs COD for HAY84 Rail Fracture Toughness Test

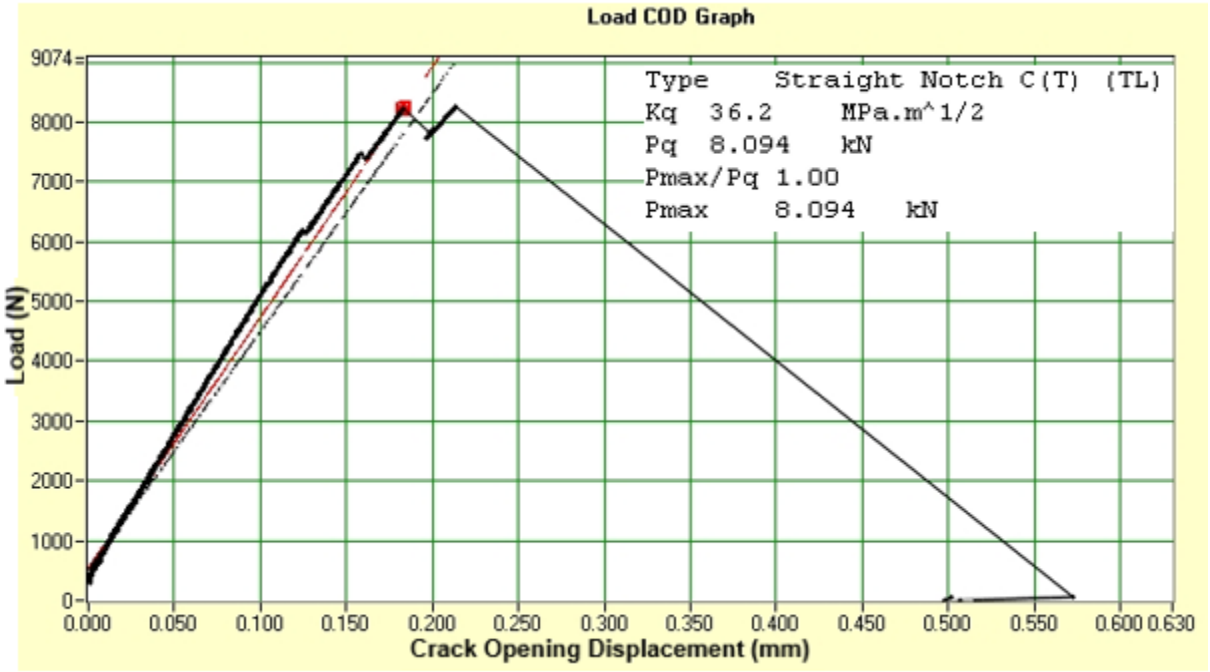

Figure 124. Load vs COD for CF&I77 Rail Fracture Toughness Test

Compliance Crack Length Calculation

During fatigue crack growth rate testing, the crack length a is inferred from changes in the measured compliance. The relationship between compliance and crack length has been analytically derived for the CT specimen. The normalized crack length, a/W, is given by the following polynomial expression:

$$\frac{a}{W} = 1.0010 - 4.6695(U) + 18.460(U)^2 - 236.82(U)^3 + 1214.9(U)^4 - 2143.6(U)^5 , \qquad (11)$$

where

$$U = \frac{1}{1 + \sqrt{\frac{E\delta_1 B}{P}}} . \qquad (12)$$

In (12) E is the elastic modulus, δ_1 is the measured crack opening displacement (COD), P the measured load, and B the specimen thickness. Figure 125 shows a screen capture from the software used to compute the CT crack length, a, during fatigue testing on the Instron mechanical test machine shown in Figure 49.

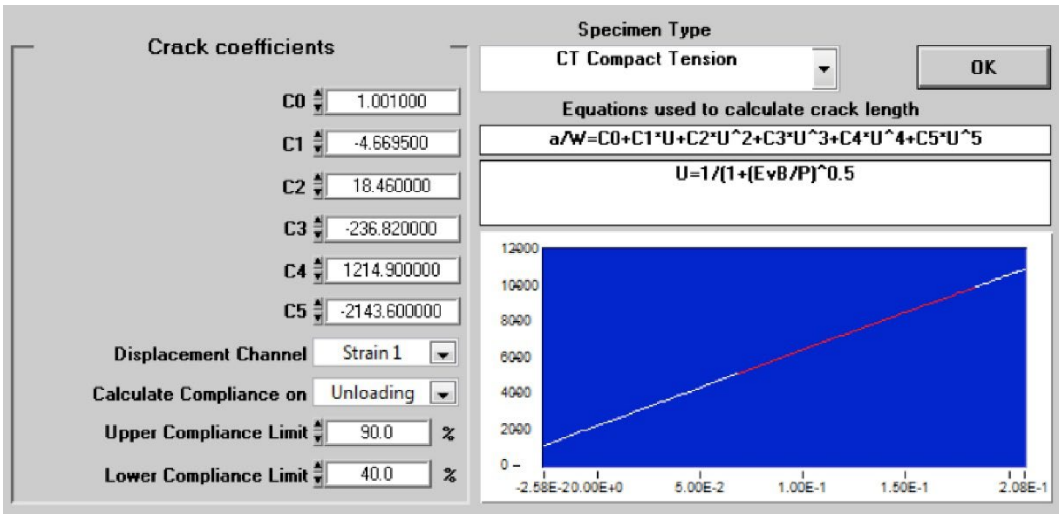

Figure 125. Crack length calculations based on compliance measurements during testing

Abbreviations and Acronyms

ACRONYM	DEFINITION
AHH	Advanced head hardened
CCT	Center cracked tension
CF&I	Colorado Fuel & Iron
COD	Crack opening displacement
CT	Compact tension
EDM	Electrical discharge machining
EDS	Energy dispersive spectrometry
FAST	Facility for Accelerated Service Testing
HH	Head hardened
HZB	Helmholz-Zentrum Berlin
IWM	Institut für Werkstoffmechanik
LOM	Light optical microscopy
LTI	Laboratory Testing, Inc.
NIST	National Institute of Standards and Technology
SEM	Scanning electron microscopy
SS	Standard, control-cooled